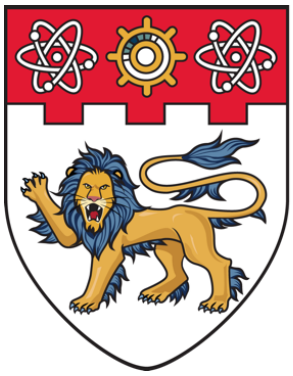

NANYANG TECHNOLOGICAL UNIVERSITY
SINGAPORE

SPIN-PHOTON INTERFACES IN DIAMOND AND SIC SYSTEMS

MU ZHAO

SCHOOL OF PHYSICAL AND MATHEMATICAL SCIENCES

2022

SPIN-PHOTON INTERFACES IN DIAMOND AND SIC SYSTEMS

MU ZHAO

SCHOOL OF PHYSICAL AND MATHEMATICAL SCIENCES

A thesis submitted to the Nanyang Technological University in partial fulfilment of the requirement for the degree of Doctor of Philosophy

2022

Statement of Originality

I hereby certify that the work embodied in this thesis is the result of original research done by me except where otherwise stated in this thesis. The thesis work has not been submitted for a degree or professional qualification to any other university or institution. I declare that this thesis is written by myself and is free of plagiarism and of sufficient grammatical clarity to be examined. I confirm that the investigations were conducted in accord with the ethics policies and integrity standards of Nanyang Technological University and that the research data are presented honestly and without prejudice.

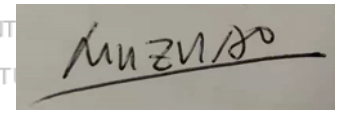

[Input Date Here] [Input Signature Here]

. 2021/08/02. . . . . .Mu Zhao . . . . . .

Date [Input Name Here]

Supervisor Declaration Statement

I have reviewed the content and presentation style of this thesis and declare it of sufficient grammatical clarity to be examined. To the best of my knowledge, the thesis is free of plagiarism and the research and writing are those of the candidate's except as acknowledged in the Author Attribution Statement. I confirm that the investigations were conducted in accord with the ethics policies and integrity standards of Nanyang Technological University and that the research data are presented honestly and without prejudice.

[Input Date Here]	[Input Supervisor Signature Here]
2021/08/02.	. . . . . Weibo Gao. . . . .
Date	[Input Supervisor Name Here]

Authorship Attribution Statement

This thesis contains material from 3 papers published in the following peer-reviewed journals in which I am listed as an author.

Chapter 3 is published as **Disheng Chen[+], Zhao Mu[+],** Yu Zhou, Johannes E. Fröch, Abdullah Rasmit, Carole Diederichs, Nikolay Zheludev, Igor Aharonovich, and Wei-bo Gao. "Optical Gating of Resonance Fluorescence from a Single Germanium Vacancy Color Center in Diamond." Phys Rev Lett 123(3): 033602 (2019).

The contributions of the co-authors are as follows:

- Prof Wei-bo Gao and Prof. Igor Aharonovich supervised the project.
- Dr. Johannes E. Fröch prepared the sample.
- Zhao Mu and Dr. Disheng Chen did the experiments.
- All authors discussed and analyzed the data.
- Dr. Disheng Chen performed the simulation.
- Dr. Disheng Chen and Prof. Weibo Gao wrote the manuscript and it is revised by all the authors.

Chapter 4 is published as **Zhao Mu[+], Yu Zhou[+], Disheng Chen[+],** Johannes E. Fröch, Jianqun Yang, Xingji Li, Igor Aharonovich, Wei-bo Gao. “Observation of Binary Spectral Jumps in Color Centers in Diamond.” Advanced Optical Materials 8, 2000495 (2020).

The contributions of the co-authors are as follows:

- Prof. Xingji Li, Prof. Igor Aharonovich, and Prof. Weibo Gao supervised the research.
- Dr. Johannes E. Fröch, Prof. Jianqun Yang helped with the sample fabrication.
- Zhao Mu and Dr. Yu Zhou performed the experiments.
- Zhao Mu and Dr. Yu Zhou and Dr. Disehng Chen analyzed the data.
- Zhao Mu and Dr. Yu Zhou prepared the manuscript drafts. The manuscript was revised by Dr. Disheng Chen, Prof. Igor Aharonovich, and Prof. Weibo Gao.

Chapter 5 is published as **Zhao Mu,** Soroush Abbasi Zargaleh, Hans Jürgen von Bardeleben, Johannes E. Fröch, Milad Nonahal, Hongbing Cai, Xinge Yang, Jianqun Yang, Xingji Li, Igor Aharonovich*, and Weibo Gao*. "Coherent Manipulation with Resonant Excitation and Single Emitter Creation of Nitrogen Vacancy Centers in 4H Silicon Carbide." Nano Lett. 20, 8, 6142–6147. (2020)

The contributions of the co-authors are as follows:

- Prof. Xingji Li, Prof Wei-bo Gao, and Prof. Igor Aharonovich supervised the project.
- Dr. Abbasi Zargaleh, Dr. Johannes E. Fröch, Milad Nonahal, Dr Hongbing Cai, and Prof. Jianqun Yang helped the sample preparation.
- Zhao Mu performed the experiments with Xinge Yang.
- Zhao Mu analyzed the data.
- Prof. Hans Jürgen von Bardeleben did the electron paramagnetic resonance experiment.
- Zhao Mu and Prof. Wei-bo Gao prepared the manuscript and it is revised by all the authors.

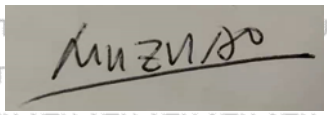

[Input Date Here]	[Input Signature Here]
. 2021/08/02.	. Mu Zhao. . . . .
Date	[Input Name Here]

Abstract

Color centers in wide bandgap materials that behave as 'artificial atoms' are promising candidates for quantum applications. The negatively charged nitrogen-vacancy (NV^-) center in diamond is a benchmark platform for testing the quantum sensing, the quantum communication, and the quantum computation. However, the optical properties of the NV^- center system are not yet perfect for the realization of the quantum network. Compared to the NV^- center, there are many types of defects in diamond or hosts like silicon and silicon carbide (SiC) which exhibit superior optical properties. This thesis is devoted to studying two spin-photon interfaces including group IV defects in diamond and $N_CV_{Si}^-$ centers in SiC.

Chapter 1 presents basic elements of the quantum network employing the quantum resources in the solid-state color centers systems. The latest progress in the quantum computation and the quantum network based on these systems are then presented. After that, the motivation of this study is introduced regarding the emerging challenges.

Chapter 2 starts with introducing several experimental methodologies utilized for the optical and spin study of color centers. Then it describes the physical properties of diamond and SiC hosts along with molecular configurations of two kinds of defects. The recent progress on the optical and microwave manipulation of the group IV defects in diamond and defects (silicon-vacancy (V_{Si}^-), divacancy (VV^0), and $N_CV_{Si}^-$ centers) in SiC are reviewed.

Chapter 3 presents our study of the negatively charged germanium vacancy (GeV^-) center in diamond. The GeV^- centers in the diamond sample exhibit quenched emission upon resonant excitation but could be lightened up with an additional off-resonant excitation. We attribute this abnormal behavior to the presence of an extra dark. The competing dynamical process between a 'dark' state and a 'bright' state is further investigated and simulated with a three-level system.

Chapter 4 presents our observation of the binary spectral jump behavior of Ge-related single-photon emitters in diamond. The optical properties of these emitters are investigated.

Chapter 5 presents the study of $N_CV_{Si}^-$ centers in 4H-SiC. The fine orbital structure of the excited states and the zero-field splitting in the spin ground states are characterized by resonant laser excitation and microwave-assisted spin manipulation. The coherent manipulation of

$N_CV_{Si}^-$ centers ensembles is realized upon resonant excitation. Meanwhile, single $N_CV_{Si}^-$ centers generations and their optical properties are reported.

Chapter 6 begins by drawing conclusions on this thesis. After that, outlooks on several possible directions toward better spin-photon interfaces are presented.

Acknowledgments

Time flies! My 4-year Ph.D. study would not proceed so smoothly without help from many people. This journey will benefit my whole life. I would like to take this opportunity to thank all the following people.

First, I would like to thank Prof. Gao Weibo. Prof. Gao gave me the chance to join his excellent group where I can get access to state-of-the-art instruments. When I was a beginner, he spent lots of time discussing and designing my project. With his help, I could manage to do experiments individually in a short time. In the third and fourth years, Prof. Gao allowed me to explore various topics, which broadened my horizon and would benefit my future research. It is no doubt worthwhile to mention his passion for science. Whenever I came up with difficulties, I could always get valuable advice from him.

During my study, I received valuable advice from my Thesis Advisory Committee members, Prof. CHEW Lock Yue and Prof. WILKOWSKI David. Thank you all for the feedbacks and discussions.

As an experimentalist, I have the fortune to get sample support from various collaborators. Prof. Igor Aharonovich leads a great group with rich experience in sample preparation and nanostructures fabrications. I want to thank Igor and his group members: Dr. Johannes, Forech, Dr. Amanuel Berhane, Milad Nonahal from the University of Technology Sydney. Prof. Li xingji and Prof. Yang jianqun, their members Dong lei, and Wan Pengfei from Harbin Institute of Technology, thank you all for your efforts on sample preparation and theoretical support. Thanks to Prof. Hans Jurgen Von Bardeleden and Dr. Soroush Abbasi Zargaleh for your efforts on the NV project. I also appreciate the support from our collaborators from NTU, Dr. Giorgio Adamo for his nanofabrication.

It is a great pleasure to join the Quantum Photonics Group where I met so many great teammates. I would first thank our earlier group members whose contributions benefit me a lot. I learned a lot from Dr. Zhou Yu, experimentally and personally. He trained me in both the optics and microwave experiments and set me an example on how to be a good Ph.D. student. Thank you, Dr. Zhou. With Dr. Chen Disheng, we worked on the GeV project. Dr. Chen impressed me with his deep understanding of physics, from whom I learned to think the mechanism. Dr. Rasmit Abudullah, whom I discussed a lot on the nanostructure simulation and my project, always shows me that I know nothing. I appreciate the help given by Dr. Cai Hongbing, Dr. Tang Chaolong, Dr. Laishen, Dr. Wang Naizhou, for the sample fabrication. Thanks to Dr. Tan Qinhai, Dr. Tian Yao, Dr. Liu Yuanda. During the past years, I shared a lot

of happiness with Huang Zumeng, Wang Ziyu, Zhang Zhaowei, Lv Xiaodan, Yang Zhenning, Zhang Chusheng. Thank you all for your support and company.

And in the end, my thanks to my family who supports me in my tough times. This Ph.D. study would not be possible without your support and patience.

Table of Contents

List of publications

First and co-first authored papers:

1. **Disheng Chen[+], Zhao Mu[+],** Yu Zhou, Johannes E. Fröch, Abdullah Rasmit, Carole Diederichs, Nikolay Zheludev, Igor Aharonovich*, and Wei-bo Gao*. "Optical Gating of Resonance Fluorescence from a Single Germanium Vacancy Color Center in Diamond." Phys Rev Lett 123(3): 033602. (2019) *(Equal contribution)*
2. **Zhao Mu,** Soroush Abbasi Zargaleh, Hans Jürgen von Bardeleben, Johannes E. Fröch, Milad Nonahal, Hongbing Cai, Xinge Yang, Jianqun Yang, Xingji Li, Igor Aharonovich*, and Weibo Gao*. "Coherent Manipulation with Resonant Excitation and Single Emitter Creation of Nitrogen Vacancy Centers in 4H Silicon Carbide." Nano Lett. 20, 8, 6142–6147. (2020)
3. **Zhao Mu[+], Yu Zhou[+], Disheng Chen[+],** Johannes E. Fröch, Jianqun Yang, Xingji Li, Igor Aharonovich*, Wei-Bo Gao*. "Observation of Binary Spectral Jumps in Color Centers in Diamond." Advanced Optical Materials 8, 2000495. (2020) *(Equal contribution)*
4. **Zhao Mu,** Abdullah Rasmita, Jianqun Yang, Xingji Li*, Weibo Gao*. "Room-Temperature Solid-State Quantum Emitters in the Telecom Range." Adv. Quantum Technol. 4: 2100076. (2021)

Co-authored papers:

5. Yu Zhou, **Zhao Mu**, Giorgio Adamo, Sven Bauerdick, Axel Rudzinski, Igor Aharonovich, Wei-bo Gao. "Direct writing of single germanium vacancy center arrays in diamond." New Journal of Physics, 20(12), (2018)
6. Toan Trong Tran, Blake Regan, Evgeny A. Ekimov, **Zhao Mu**, Zhou Yu, Weibo Gao, Prineha Narang, Alexander S. Solntsev, Milos Toth, Igor Aharonovich, Carlo Bradac. "Anti-Stokes excitation of solid-state quantum emitters for nanoscale thermometry." Science Advances Vol. 5, no. 5, eaav9180 (2019)
7. Kh. Khazen, H. J. von Bardeleben, S. A. Zargaleh, J. L. Cantin, **Zhao Mu**, Weibo Gao, T. Biktagirov, and U. Gerstmann. "High-resolution resonant excitation of NV centers in 6H − SiC: A matrix for quantum technology applications." Phys. Rev. B 100, 205202 (2019)
8. Jian Zhou, Changyu Li, Denghao Li, Xiaofeng Liu, **Zhao Mu**, Weibo Gao, Jianrong Qiu, Renren Deng. "Single-molecule photoreaction quantitation through intraparticle-surface energy transfer (i-SET) spectroscopy." Nature Communications 11, 4297 (2020)
9. Johannes E. Fröch, Mehran Kianinia, **Zhao Mu**, Vijay Bhatia, Sejeong Kim, Julie M. Cairney, Weibo Gao, Carlo Bradac, Igor Aharonovich, Milos Toth. "Versatile direct-writing of dopants in a solid state host through recoil implantation." Nature Communications 11(1): 5039. (2020)

List of abbreviations

AOM: acousto-optical modulator
EOM: electro-optical modulator
EPR: electron paramagnetic resonance
$g^{(2)}(\tau)$: second order correlation
GeV^-: negatively charged germanium vacancy
HBT: Hanbury Brown and Twiss
HOM: Hong–Ou–Mandel
IR: infrared
kcps: kilo counts per second
NV^- (in diamond): negatively charged nitrogen vacancy
$N_CV_{Si}^-$ (in SiC): negatively charged nitrogen vacancy
PbV^-: negatively charged lead vacancy
PL: photoluminescence
PLE: photoluminescence excitation
PSB: phonon side band
ODMR: optically detected magnetic resonance
QDs: quantum dots
QKD: quantum key distribution
QIP: quantum information processing
RF: resonance fluorescenc
SiC: silicon carbide
SiV^- (in diamond): negatively charged silicon vacancy
SPS: single photon source
SPEs: single photon emitters
SnV^-: negatively charged tin vacancy
VV^0: neutral divacancy
V_{Si}^- (in SiC): negatively charged silicon vacancy in SiC
ZPL: zero phonon line

Chapter I Introduction

1.1 Introduction to quantum network

Quantum mechanics is one of the most successful theories in science. It has enabled the invention of transistors and lasers, which are the products of the first quantum revolution[1]. The transistors are the basic elements of today's computers. The size of the transistors determined the performance of the computers. This size is approaching atomic scale, where the source-drain leakage is no longer negligible[2]. Thus, it demands new computing architectures, one of them is quantum computing[3].

On the other hand, these scattered nodes are connected to the Internet so that information can be shared among them. The security of the information is currently guaranteed by end-to-end encryption. This security is based on the limited computing power of modern computers in light of the long length of the encryption keys[4]. However, the quantum computer could decrypt these keys much faster than the current computers[5]. This in turn requires people to develop a new key distribution protocol. One of the potential solutions is the quantum key distribution (QKD)[6].

Some scientists believe that we are experiencing the second quantum revolution[7]. During the second phase of the revolution, the quantum nature of particles (coherence, interference, superposition, and entanglement) is exploited[8]. These particles often have two orthogonal states which are employed to build up the quantum version of the binary bits, named as quantum bits (qubits). People have developed many platforms to construct qubits, including superconducting loops[9], trapped ions[10], neutral atoms[11], dopants in silicon[12], and color centers in wide-bandgap materials[13]. With these systems, people are investigating the realization of quantum applications, including quantum computation, quantum communication, quantum sensing, and ultimately the quantum network.

Figure 1.1(a) shows the quantum network with building blocks, including quantum repeaters, quantum nodes, and quantum channels[14]. This quantum network is based on realizing the quantum applications at local nodes and would benefit qubits being shared by different nodes. **The quantum nodes** involve the realization of quantum computation[8] using qubits (spin, charge, etc.) or quantum sensing[15] of fields (magnetic and electric fields, temperature). **The quantum channels** refer to free space or fiber-based key or entanglement distributions[6]. Photons are widely used as information carriers among quantum nodes. In practice, the spin states at **local nodes** are encoded into photon states via spin-photon

entanglement. Photons can then be sent to other nodes to realize key distribution or identical photons from two nodes could be sent onto a beam splitter to realize the spin-spin entanglement between two nodes[16] (Figure 1.1(b)). If spin-spin entanglement could be realized between any nodes, teleportation of states can be realized[17]. In practice, photon loss in fiber networks would limit the quantum operation rates and the transmission distance. In this regard, the quantum repeater is an indispensable component of the quantum network to realize a long-distance key distribution. **The quantum repeaters** include an efficient electron spin-photon interface along with nuclear spins serving as quantum memories[18]. After establishing two pairs of quantum entanglement (quantum node A and quantum repeater B, quantum repeater B and quantum node C), A's information can then be teleported to C without sacrificing security. The distribution length could be prolonged with the help of quantum repeaters. To realize the quantum network, it demands platforms having an optical interface.

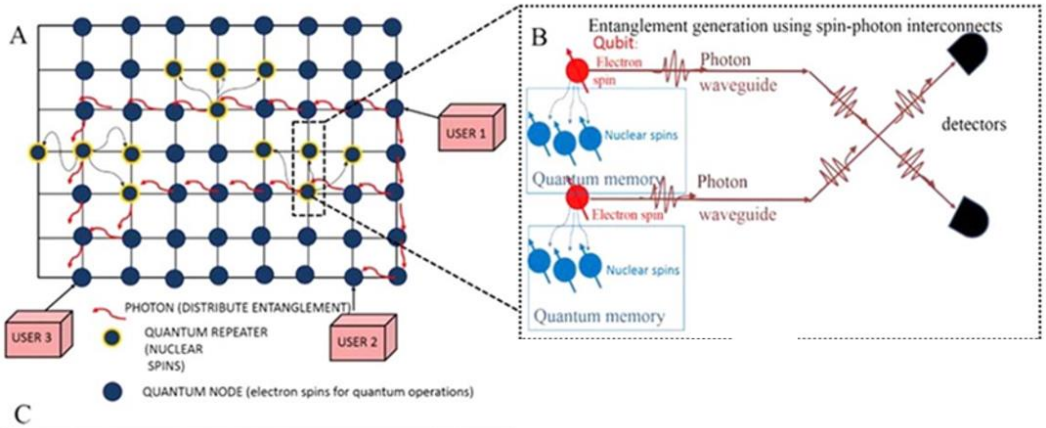

C

Material and color centres	spin coherence time	ancilla qubits	emission wavelength
Diamond Nitrogen Vacancy	>1s	^{13}C and ^{14}N	637nm
SiC double vacancy	1ms	^{13}C and ^{29}Si	1100nm
SiC vacancy silicon	20 ms	^{13}C and ^{29}Si	900nm
QDs in 2D TMC	unknown	unknown	near infrared
InAs/gaAs QDs	3-10 μs	Mn dopants	900-1550nm

Figure 1.1: Quantum network[14]. (a) The quantum network includes three essential components: quantum channels, quantum repeaters, and quantum nodes. (b) A scheme for entanglement distribution between two quantum nodes via photons. Nuclear spins are used to store the information, which could be mapped out to electron spins by generating entanglement between electron spins and nuclear spins. (c) Representative candidates with spin-photon interfaces for the realization of the quantum network. Reproduced under the terms of a creative commons CC-BY international license [14]. Copyright 2020, The Authors, published by IOP Publishing.

1.2 Quantum applications of color centers in wide bandgap materials

Among these systems mentioned above, color centers in wide-bandgap materials have demonstrated themselves as promising candidates fulfilling the requirements of all applications because of the presence of spin-photon interfaces[19-23]; in other words, the electron spin states could be manipulated deterministically with photons (laser, microwave), the spin states could be mapped out deterministically into the photon states (frequency, polarization), and nuclear spins allow for constructing of quantum memories. Figure 1.1(c) lists several spin-photon interfaces including color centers in diamond and SiC, and quantum dots. The NV^- center in diamond is the most studied system among the investigated color centers. It has been employed to demonstrate a quantum network composed of three nodes[24], realize a 10 qubits quantum processor with coherence time up to 1 minute[25], and detect AC and DC magnetic fields with $pT/\sqrt{Hz}$ precision[26]. Besides diamond NV^- centers, the recent progress of SiV^- center in diamond demonstrated itself as a promising platform to realize the quantum repeater. The SiV^- spin exhibits a millisecond coherence time at 100 mK[27]. The Harvard group has reported memory-enhanced quantum communication based on this system[28], a cornerstone of long-distance key distribution.

Despite these significant breakthroughs, these platforms are not yet perfect. Regarding the NV^- center in diamond, there are still two aspects preventing it from going further. The first is its emission wavelength at 637 nm, which is incompatible with the current fiber-based communication channels[29]. The second is the low ZPL ratio around 3%, limiting the spin-photon entanglement rates[30] because the entanglement is realized with ZPL photons. With regard to the SiV^- in diamond, the great challenge is imposed by the critical operating temperature. **While it is essential to scale up the color center qubits and realize high fidelity quantum gates based on these two systems, the study of emerging new color centers platforms that exhibit complementary or better properties than these two systems is equally important.** Years of study on the NV^- centers and SiV^- centers in diamond allow people to give a comprehensive description of an ideal of color centers systems regarding their optical, spin, charge, and host properties[29]. This precious experience not only offers people the toolbox to optimize the properties of the emerging defects, but also it enables people to design defects with desired properties[31]. With two decades of study of color centers systems, it is believed that ideal platforms should satisfy the following aspects[29, 32]:

(1) Optical properties. Ideal color centers should be bright and stable telecom emitters. Their emission should exhibit lifetime limited linewidth at cryogenic temperature. Their lifetime should be within the nanoseconds range.
(2) Charge properties. Charge states of the emitters should be controllable with the Fermi-level engineering or electrical-optical methods.
(3) Spin properties. The ODMR contrast should be high enough. The spin dephasing time and spin coherence time should be long enough to allow quantum gate operation and enable high sensitivity detections.
(4) Host. The host should be nanofabrication friendly and could be purified to provide a clean environment for the residing spin qubits.

This thesis is dedicated to investigating two types of color centers and their associated optical, spin, charge, and host properties. Knowledge of these properties opens the door to their applications into quantum information sciences.

1.3 Motivations and thesis overview

Regarding the low ZPL ratio of NV^- centers in diamond , people have studied group IV split vacancy centers in diamond whose ZPL ratios are greater than 50%[33]. To overcome the critical working temperature of SiV^- centers in diamond, people resorted to other defects including GeV^-, SnV^- and PbV^- centers. The energy differences of the group IV split vacancy centers between the ground orbital doublets get larger when the elements change from Si to Ge. It is thus expected that the GeV^- centers would have a long spin coherence time at a higher working temperature than the SiV^- centers counterpart. During the study of GeV^- centers that were generated via the high energy ion implantation, I observed a dark state besides the typical energy levels of GeV^- centers. I then delved into (1) how it is possible to recover the emission of GeV^- centers upon resonant excitation; (2) how this dark stater would affect the optical properties of GeV^- centers; (3) what the dark state may be.

Regarding the visible emission wavelength of diamond NV^- centers, people have raised a corresponding solution, to convert NV^- centers' emission into the infrared (IR) range[34]. Alternatively, people may utilize color centers whose emission is in the IR range[14]. In this regard, I studied the $N_CV_{Si}^-$ centers in SiC whose ZPLs are near the telecom window. A competitive candidate for quantum applications requires long spin coherence times and bright emission. I then studied (1) how to generate single $N_CV_{Si}^-$ centers in SiC; (2) the optical

properties of single $N_CV_{Si}^-$ centers in SiC; and (3) the spin properties of $N_CV_{Si}^-$ ensembles in SiC.

While these two defects are new entrants in terms of their composing element or host, they could still be categorized into two families. The GeV^- centers in diamonds naturally belong to group IV split vacancies centers; however, the $N_CV_{Si}^-$ centers in SiC share similar energy levels with NV^- centers in diamond or VV^0 centers in SiC. It is thus believed that some works on the SiV^- centers in diamond could be realized with GeV^- centers. Similarly, the future study of the charge, optical, spin properties of $N_CV_{Si}^-$ centers in SiC would benefit significantly from the ongoing study of VV^0 centers in SiC and NV^- centers in diamond. Furthermore, the optical, spin, and charge properties of these systems (SiV^- center in diamond, NV^- center in diamond, VV^0 center in diamond) are ideal platforms to be referred. I thus introduce those SiV^- centers and VV^0 centers related progress in Chapter 2. I then use three chapters to present my work. **Understanding defects' properties from spin, optical, charge, and materials perspectives are the first step toward quantum applications[29].** In the concluding chapter, I outlooked several possible works in this context.

In Chapter 1, I briefly introduce the quantum applications of solid-state color centers and describe the backgrounds and motivations.

In Chapter 2, the general information on group-IV split vacancy color centers in diamond and color centers (V_{Si}^- VV^0 and $N_CV_{Si}^-$) in SiC will be presented. Then some related work on these two systems will be shown. In the end, I present contributions of this thesis in this context.

In Chapter 3, I introduce the coherent manipulation of GeV^- color centers in diamond. Unlike a typical two-level system, a dark state for this system is identified. A three-level model is constructed to explain the photo-physical properties of these emitters.

In Chapter 4, I present our observation of spectral jumps in a Ge-related defect in diamond. The optical properties of these unidentified defects will be presented.

In Chapter 5, I show our study of $N_CV_{Si}^-$ emitters in 4H-SiC. It involves the coherent manipulation of electron spins of $N_CV_{Si}^-$ emitters. To go further, I present our method to generate single $N_CV_{Si}^-$ emitters and their associated optical properties.

In Chapter 6, I conclude the thesis and outlook the following possible works to extend the current studies.

References

[1] ASPECT A. 14 From Einstein, Bohr, Schrödinger to Bell and Feynman: a New Quantum Revolution? [M]. Ondes, matière et Univers. EDP Sciences. 2021: 407-34.

[2] THEIS T N, WONG H-S P. The end of moore's law: A new beginning for information technology [J]. Computing in Science & Engineering, 2017, 19(2): 41-50.

[3] PRESKILL J. Quantum computing in the NISQ era and beyond [J]. Quantum, 2018, 2: 79.

[4] KERR O S, SCHNEIER B. Encryption workarounds [J]. Geo LJ, 2017, 106: 989.

[5] MAVROEIDIS V, VISHI K, ZYCH M D, et al. The impact of quantum computing on present cryptography [J]. arXiv preprint arXiv:180400200, 2018.

[6] SCARANI V, BECHMANN-PASQUINUCCI H, CERF N J, et al. The security of practical quantum key distribution [J]. Reviews of modern physics, 2009, 81(3): 1301.

[7] DEUTSCH I H. Harnessing the Power of the Second Quantum Revolution [J]. PRX Quantum, 2020, 1(2).

[8] DIVINCENZO D P. The physical implementation of quantum computation [J]. Fortschritte der Physik: Progress of Physics, 2000, 48(9-11): 771-83.

[9] CLARKE J, WILHELM F K. Superconducting quantum bits [J]. Nature, 2008, 453(7198): 1031-42.

[10] HäFFNER H, ROOS C F, BLATT R. Quantum computing with trapped ions [J]. Physics reports, 2008, 469(4): 155-203.

[11] WEISS D S, SAFFMAN M. Quantum computing with neutral atoms [J]. Physics Today, 2017, 70(7).

[12] ZWANENBURG F A, DZURAK A S, MORELLO A, et al. Silicon quantum electronics [J]. Reviews of modern physics, 2013, 85(3): 961.

[13] PEZZAGNA S, MEIJER J. Quantum computer based on color centers in diamond [J]. Applied Physics Reviews, 2021, 8(1): 011308.

[14] CASTELLETTO S, BORETTI A. Silicon carbide color centers for quantum applications [J]. Journal of Physics: Photonics, 2020, 2(2).

[15] DEGEN C L, REINHARD F, CAPPELLARO P. Quantum sensing [J]. Reviews of modern physics, 2017, 89(3): 035002.

[16] HENSEN B, BERNIEN H, DRéAU A E, et al. Loophole-free Bell inequality violation using electron spins separated by 1.3 kilometres [J]. Nature, 2015, 526(7575): 682-6.

[17] BOUWMEESTER D, PAN J-W, MATTLE K, et al. Experimental quantum teleportation [J]. Nature, 1997, 390(6660): 575-9.

[18] SANGOUARD N, SIMON C, DE RIEDMATTEN H, et al. Quantum repeaters based on atomic ensembles and linear optics [J]. Reviews of Modern Physics, 2011, 83(1): 33-80.

[19] ATATüRE M, ENGLUND D, VAMIVAKAS N, et al. Material platforms for spin-based photonic quantum technologies [J]. Nature Reviews Materials, 2018, 3(5): 38-51.

[20] AWSCHALOM D D, HANSON R, WRACHTRUP J, et al. Quantum technologies with optically interfaced solid-state spins [J]. Nature Photonics, 2018, 12(9): 516-27.

[21] LIU G-Q, PAN X-Y. Quantum information processing with nitrogen–vacancy centers in diamond [J]. Chinese Physics B, 2018, 27(2).

[22] WEHNER S, ELKOUSS D, HANSON R. Quantum internet: A vision for the road ahead [J]. Science, 2018, 362(6412).

[23] CHEN D, ZHELUDEV N, GAO W B. Building Blocks for Quantum Network Based on Group-IV Split-Vacancy Centers in Diamond [J]. Advanced Quantum Technologies, 2019, 3(2).

[24] POMPILI M, HERMANS S L N, BAIER S, et al. Realization of a multinode quantum network of remote solid-state qubits [J]. Science, 2021, 372(6539): 259-64.

[25] BRADLEY C E, RANDALL J, ABOBEIH M H, et al. A Ten-Qubit Solid-State Spin Register with Quantum Memory up to One Minute [J]. Physical Review X, 2019, 9(3): 031045.

[26] BARRY J F, SCHLOSS J M, BAUCH E, et al. Sensitivity optimization for NV-diamond magnetometry [J]. Reviews of Modern Physics, 2020, 92(1).

[27] SUKACHEV D D, SIPAHIGIL A, NGUYEN C T, et al. Silicon-Vacancy Spin Qubit in Diamond: A Quantum Memory Exceeding 10 ms with Single-Shot State Readout [J]. Physical Review Letters, 2017, 119(22): 223602.
[28] BHASKAR M K, RIEDINGER R, MACHIELSE B, et al. Experimental demonstration of memory-enhanced quantum communication [J]. Nature, 2020, 580(7801): 60-4.
[29] WOLFOWICZ G, HEREMANS F J, ANDERSON C P, et al. Quantum guidelines for solid-state spin defects [J]. Nature Reviews Materials, 2021.
[30] TOGAN E, CHU Y, TRIFONOV A S, et al. Quantum entanglement between an optical photon and a solid-state spin qubit [J]. Nature, 2010, 466(7307): 730-4.
[31] KANAI S, HEREMANS F J, SEO H, et al. Generalized scaling of spin qubit coherence in over 12,000 host materials [J]. arXiv preprint arXiv:210202986, 2021.
[32] AHARONOVICH I, ENGLUND D, TOTH M. Solid-state single-photon emitters [J]. Nature Photonics, 2016, 10(10): 631-41.
[33] BRADAC C, GAO W, FORNERIS J, et al. Quantum nanophotonics with group IV defects in diamond [J]. Nature Communications, 2019, 10(1): 5625.
[34] DRéAU A, TCHEBOTAREVA A, MAHDAOUI A E, et al. Quantum Frequency Conversion of Single Photons from a Nitrogen-Vacancy Center in Diamond to Telecommunication Wavelengths [J]. Physical Review Applied, 2018, 9(6): 064031.

Chapter II Experimental methods and literature review

In the second quantum revolution, a distinct difference compared to the first phase is the capability of manipulating particles at a single level (photon, electron, ions)[1]. With two decades of study of solid-state emitters, people have gained rich experience in the generation, characterization, and manipulation of single defects[2]. The single-photon emission is generally characterized by the Hanbury Brown-Twiss experiment[3]. Color centers like NV^- centers and VV^0 centers are 'atom-like'[4]. An isolated SPE comes with a single electron interface if the SPE is a paramagnetic system.

Since color centers are 'atom-like', their optical and spin properties are then closely linked to their energy levels. The two basic approaches to reveal their energy levels are the resonant laser excitation[5] and the optically detected magnetic resonance (ODMR) spectroscopy[6]. These methods also enable estimations of systems' optical and spin coherence time. To scale up the qubits, it is critical to generate SPEs whose emissions are indistinguishable[7]. The indistinguishability is estimated with the Hong-Ou-Mandel experiment.

In this regard, I will introduce the basic experimental methods in section 2.1, including the HBT experiment, HOM experiment, resonant excitation, and ODMR.

In section 2.2, I introduce the physical properties of two main color center hosts: diamond and SiC. Their hosted defects are also introduced.

In section 2.3, I review the basic properties of group IV defects in diamond. **Beyond this, I present several pioneer works that laid a foundation for realizing quantum network.** In detail, the indistinguishable photon generation is a crucial step toward spin-spin entanglement between different SiV^- emitters[8]; the all-optical manipulation of SiV^- spins demonstrate the construction of a Λ-system which is a crucial ingredient for spin-photon entanglement[9]; the microwave-assisted spin rotation shows the possibility to realize spin polarization and manipulation via microwave, and the spin coherence time could be estimated with pulsed microwave operations[10]; fabrication of SiV^- in diamond nanostructures with narrow emission linewidth paves the way for building up a scalable quantum network[11]. Though these works are mainly performed with the SiV^- center in diamond, similar works could be realized on other group IV split vacancy centers given that they shared similar energy level structures.

In section 2.4, I categorized V_{Si}^-, VV^0, and $N_CV_{Si}^-$ centers in SiC into the same family for the following reasons: (1) they have a non-zero D (zero-field splitting) value, and the spin states could be polarized via off-resonant excitation[2]; (2) they reside in the same host; thus material

or device engineering technologies could be shared among them. Similar to section 2.3, I review the progress in the SiC color centers community. They include indistinguishable photon generation for V_{Si}^- centers in SiC[12]; coherent manipulation of VV^0 spin; tunable emission wavelengths of VV^0 centers in SiC, which would enable indistinguishable photon generation from different VV^0 emitters[13, 14]. These works demonstrate SiC emitters as promising candidates for quantum communication and quantum computation.

2.1 Experimental methodologies

2.1.1 HBT experiment

Single-photon sources (SPSs) refer to sources that emit no more than one photon within a specific time. This behavior could be readily characterized with a second-order coherence measurement ($g^{(2)}(\tau)$). The $g^{(2)}(\tau)$ function describes the intensity correlation among a train of photons. In the time domain, it is given by:

$$g^{(2)}(\tau) = \frac{< I(t)I(t+\tau) >}{< I(t) >^2} \tag{2.1}$$

Where $\boldsymbol{\tau}$ is defined as the time interval of two photons, **I(t)** represents the intensity at time t, the < > refers to a statistical average. In practice, the Hanbury Brown-Twiss (HBT) setup is employed to characterize a specific source. With this function, it is possible to distinguish sources of the following cases:

(A) In the ideal case, the SPS is in the Fock state, thus $g^{(2)}(\tau) = 1$ and $g^{(2)}(0) = 0$. Figure 2.1a shows a dip down to zero, called the antibunching effect. In practice, the $g^{(2)}(0)$ is always greater than 0 because of the imperfection of an SPS. People treat a photon source as an SPS when its $g^{(2)}(0)$ smaller than 0.5.

(B) Coherent state. The $g^{(2)}(\tau) = 1$ (Figure 2.1(b)). The photon number within a given time interval **t** satisfies the Poisson distribution. This Poisson distribution reflects the random time intervals between photons. However, the photons are not bunched.

$$p(k) = e^{-n}\frac{n^k}{k!} \tag{2.2}$$

Where **k** is the emission photon number and **n** is the average photon number. It is worth mentioning that the $g^{(2)}(\tau)$ for a faint laser reaching a single-photon level remains at 1.

(C) For thermal light, it can be characterized as $g^{(2)}(\tau) \geq 1$ and $g^{(2)}(0) \geq g^{(2)}(\tau)$ (Figure 2.1(c)). An evident bunching effect could be observed at $\tau = 0$. In other words, there is a high probability to detect photons simultaneously with the two arms of the HBT setup. The photon number satisfies a super-Poisson distribution.

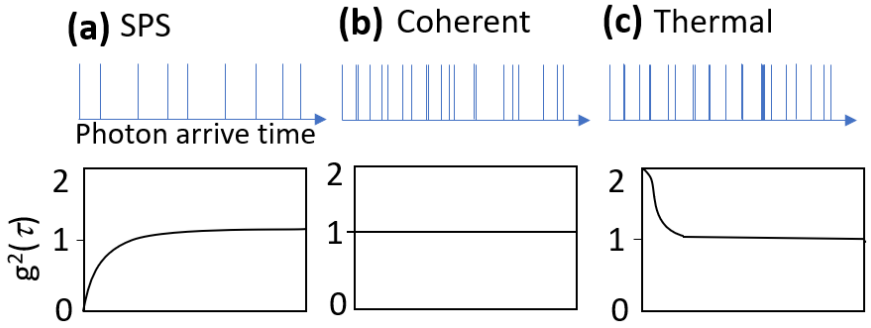

Figure 2.1: Photon trains and $g^{(2)}(\tau)$ of three types of photon source. (a) Single-photon source. (b) Coherent source. (c) Thermal light source.

With decades of efforts, people have realized single-photon emission on many systems like single-emitter systems (neutral atoms, ions, molecules, quantum dots, and color centers), unidentified emission sources (gallium nitride and 3C-SiC)[15, 16], ensemble atoms with collective excitation, parametric down-conversion and four-wave mixing based on non-linear crystals[17]. This thesis focuses on color centers in wide-bandgap materials.

2.1.2 Hong-Ou-Mandel experiment

In the past two decades, people have discovered many kinds of color centers SPSs. Nevertheless, only a few of these systems are demonstrated to show indistinguishable emission, e.g., SiV^- centers in diamond[8], NV^- centers in diamond[7], and V_{Si}^- centers in SiC[12]. Indistinguishable emission is important since it is the prerequisite for the entanglement distribution between separated nodes. **The indistinguishable emission requires photons generated by an SPE or several SPEs to have the same frequency, polarization, and spatial and temporal extent.** In practice, the degree of indistinguishability of an SPE or two SPEs is estimated by the HOM experiment[18]. In Figure 2.2, photons from an SPE which are split into two paths or photons emitted by two SPEs, are guided to a 50/50 beam splitter. If the photons of the two paths are indistinguishable and impinge simultaneously on the beam splitter, both photons come out at the same port. These two output ports are connected to an HBT setup. Ideally, a $g^2(0) = 0$ could be obtained given that photons are indistinguishable. **In practice,**

emitters in solid-state hosts suffer from spectral diffusion or unstable emission wavelengths, resulting in reduced indistinguishability.

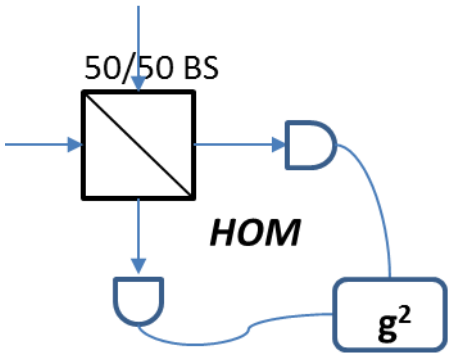

Figure 2.2: HOM setup. Photons from two separated channels impinge on a 50/50 beam splitter. The beam splitter's output is guided to two single-photon detectors to realize g^2 measurement.

2.1.3 Optically detected magnetic resonance

Single NV^- center in diamond was firstly reported in 1997[6]. Meanwhile, the ODMR spectrum of a single NV^- electron spin was demonstrated. Since then, the energy levels of the NV^- center have been revealed with the help of experimental[19] and theoretical studies[20]. Figure 2.3(a) shows the atomic structure of the NV^- center in diamond[21], in which a nitrogen atom replaced a carbon atom with an adjacent atom being replaced by a vacancy. NV centers in diamond have two reported optically active charge states: a neutral charge state (NV^0) whose ZPL is located at 575 nm, and a negatively charged state with a ZPL of 637 nm (Figure 2.3(b)). The ZPL ratio of NV^- centers is about 3%. The NV^- centers have 6 electrons which are filled in 4 orbitals. While two orbitals are fully occupied, the other two are half-filled. This results in an S = 1 system. Figure 2.3(c) shows the simplified energy levels of NV^- centers. It includes a spin-triplet orbital-singlet ground state and a spin-triplet orbital-singlet excited state. The energy difference between the ground $m_s = 0$ and $m_s = \pm 1$ state is called zero-field splitting (ZFS).

The spin states of NV^- centers could be initialized into the S = 0 with both resonant and off-resonant excitation. Elections in excited states have two decay channels. The spin conserved radiative decay gives emission into both the ZPL and the associated phonon sideband (PSB), and the spin filliped channel gives no emission in the visible range. The spin initialization is possible because about 40% of electrons in $m_s = 1$ states decay via the ^1A channel, which is coupled to the ground states with the same strength. By contrast, the $m_s = 0$ hardly decay via the ^1A channel. In this regard, electrons could be polarized into the $m_s = 0$ sublevel after several

pumping cycles. After being optically polarized into the bright $m_s = 0$ state, spins could be flipped into the $m_s = \pm 1$ states with a resonant oscillating magnetic field. Since the $m_s = \pm 1$ states give lower emission than the $m_s = 0$ state, the emission under a resonant MW excitation gives lower counts when the MW is not resonant with the ground splitting (Figure 2.3d). Since the $m_s = \pm 1$ states are degenerated, giving one dip at zero magnetic fields. When an external magnetic field is applied along the NV axis, the degeneracy of $m_s = \pm 1$ states is lifted due to the Zeeman effect. The transitions from $m_s = 0$ to $m_s = -1$ and $m_s = +1$ states are observed.

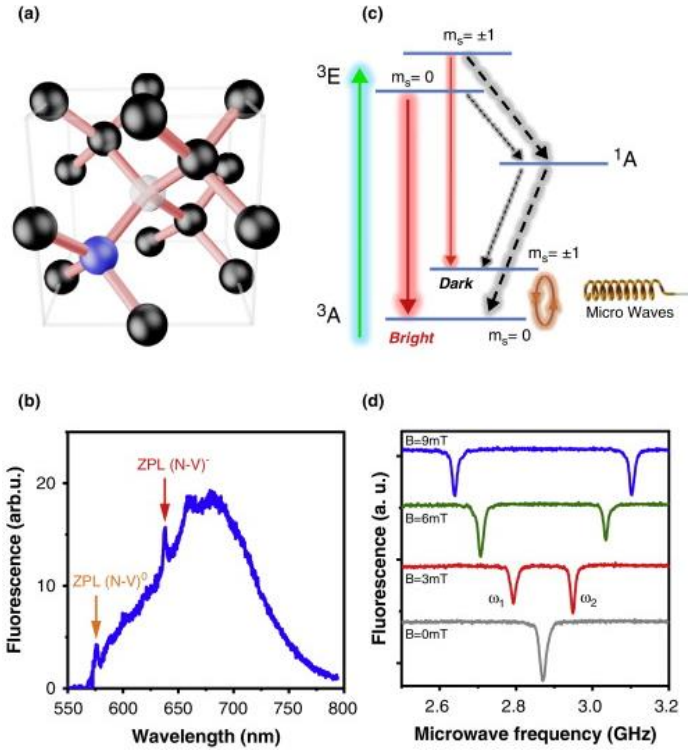

Figure 2.3: Optical and spin properties of NV centers in diamond[21]. (a) The atomic structure of a single NV center in diamond. Dark: carbon atoms; blue: nitrogen atom; white: vacancy. (b) Emission spectra of neutral NV centers and negatively charged NV centers in diamond. (c) Energy level structure of the NV^- center in diamond and the allowed transitions among them. The green arrow refers to the laser excitation; the red arrows refer to the radiative transitions; the grey arrows refer to the inter-system crossing processes. (d) ODMR spectra of NV^- centers at different magnetic fields. Reproduced with permission [21]. Copyright 2014, The Authors, published by Elsevier B.V.

Since the spins of NV^- centers could be initialized with an off-resonant laser, then spin operation at room temperature is possible. This enabled the application of NV^- spin into sensing magnetic fields, electrical fields, temperature, and pressure[22]. The NV^- center has recently found new application frontiers, including biology and condensed matter physics. Similar to the NV^- center, other platforms are found to share similar spin-photon interfaces, e.g., the

negatively charged boron vacancy in hexagonal boron nitride[23], the VV^0 in silicon carbide[24], the NV^- centers in SiC[25], and the V_{Si}^- center in SiC[26] (S = 3/2).

2.1.4 Resonant excitation of NV^- centers in diamond

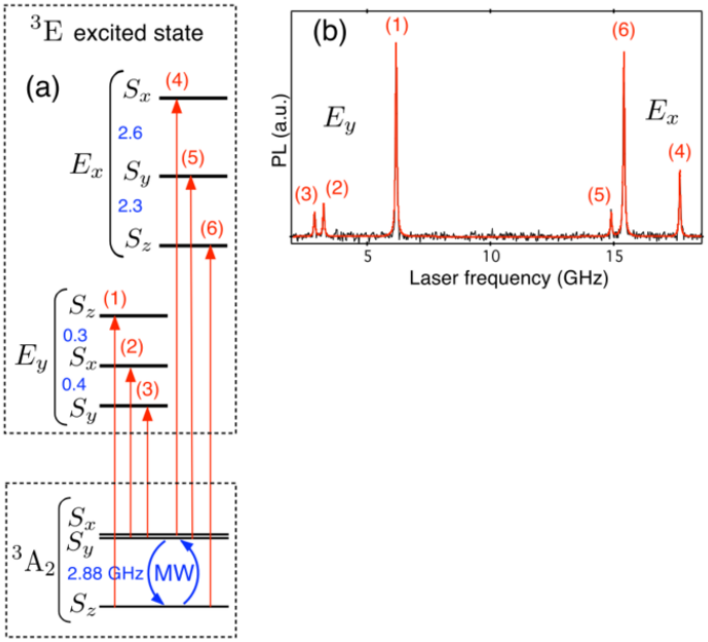

Figure 2.4 Resonant excitation of a single NV^- center in diamond[19]. (a) Energy levels of a single NV^- center in diamond. (b) Resonant laser excitation resolved 6 transitions at low temperatures. Read lines are Lorentzian fitting of the transitions. Reproduced with permission [19]. Copyright 2009, American Physical Society.

As discussed in section 2.1.3, the room temperature spin manipulation has enabled the application of NV^- center into quantum sensing. For sensing applications, what matters is the ODMR contrast and spin coherence time but the photon frequency. By contrast, the application of NV^- centers into quantum network demands indistinguishable photons from different sources. **In practice, only ZPL photons are applicable for spin-photon entanglement or are used to connect several nodes.** Nevertheless, there are several spin-conserved transitions within the ZPL range. It then demands people to select one transition for spin-photon entanglement.

Figure 2.4a shows the energy levels of the NV^- center at low temperatures. It includes a spin-triplet, orbital-singlet ground state, and a spin-triplet, orbital-doublet excited state. It thus allows six transitions (Figure 2.4b). People can then create Λ-systems to realize the spin-photon entanglement. People frequently employ a resonant excitation to identify the energy levels and quantify photons' frequencies. When performing the resonant excitation, target emitters are excited with a wavelength-tunable laser, and their emission can be collected with a long-pass

filter or can be collected with a cross-polarization scheme to suppress the laser. Apart from the emission frequencies of the photons, the resonant excitation could provide more information of the emitters including their emission stability and emission linewidth. A photon source with highly indistinguishability requires stable emission wavelength, stable emission counts, and narrow emission linewidth (preferably near the lifetime limited).

2.2 Diamond and Silicon carbide hosts

	Si[27]	3C-SiC[27]	4H-SiC[27]	6H-SiC[27]	15R-SiC[28]	Diamond[29]	GaN[30]
Crystal structure	Diamond	Cubic	Hexagonal	Hexagonal	Hexagonal	Cubic	Hexagonal
Bandgap (eV)	1.1	2.39	3.265	3.023	2.986	5.5	3.4
Lattice constant (A)	5.43	a=4.36	a=3.08 c=10.05	a=3.08 c=15.12	a=3.08 c=37.70	3.57	a=3.186 c=5.186
Density (g/cm3)	2.33	3.21	3.21	3.21		3.53	6.1
Debye Temperature (K)	640	1200	1300	1200		2200	600
Breakdown field (10^5V/cm)	3		30	25		100	30
Refractive Index	3.5	2.55	2.56	2.55		2.4	2.43
Transparency range (um)	1.1-5.5		0.37-5.6			0.22-20	0.36-7

Table I: Physical properties of color center host materials.

Table I listed several kinds of semiconductor materials hosting color centers. Among them, silicon, SiC, and gallium nitride (GaN) are intensively studied in the industry because of their applications in power electronics. With constant efforts of both industry and research communities, materials including Si, SiC, GaN are nano-fabrication friendly. People have mastered techniques like p- and n-doping, inch-scale growth, nanofabrication, and refining. By contrast, these studies on diamond lagged. It is generally difficult to dope the diamond, making it challenging to drive defects in diamond electrically. A 2-inch SiC wafer typically has the same price as a 2 mm by 2 mm high-purity diamond. Further isotope purification of the diamond will induce additional costs. Moreover, there is no matured nanofabrication recipe, making it is challenging to scale up the diamond nanostructures.

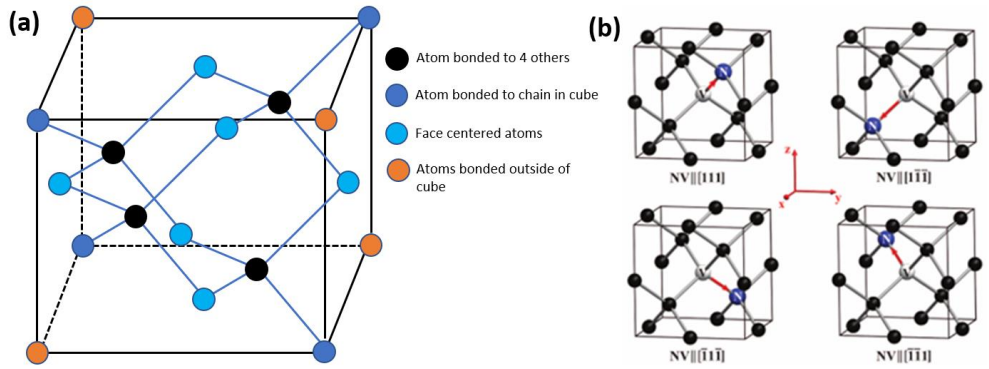

Figure 2.5: (a) Diamond unit cell. (b) NV^- centers in diamond (four NV symmetry axes are shown)[31]. Reproduced with permission [31]. Copyright 2012, American Physical Society.

Diamond. Diamond is made of carbon atoms which are arranged in a cubic crystal structure (as shown in Figure 2.5). The diamond lattice could be treated as two face-centered cubic lattices, with one made of the orange and light blue dots in Figure 2.5(a) and another the blue dots. The sublattice is made of blue dots displaced along the cubic diagonal by ¼. Each carbon (the blue dot) is covalently bonded to four nearest atoms (four dark dots). This arrangement is so rigid that it just allows the presence of two kinds of impurities (boron and nitrogen). The diamond has an indirect wide bandgap of 5.5 eV, making it transparent in the visible range if no impurity is involved. However, with the presence of nitrogen or boron defects and possible linked vacancies, the diamond is no longer transparent in the visible range but will show absorption and give emission in the visible range. We call the defects that give diamond color as color centers. One of the most studied color centers is NV^- centers, as shown in Figure 2.5(b)[31]. There are four N-V axes in diamond (Figure 2.5(b)). For single NV center manipulation, an electronic grade diamond host should be employed and could be purchased from companies.

Silicon carbide. Silicon carbide is a binary compound semiconductor in which half atoms are silicon and the rest carbon. There are more than 200 polytypes of SiC, among which the 3C, 4H, and 6H-SiC are most studied as hosts of quantum emitters. The SiC are good hosts of quantum emitters in terms of the following aspects[32]: (1) The matured inch scale growth technique; (2) The matured n- and p-doping technologies; (3) The heteroepitaxy of SiC on a silicon wafer; (4) The matured nanofabrication techniques.

Figure 2.6 shows the stacking sequence of 3C-, 4H-, and 6H- SiC, and an additional stacking sequence of 4H-SiC with stacking fault. The presence of stacking faults will introduce more Si-C environments. While it is possible to grow 3C-SiC on a silicon wafer, it is necessary to

grow 4H-SiC on the 4H-SiC substrate to get a high-quality SiC host. The high purity SiC layer with a thickness of tens μm provides a clean environment which allows the generation and isolation of single defects within this layer. Unlike diamond defects whose emissions are in the visible range, the SiC defects like silicon-vacancy (V_{Si}), divacancy ($V_{Si}V_C$), and nitrogen-vacancy (N_CV_{Si}) give emission in the near-infrared window[32-34]. As the labeling indicates, a vacancy replaces an atom at a silicon site for the V_{Si}^- center; vacancies would replace a pair of adjacent Si-C atoms for the VV center, and a nitrogen atom would occupy a carbon site while leaving its nearest silicon site as a vacancy for the $N_CV_{Si}^-$ center. Moreover, if no stalking fault is considered, there is only one cubic site for both silicon and carbon atoms in 3C-SiC; there are h and k sites in 4H-SiC; there are h, k1, and k2 sites in 6H-SiC. As a result, there is one type of VV or N_CV_{Si} centers in 3C-SiC; 4 in 4H-SiC; 6 in 6H-SiC. If stacking fault is considered, several extra VV defects in 4H-SiC are reported (Figure 2.6(d))[32].

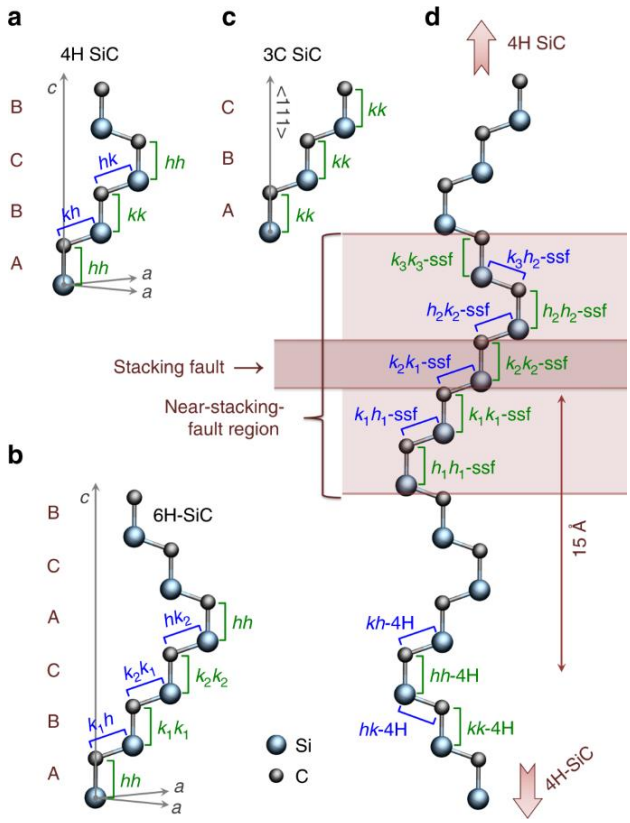

Figure 2.6: SiC polytypes[35]. (a) 4H-SiC with ABCB stacking sequence. (b) 6H-SiC with ABCACB stacking sequence. (c) 3C-SiC with ABC stacking sequence. (d) 4H-SiC with stacking fault. Reproduced under the terms of a creative commons CC-BY international license [35]. Copyright 2019, The Authors, published by Springer Nature.

2.3 Group IV split vacancy centers in diamond

2.3.1 Energy levels of group-IV split vacancy centers in diamond

While the NV^- center in diamond is occupied at two nearest sits of carbon atoms, the silicon-vacancy (SiV^-) center in diamond has silicon located between two vacancies (as shown in Figure 2.7). The different molecule configurations give them different symmetry, C_{3v} for NV^- centers, D_{3d} for SiV^- centers.

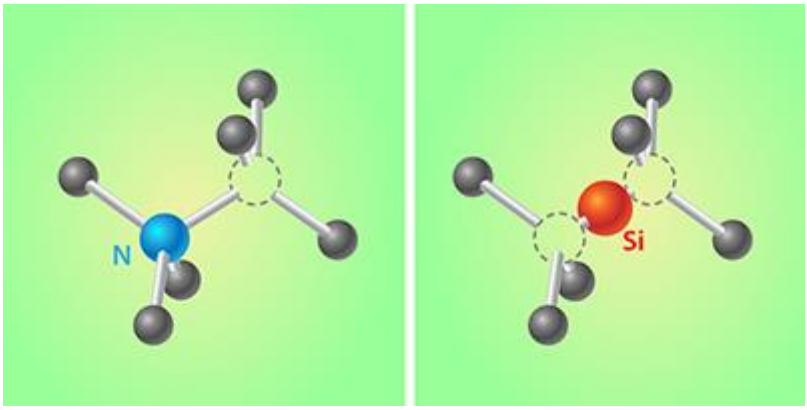

Figure 2.7: Molecule configuration comparison of NV^- centers in diamond and SiV^- centers in diamond[36]. Reproduced with permission [36]. Copyright 2014, American Physical Society.

This D_{3d} symmetry gives group IV split vacancies degenerated doublet excited and ground orbital states. **The degeneracy could be lifted via a Jahn-Teller interaction or a spin-orbit coupling (shown in Figure 2.8(a)), producing ground state splitting (Δ_{GS}) and excited-state splitting (Δ_{ES}).** The transitions between the ground states and excited states give a four-line structure that could be resolved at low temperatures. Due to the high Debye-Waller factors of the group IV split vacancy centers (more than 70 % for diamond SiV^{--} centers verse 3% for diamond NV^- centers), it is possible to observe their ZPLs even at room temperature (as shown in Figure 2.8(b)). Since their emission is coupled to phonon baths at ambient temperature, the fine structures related to the orbital transitions could not be identified at room temperature. Figure 2.8(b) shows that the SiV^- centers exhibit the longest emission wavelength while the PbV^- centers the shortest one. However, the GeV^- centers give a shorter emission wavelength than the SnV^- centers. **People are interested in the heavier impurity because it has a larger spin-orbit coupling and leads to a larger Δ_{GS} and Δ_{ES}.** In practice, the PbV^- has a Δ_{GS}= 5700 GHz[37] and Δ_{ES}= 6400 GHz (calculated)[38], which is more than 100 times and 20 times greater

than SiV^- centers' splitting Δ_{GS} = 50 GHz and Δ_{ES}= 267.5 GHz, respectively.[39] **The benefits of larger splitting are two folds: reduced phonon dephasing and robust optical cyclicity[40].**

Each orbital level could be further split into two spin sublevels when an external magnetic field is applied. As shown in Figure 2.8(a), the optical transitions could happen among the ground states labeled as |1>, |2>, |3>, |4> and the excited states |A>, |B>, |C>, |D> when the vector magnetic field is appropriately aligned with respect to the symmetry axis of the group IV split vacancy centers[41]. **Then several Λ systems could be prepared, making them applicable for spin-photon entanglement.**

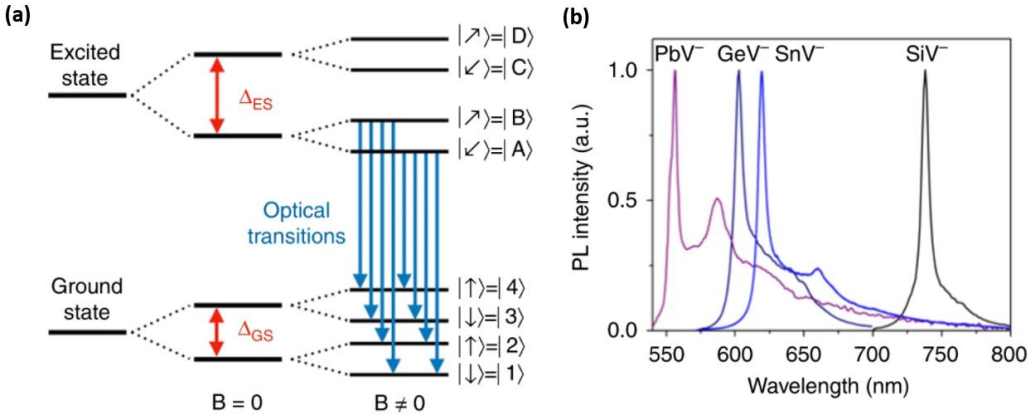

Figure 2.8: (a) Energy structures of group IV split vacancy centers without and with a magnetic field. (b) Room temperature emission spectra of the four kinds of color centers in diamond[42]. Reproduced under the terms of a creative commons CC-BY international license [42]. Copyright 2019, The Authors, published by Springer Nature.

Apart from the high ZPL ratio of the group IV split vacancy centers, another advantage of these defects over the diamond NV^- center is the inversion symmetry-protected optical transitions that are not sensitive to the electric field to the first order[8]. **Thanks to this, the optical transitions of group IV centers suffer less spectral diffusion and show a narrower distribution of transition frequencies than the diamond NV^- centers.** People have observed lifetime limited linewidth on SiV^-[8], GeV^- [43], and SnV^- centers [44]. Moreover, *Alp et al.* have demonstrated indistinguishable emission of two SiV^- color centers[8].

In the following, I will review several works on group IV color centers in diamond which demonstrate themselves as a suitable spin-photon interface.

2.3.2 Indistinguishable emission from separated SiV^- centers in diamond

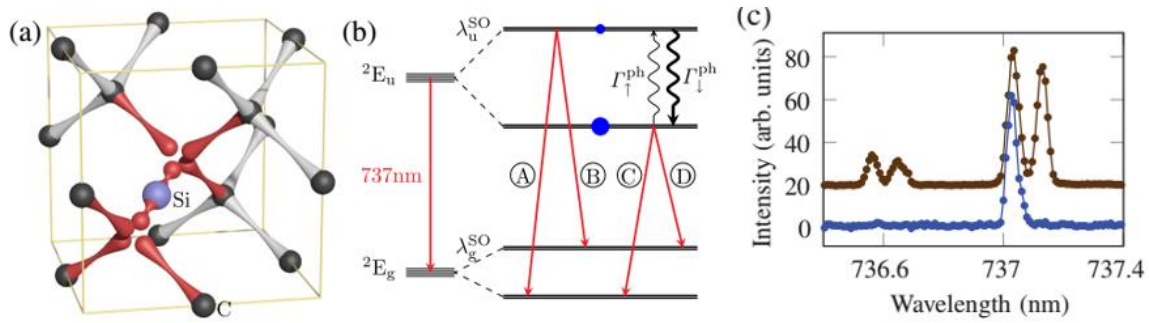

Figure 2.9: (a) Molecule configuration of a SiV^- center in diamond. (b) The SiV^- center energy level at cryogenic temperature. (c) ZPL spectrum (brown line) and etalon filtered transmission (dark blue line)[8] spectrum of single SiV^- center. Reproduced with permission [8]. Copyright 2014, American Physical Society.

Demonstration of indistinguishable emission is a vital step to interface quantum nodes via flying qubits. People have demonstrated indistinguishable emission of two separated SiV^- emitters by selecting them with resonant excitation. This facility is closely linked to the previously mentioned symmetry properties of diamond SiV^- color centers[8]. Figure 2.9(a) presented the molecular configuration of a SiV^- center in diamond. Figure 2.9(b) shows the four emission peaks labeled as A, B, C, and D, where C and D correspond to the intensive ones (Figure 2.9(c)). The transition C of two SiV^- color centers are chosen for two-photon interference measurement.

As the SiV^- centers' optical transitions are insensitive to the electric field, the authors found two emitters with perfect spectral overlap among massive centers created via ion implantation. Figure 2.10(a) and (b) show two emitters situated 30 μm away with an emission wavelength difference of 42 MHz. Their linewidth is about 100 MHz (as shown in Figure 2.10(c)), which is comparable with the lifetime transform-limited linewidth (94 MHz). The emission of two sources is tuned to impinge simultaneously on a beam splitter to perform a two-photon interference experiment (HOM experiment). The second-order correlation of two outputs of the beam splitting is further estimated by controlling the emitters' polarization with polarizers. The $g^{(2)}(\tau)$ measurement in Figure 2.10(d) shows both the distinguishable and indistinguishable emission cases. When indistinguishable (identical polarization), a dip of 0.25 (pink data) is obtained; likewise, a shallow dip (green data) of 0.75 is associated with the other case (orthogonal polarization).

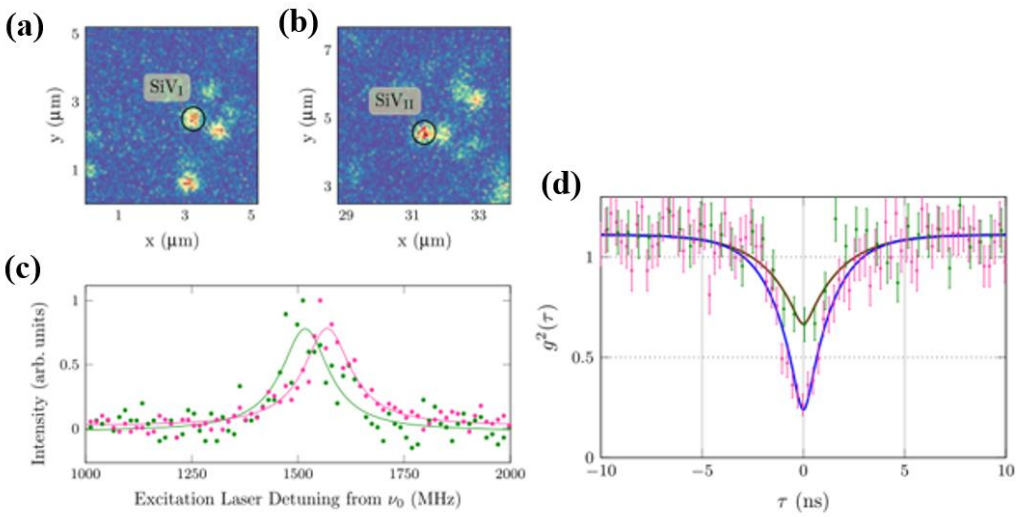

Figure 2.10: Two indistinguishable SiV^- SPEs (a, b) with their corresponding coordinates shown. (c) Resonant laser determined emission spectra of SiV_I and SiV_{II} centers. (d) HOM interference experiment. The $g^{(2)}(\tau)$ is measured when polarizations of both emitters are identical (pink data) and are orthogonal (green data)[8]. Reproduced with permission [8]. Copyright 2014, American Physical Society.

2.3.3 Manipulation of orbital and spin states of group IV split vacancy centers

The ability to initialize, manipulate, and readout of a spin state is the key to realizing quantum applications like quantum computation and quantum sensing. During the last decades, people have demonstrated the coherent manipulation of both the orbit and spin degrees of freedom of SiV^-[41, 45-48] and GeV^-[43] centers in diamond. The study of SnV^- and PbV^- centers lagged because their controllable generation is much later than the other two defects. People have demonstrated all-optical manipulation of the SiV^- emitters' orbital and spin states and have estimated the spin properties of SiV^- and GeV^- centers with optical and microwave pulses.

2.3.2.1 All-optical manipulation of the SiV^- center orbital states

Figure 2.11(a) and (b) show the coherent manipulation of a SiV^- center by resonantly driving the transition C and B with different pulse laser areas (labeling refers to Figure 2.9). In practice, the laser pulse length is fixed to be 12 ps, while the laser power could be changed to reach different rotation angles. As shown, it is possible to coherently rotate the transition C up to 10π and more than 6π for transition B. Known the π-pulse area, the authors perform Ramsey interference experiment with these two transitions to estimate the coherence time of excited states. The interference envelops with respect to varied pulse areas are shown in Figure 2.11(c), from which the coherence times of the two corresponding excited states are extracted. The coherence time is about 1 ns for the lower excited state and is about 0.4 ns for the upper excited

state. The coherence time limiting factors for the two transitions are different: the lower excited state coherence time is limited by the orbital lifetime (1.85 ns), while the upper excited state one is attributed to the fast decay from the upper excited state to the lower excited state (0.4 ns). **Given the picosecond pulse length, this coherence time may permit hundreds to thousands of gate operations[9].**

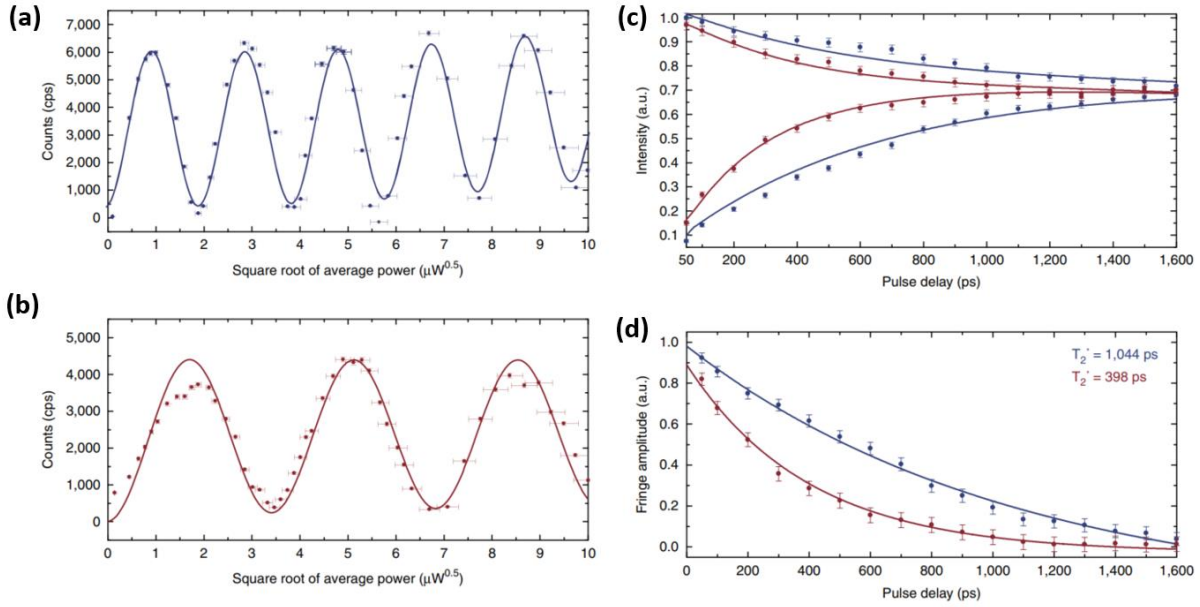

Figure 2.11: Coherent manipulation of SiV^- center orbital states. Optical one photon Rabi oscillations for picosecond laser pulses resonant with (a) transition C and (b) transition B (Labelling refers to Figure 2.8). (c) Optical one photon Ramsey interferences for transition C (blue) and transition B (red). (d) Extracted Ramsey interference fringe amplitude with varying pulse delay (blue for transition C and red for transition B). The excited state coherence times (T_2^*) are extracted from the decay (T_2^* = 1044 ps for transition C and T_2^* = 398 ps for transition B)[9]. Reproduced under the terms of a creative commons CC-BY international license [9]. Copyright 2016, The Authors, published by Springer Nature.

2.3.2.2 All-optical manipulation of the SiV^- center spin states

As the previous section shows, the short excited states lifetime imposes an upper limit on the coherence time of the studied states**. A better choice for applications like quantum memory is the utilization of ground spin states.** Several groups have demonstrated the all-optical manipulation of SiV^- center spins in diamond. They also estimated the spin coherence time with either the coherent population trapping (CPT)[41, 46] or the optical Hahn Echo measurement[49].

To get access to the spin degree of freedom, an external magnetic with a proper direction to the SiV^- center symmetry axis should be applied. Figure 2.12(a) shows four simplified spin levels, with the upper two corresponding to the excited state and the lower two to the ground state. A laser resonant with the transition D_1 is applied to prepare the electron into the ground spin-up sublevel. The population on this spin-up state could be read out with a D_2 resonant pulse. As shown in Figure 2.12(a), a higher photoluminescence intensity is observed if there is D_1 before the D_2 reading pulse. The estimated spin initialization fidelity is about 78**%. By varying the dark interval between D_1 and D_2, it is also possible to estimate the ground state orbital lifetime, which is inversely proportional to the temperature (Figure 2.12(a)).** With such a Λ-scheme composed of a common excited state and two ground states of orthogonal spin states, it is possible to prepare a dark superposition state of spin-up and spin-down ground states. The dip width of the spectrum could estimate the coherence between the two ground states. A dip width of 4.5 MHz is extracted by eliminating the power broadening effect, which equals a spin coherence time of $T_2^* = 35$ ns (Figure 2.12(b)). This value is limited by the phonon bath or the ground state orbital lifetime. **In turn, this short spin dephasing time requires the research on group IV centers whose D_{GS} has a larger splitting.** With the CPT experiment, the author observed the ^{29}Si nuclear spin-induced fine structure (shown in Figure 2.12(c)). Similar work could be found in [41].

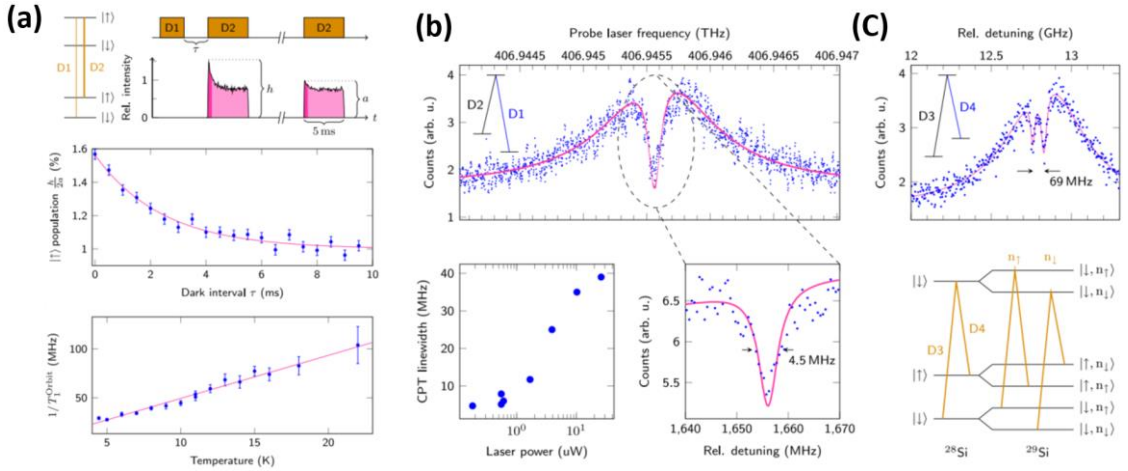

Figure 2.12: All-optical initialization and coherent preparation of SiV^- spins in diamond. (a) Initialization of SiV^- spins (up). Estimated spin polarization ratio (middle) and orbital lifetime (down). (b) Preparation of coherent dark states. The spin coherence time is extracted from the dip width $T_2^* = 35$ ns. (c) Nuclear spins induced double dip[46]. Reproduced with permission [46]. Copyright 2014, American Physical Society.

In 2018, Jonas et al. explored the ground spin coherence properties by lifting the phonon-induced limitation (sample is cooled down to 40 mK). The coherence properties are then studied by employing optical Rabi, Ramsey, and spin-echo measurement[49]. Nevertheless, the T_2^* is merely about 29 ns at 40 mK and 20 ns at 3.7 K, comparable with the previous case at 3.7 K. The author analyzed the spin coherence at a different temperature, based on which they attribute the residual decoherence source to electron spin bath[49]. This spin bath is related to the residual N impurity centers (P1 centers).

2.3.2.3 Manipulation of the GeV^- center spin states with microwave

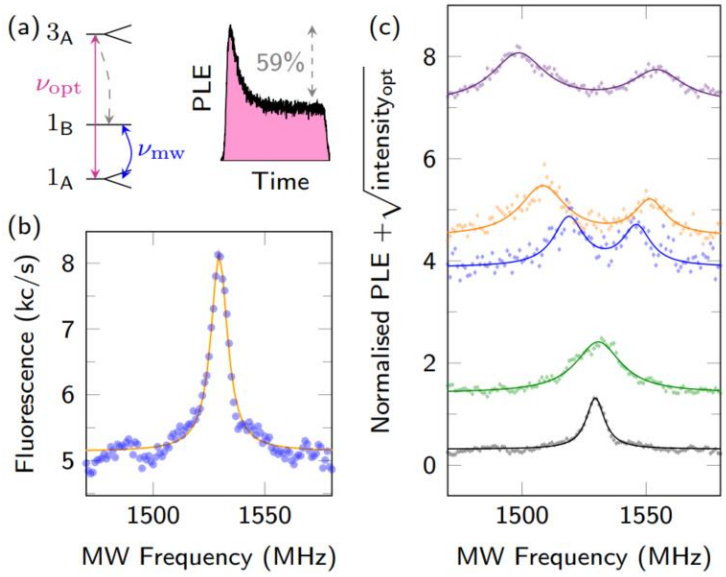

Figure 2.13: Microwave manipulation of a GeV^- center[43]. (a) Spin sublevel of the GeV^- center. 1_A 1_B refers to ground spin sublevels and 3_A excited spin sublevel. The spin is initialized into 1_B with a laser resonant with the transition from 1_A to 3_A. (b) Microwave-assisted spin-flip from 1_B to 1_A. (c) Strong laser pumping induced the Autler-Townes effect. The 1_A sublevel splitting is resolved with microwave sweeping. Reproduced with permission [43]. Copyright 2017, American Physical Society.

Upon applying an external static magnetic field, the energy difference between the spin-up and spin-down sublevels generally ranges from MHz to GHz. This is just within the microwave frequency range. Hence, apart from the previously mentioned all-optical spin manipulation, another feasible approach is the microwave. A representative work on the optical and microwave manipulation of the GeV^- center spin is shown in Figure 2.13. The degenerated ground spin doublet is first lifted by applying an external magnetic field. The system could be initialized by a resonant excitation, namely the 1_A-3_A transition (Figure 2.13(a)). The exact energy split between 1_A and 1_B is resolved by sweeping the microwave frequency. A peak is

observed when the microwave frequency is resonant with the 1_A-1_B transition (Figure 2.13(b)). Upon high laser power resonant excitation, the 1_A-3_A levels will be further split by the electric field into two dressed states, respectively. Figure 2.13(c) shows that spin flipped transitions from 1_A doublet to 1_B are well resolved. To learn the spin dynamics, microwave pulse sequences like Rabi, Ramsey, Hahn Echo, and Carr-Purcell-Meiboom-Gill (CPMG) should be employed. The related work could be found in[50].

2.3.4 Integration into diamond nanostructures

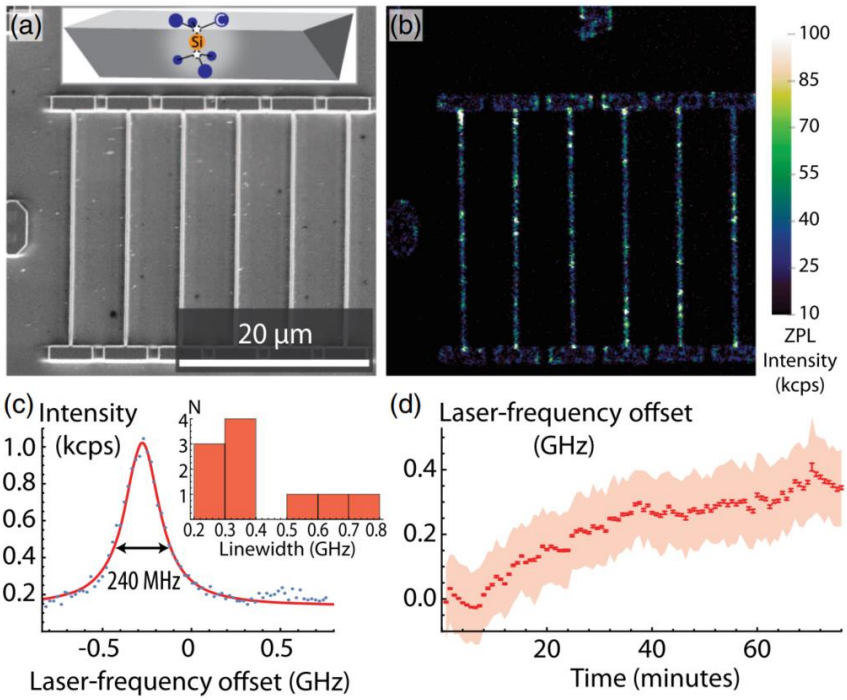

Figure 2.14: Optical properties of a SiV^- color center residing in diamond nanostructures[11]. (a) Scanning electron images of six nanobeam waveguides. (b) 2D confocal mapping of SiV^- color centers' emission. (c) The linewidth of a representative SiV^- center inside a nonwaveguide. (d) Spectral diffusion of the emitter in (c). Reproduced with permission [11]. Copyright 2016, American Physical Society.

In the past decades, nanofabrication techniques for diamond have been mastered with the combined efforts of the whole color center community. Nanostructures like micro-ring cavity[51], nanobeam cavity[52], photonic crystal cavity[53] have been fabricated to boost the light-matter interaction. Meanwhile, incorporating color centers into nanostructure will benefit the fabrication of quantum photonic integrated circuits. The group IV color centers, benefiting from their robust optical transitions, are better candidates for nanostructures-based quantum devices than the diamond NV^- center system. Lukin's group did systematic work on the demonstration of scalable quantum networks with group IV color centers in diamond [42, 52, 54].

The optical linewidth of an emitter is crucial since it reflects the achievable coherence time of an excited state. Ideally, the linewidth should be lifetime limited. Nevertheless, atomic defects in solid are not isolated from the host. **As a result, the emission linewidth is determined by both the homogeneous and inhomogeneous broadening processes.** While the previous one is determined by the direct photon emission and the dephasing in the excited states, the latter is related to the local strain and the fluctuating electrical field. For example, the lifetime limited linewidth for diamond NV^- centers is estimated to be 14 MHz, but the observed linewidth is 10 times[55] broader for NV^- centers in bulk diamond and 100-200 times[56] broader for NV^- centers in diamond nanostructures. **Thus, it is challenging to employ diamond NV^- centers for scalable nanophononics.** However, it is worth mentioning that the second broadening process could be mitigated by using a proper sample preparation protocol and a suitable defect. In terms of the strain, it is possible to create a low-strain environment for defects by either producing defects during CVD growth or relaxing the strain with a proper annealing protocol [11, 55]. **Regarding the fluctuating electric field, one needs to seek for defects that exhibit vanished static electric dipole moments.**

As shown in Figure 2.14, Si^+ ions are implanted into nanobeam waveguides (Figure 2.14(a)) and SiV^- centers are activated upon high-temperature annealing (bright spots in Figure 2.14(b)). The typical optical linewidth without phonon broadening is about 240 MHz (Figure 2.14(c)), which is comparable to SiV^- in bulk diamond[11]. Compared to diamond NV^- centers, the emission wavelength of the investigated SiV^- center in diamond nanostructure shows a slow spectral diffusion (Figure 2.14(d)). In this regard, the group IV split vacancy centers are promising candidates for the quantum photonic integrated chips. **The capability of maintaining SiV^- centers' optical properties in diamond nanostructures has indeed promised the following work quantum nonlinear optics with GeV^- centers[57], quantum entanglement between two SiV^- centers[54], etc.**

2.4 Defects in silicon carbide

2.4.1 Simplified energy structures of axial VV^0 centers and V_{Si}^- centers in 4H-SiC

In contrast to color centers in diamond, most defects discovered or created in SiC show emission in the near IR ranges. The most studied defects in SiC are V_{Si}^-, VV^0, and $N_CV_{Si}^-$[58-63] color centers. While the ZPLs of V_{Si}^- centers are less than 1000 nm,[62, 63] the latter two give ZPLs ranging from 1000 to 1300 nm.[4, 64] There are some similarities between the latter two defects in SiC and $N_CV_{Si}^-$ centers in diamond:

(A) These defects have different charge states. Both NV^- and NV^0 centers in diamond are reported to give emissions in the visible range. By comparison, $N_CV_{Si}^-$ and VV^0 centers in SiC give emission in the IR range, while it is unclear if the other charge states of them are optically active.

(B) $N_CV_{Si}^-$ and VV^0 centers in SiC have similar defect energy structures as NV^- centers in diamond. They have a triplet ground state, a triplet excited state, and a singlet metastable state. Electron spin of all defects (V_{Si}^-, VV^0, and $N_CV_{Si}^-$ in SiC) could be polarized with an off-resonant optical excitation.

The energy level model is always a helpful picturized method for explaining an atomic defect system's optical, electrical response. To get the full picture of the energy structure, people resort to the ab-initio calculation and the experimental tools, including resonant excitation, microwave sweeping, and electron paramagnetic resonance measurement (EPR). Regarding V_{Si}^-, VV^0, and $N_CV_{Si}^-$ centers in SiC, people always draw experience from the diamond NV^- centers system. Both VV^0 and $N_CV_{Si}^-$ centers in SiC have triplet ground and triplet excited states. There is a non-radiative channel (singlets) that helps the spin polarization (Figure 2.15(a)). V_{Si}^- centers in 4H-SiC have S = 3/2 for the excited and ground states. The $m_s = \pm1/2$ and $m_s = \pm3/2$ sublevels are slightly split by $2D_s = 9$ MHz for ground states and $2D_e = 980$ MHz for excited states[65] (Figure 2.15(b)). Similarly, there is a non-radiative channel-assisted spin polarization into S = 1/2.

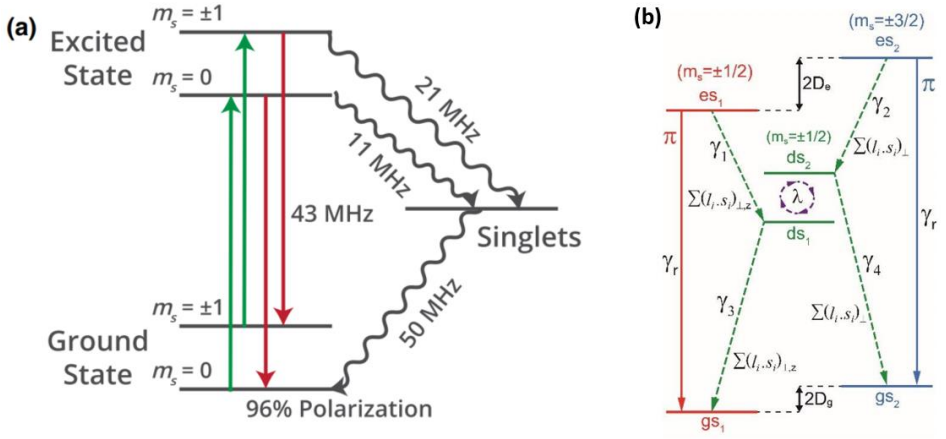

Figure 2.15: Simplified electronic fine structure for (a) axial VV^0[61] and (b) V_{Si}^- (V1)[65] defects in SiC. (a) Reproduced with permission [61]. Copyright 2017, American Physical Society. (b) Reproduced under the terms of a creative commons CC-BY international license [65]. Copyright 2019, The Authors, published by Springer Nature.

The picture shown in Figure 2.15 facilitates understanding the spin-polarization process in the three systems when exposed to **non-resonant excitation**. **However, it is worth**

mentioning that the degeneracy of the orbital state should be considered when the defects are under resonant excitation. Taking VV^0 centers as an example, they have S = 1 orbital singlet ground state and orbital doublet excited state. In terms of V_{Si}^- centers, one can just consider the spin conserving transition between the ground and excited states shown in Figure 2.15(b), as the extra excited state is too far away (this state is shown as a transition named V1' which is 2.3 nm shorter than the V1 transition).

Figure 2.16 shows the experimentally resolved excited state fine structure of 4H- and 3C-SiC VV^0 centers. **Given the similarity between the VV^0 and $N_CV_{Si}^-$ centers, this energy structure, and its characterization method could also be applied to the SiC $N_CV_{Si}^-$ centers**. Figure 2.16(a) shows the energy structure of both the excited state and the ground state. To resolve the fine structure (shown in Figure 2.16(b)), a constant microwave resonant with the ground state splitting should be applied to avoid spin polarization. Not only the fine structure is resolved, but it is also possible to estimate the strain by considering the two transitions: $|0\rangle$-ground state to $|E_x\rangle$ and $|E_y\rangle$ excited states.

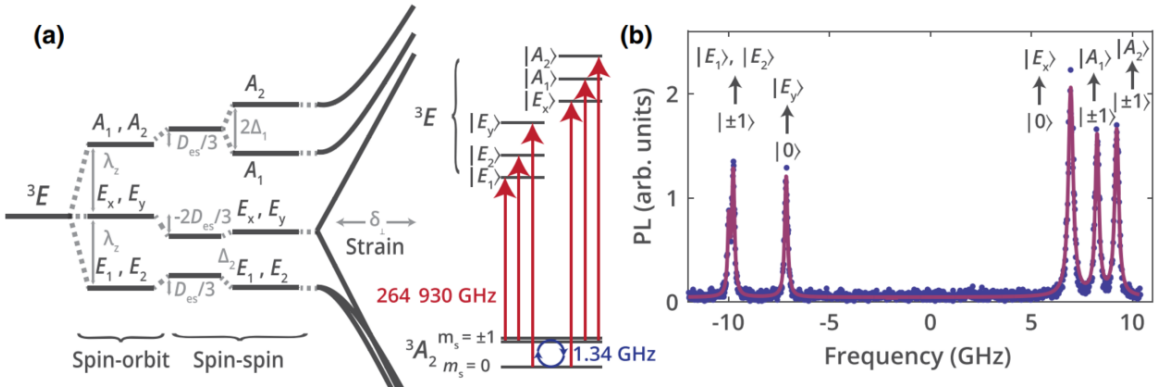

Figure 2.16: Excited-state fine structure of 4H- and 3C-SiC VV^0 centers[61]. (a) Excited-state energy level evolution with decreased perturbations: spin-orbit coupling, spin-spin interaction, and strain. The excited orbital doublets permit 6 spin-conserving transitions at a low strain regime. (b) The resonant excitation resolved 6 transitions from which a transverse strain of 7 GHz is resolved. Reproduced with permission [61]. Copyright 2017, American Physical Society.

2.4.2 Single-photon emission of SiC color centers

SPSs in SiC are ready to be fabricated by carefully choosing the host and the implantation sources (dose, energy, etc.)[2]. SiC is a binary compound material. This gives rise to two different Si and C atoms environments in 4H- and 6H-SiC, namely h and k sites. If the vacancy-vacancy or atom-vacancy replaced both h or k sites, it forms axial centers; otherwise, it

generates basal centers. For one defect type (for example, the VV^0), the number of site-specific defect types depends on the SiC polytype: one in 3C-SiC, four in 4H-SiC, and six in 6H-SiC.[32]

For the VV^0 case, fabrication of a single defect (denoted as PL1 to PL4) has been done via electron and carbon implantation into the commercially available substrate. The saturation counts for PL1 to PL4 are about 27 kcps and the excited state lifetimes are near 14 ns[61, 66]. The emission from a single $N_CV_{Si}^-$ center in 4H-SiC (fabricated via nitrogen ions implantation) has also been reported[25, 66]. Its emission count rate is 27 kcps with a lifetime of 2.7 ns. Both axial and basal centers show polarized emission, with a higher degree of polarization for axial centers[67, 68]. Additionally, single VV centers in 3C-SiC have also been generated. However, the substrate employed is not a commercial but a laboratory-grown one[61].

2.4.3 Room temperature coherent manipulation of VV^0 centers in 4H-SiC

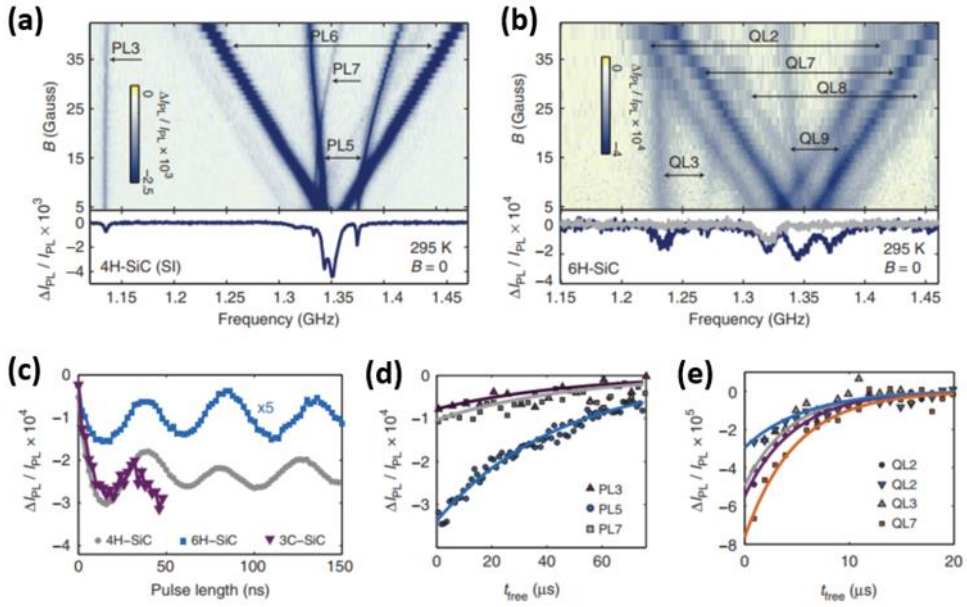

Figure 2.17: Room temperature ensemble spin control[32]. ODMR in (a) 4H-SiC and (b) 6H-SiC with and without external magnetic field. (c) Rabi driving of PL5 centers in 4H-SiC, QL2 centers in 6H-SiC, and VV centers in 3C-SiC. Hanh-echo measurements of ensemble spin in (d) 4H-SiC and (e) 6H-SiC. Reproduced under the terms of a creative commons CC-BY international license [32]. Copyright 2013, The Authors, published by Springer Nature.

The VV^0 centers and $N_CV_{Si}^-$ centers in SiC are not as bright as GaN emitters, which may prevent their use in applications like QKD. Nevertheless, they are suitable for other applications for which the spin degree of freedom is exploited. As shown in Figure 2.17(a) and (b), VV^0 centers ensembles in 4H- and 6H-SiC could be spin-polarized with off-resonant excitation. The coherent manipulation of VV^0[24] and $N_CV_{Si}^-$[66] spin ensembles in 4H-SiC had

been realized at room temperature (Figure 2.17(c)). The reported coherence time (T_2) of VV^0 ensembles in 4H-SiC without dynamic decoupling is hundreds of microseconds (Figure 2.17(d))[24, 32], which are comparable to the diamond NV^- ensembles[69]. This coherence time is almost one order longer than the latter reported value for VV^0 in 3C and 6H-SiC (Figure 2.17(e)). **The progress in SiC $N_CV_{Si}^-$ centers, however, is lagged.** Early studies on SiC $N_CV_{Si}^-$ centers were on the generation of $N_CV_{Si}^-$ ensembles and their low-temperature EPR characterization, which led to the association of distinct $N_CV_{Si}^-$ centers to their zero-field splitting parameters[34, 70-72].

2.4.4 Indistinguishable photon generation from V_{Si}^- centers in 4H-SiC

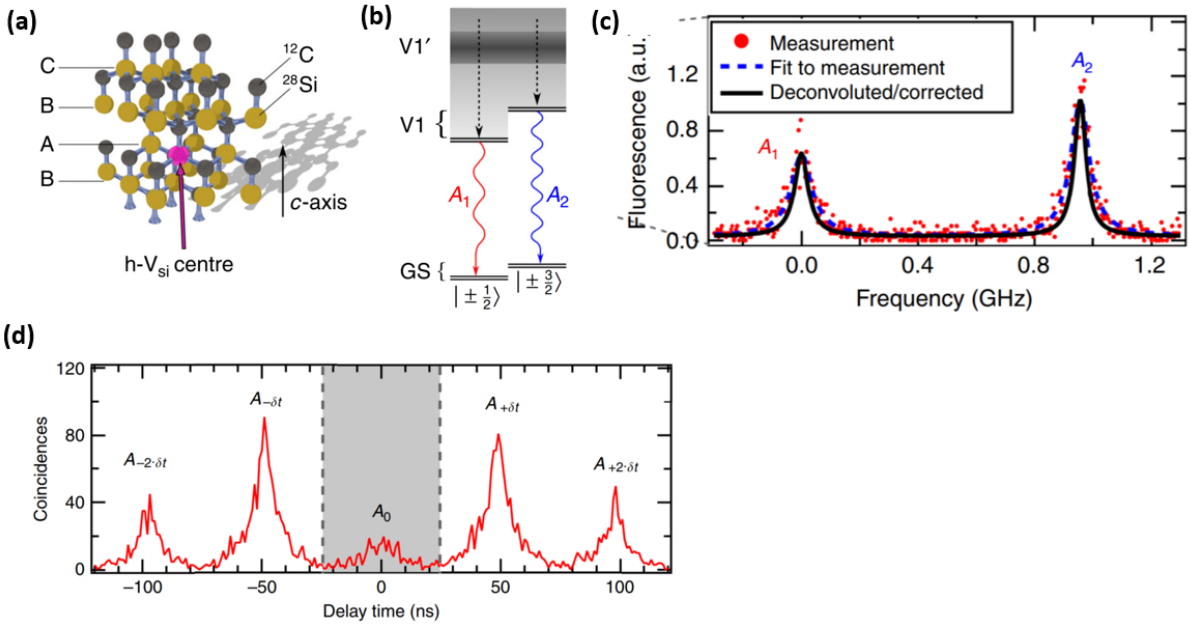

Figure 2.18: Indistinguishable photon generation from V_{Si}^- centers in SiC[12]. (a) Molecular configuration of h-site V_{Si}^- in 4H-SiC. (b) Two spin conserving transitions from the lower excited state to the ground state (A1 for S = 1/2 A2 for S = 3/2). (c) Fabry-Perot cavity resolved emission linewidths. (d) Indistinguishable photon emission from a V_{Si}^- center in SiC. Reproduced under the terms of a creative commons CC-BY international license [12]. Copyright 2020, The Authors, published by Springer Nature.

As a candidate for the spin-photon interface, one prerequisite requirement is to generate indistinguishable emissions. People have demonstrated this with diamond NV^- centers[73] and diamond V_{Si}^- centers[8]. For both systems, people chose two separated emitters to demonstrate this. In the SiC color centers community, Naoya et al. demonstrated the indistinguishability among a train of photons emitted by a V_{Si}^- emitter[12]. The authors chose one emission branch of an h-site emitter (Figure 2-18(a) and (b)). The sample is carefully prepared so that the

emission linewidths are not broadened by strain. The Fabry-cavity resolved linewidths are just 2 times of the lifetime transformed linewidth (Figure 2-18(c)). The HOM experiment is then performed with a train of photons associated with A_1 transition. As shown in Figure 2-18(d), the spectrum associated with the HOM experiment shows a weak peak at zero- time delay. The relative intensity among the five peaks satisfies the well-known ratio of 1 : 2 : 0 : 2 : 1. The estimated HOM interference visibility is about 0.69, which is comparable to the quantum dots results.

2.4.5 Electrical and optical control of single VV^0 center spins in 4H-SiC

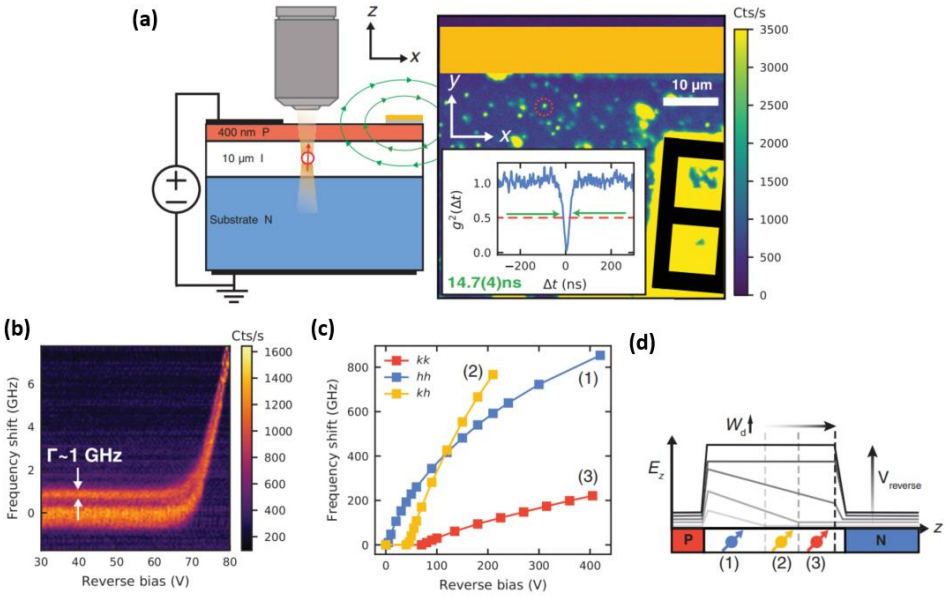

Figure 2.19: Electrical and optical control of VV^0 centers[13]. (a) VV^0 centers reside in a PIN junction. The sample could be controlled with an electric field and microwave. A single VV^0 emitter (marked in a red circle) is isolated by confocal microscopy. (b) Resonant excitation resolved fine energy levels at different reverse biases. (c) Electric field assisted emission wavelength tunning for three emitters (red for kk, blue for hh, and yellow for kh). (d) Three emitters at different depths in the i-layer. Reproduced with permission [13]. Copyright 2019, American Association for the Advancement of Science.

One evident advantage of employing the SiC as a color center host over the diamond counterpart is the feasibility of doping. In return, it is easy to fabricate SiC PIN junctions[13, 74]. This PIN structure enables the manipulation of color centers with electric fields. As shown in Figure 2.19(a), VV^0 centers are generated with electron implantation in the i-layer of 4H-SiC. On top of the p-layer, electrical pads and microwave guides provide electrical and microwave control over the isolated emitters.

It was found that the optical properties of the VV^0 centers could be optimized by applying a reverse bias. Firstly, the transition linewidths get narrower when a reverse bias surpasses a threshold voltage of 70 V (Figure 2.19(b)), starting with 1 GHz and reaching a lifetime limited linewidth (orange lines). On the other hand, the emission wavelength could be tuned up to 1 THz, which is limited by the applicable voltage source (Figure 2.19(c) blue line). Figure 2.19(c) show the wavelength tuning range for three emitters situated at different depth of the i-layer (Figure 2.19(d)). **Benefiting from these two aspects, one can expect to realize indistinguishable emissions from different VV^0 emitters.**

2.5 Contributions of this work in the context of literature

The purpose of this study starts with answering the two pending problems raised during the study of diamond NV^- centers. To give a satisfying answer to these two questions mentioned in Chapter 1 requires the combined efforts of the whole color centers community, including ab-initio calculation, defects generation, defects characterization, single defect manipulation, gate demonstration, and so on. The major contributions of this thesis to the research area are as follows:

(A) The progress in the SiV^- center in diamond demonstrated itself as a promising platform for quantum communication and scalable quantum network applications. However, the SiV^- spins are coupled to phonon bath, limiting the spin coherence time. The SiV^- center should work at 100 mK range to suppress the phonon interaction. To relax this critical temperature limitation, group IV defects with greater Δ_{GS} are preferred. In this regard, we first reported the other charge state of GeV centers and investigated their optical properties. We first observed a single GeV^- center system whose behavior is determined by a typical GeV^- center energy structure plus a dark state. By investigating this system, we found it is possible to suppress the impact of the dark state on the GeV^- center emission by applying weak off-resonant excitation. More importantly, we found that the coherence between the ground and excited state is maintained even with the presence of the dark state, proving that the GeV^- center is a robust spin-photon interface.

(B) The progress of the VV^0 center in SiC is inspiring since it provides new approaches to optimize the optical and spin properties of VV^0 centers thanks to the host. However, their ZPLs are still not falling in the telecom window. The $N_CV_{Si}^-$ centers in SiC exhibit longer emission wavelengths than the VV^0 centers. However, the study of $N_CV_{Si}^-$ centers in SiC was limited to the EPR method. Here, we, on the one hand, demonstrated the single $N_CV_{Si}^-$

emitters generation. On the other hand, we systematically characterized the ground state zero-field splitting parameters associated with each kind of $N_CV_{Si}^-$ center, so did we resolve the hyperfine interaction between electron spins and ^{14}N nuclear spins. Both laid a foundation for further study. Besides, we demonstrated the coherent manipulation of $N_CV_{Si}^-$ centers, showing SiC $N_CV_{Si}^-$ centers a potential spin-photon interface platform.

References

[1] DOWLING J P, MILBURN G J. Quantum technology: the second quantum revolution [J]. Philosophical Transactions of the Royal Society of London Series A: Mathematical, Physical and Engineering Sciences, 2003, 361(1809): 1655-74.

[2] CASTELLETTO S, BORETTI A. Silicon carbide color centers for quantum applications [J]. Journal of Physics: Photonics, 2020, 2(2).

[3] BROWN R H, TWISS R Q. Correlation between Photons in two Coherent Beams of Light [J]. Nature, 1956, 177(4497): 27-9.

[4] HEREMANS F J, YALE C G, AWSCHALOM D D. Control of Spin Defects in Wide-Bandgap Semiconductors for Quantum Technologies [J]. Proceedings of the IEEE, 2016, 104(10): 2009-23.

[5] TOGAN E, CHU Y, TRIFONOV A S, et al. Quantum entanglement between an optical photon and a solid-state spin qubit [J]. Nature, 2010, 466(7307): 730-4.

[6] GRUBER A, DRäBENSTEDT A, TIETZ C, et al. Scanning Confocal Optical Microscopy and Magnetic Resonance on Single Defect Centers [J]. Science, 1997, 276(5321): 2012-4.

[7] BERNIEN H, CHILDRESS L, ROBLEDO L, et al. Two-Photon Quantum Interference from Separate Nitrogen Vacancy Centers in Diamond [J]. Physical Review Letters, 2012, 108(4): 043604.

[8] SIPAHIGIL A, JAHNKE K D, ROGERS L J, et al. Indistinguishable photons from separated silicon-vacancy centers in diamond [J]. Phys Rev Lett, 2014, 113(11): 113602.

[9] BECKER J N, GORLITZ J, AREND C, et al. Ultrafast all-optical coherent control of single silicon vacancy colour centres in diamond [J]. Nat Commun, 2016, 7: 13512.

[10] SIYUSHEV P, METSCH M H, IJAZ A, et al. Optical and microwave control of germanium-vacancy center spins in diamond [J]. Physical Review B, 2017, 96(8): 081201.

[11] EVANS R E, SIPAHIGIL A, SUKACHEV D D, et al. Narrow-Linewidth Homogeneous Optical Emitters in Diamond Nanostructures via Silicon Ion Implantation [J]. Physical Review Applied, 2016, 5(4).

[12] MORIOKA N, BABIN C, NAGY R, et al. Spin-controlled generation of indistinguishable and distinguishable photons from silicon vacancy centres in silicon carbide [J]. Nat Commun, 2020, 11(1): 2516.

[13] ANDERSON C P, BOURASSA A, MIAO K C, et al. Electrical and optical control of single spins integrated in scalable semiconductor devices [J]. Science, 2019, 366(6470): 1225-30.

[14] MIAO K C, BOURASSA A, ANDERSON C P, et al. Electrically driven optical interferometry with spins in silicon carbide [J]. Science Advances, 2019, 5(11): eaay0527.

[15] BERHANE A M, JEONG K Y, BODROG Z, et al. Bright Room-Temperature Single-Photon Emission from Defects in Gallium Nitride [J]. Adv Mater, 2017, 29(12).

[16] WANG J, ZHOU Y, WANG Z, et al. Bright room temperature single photon source at telecom range in cubic silicon carbide [J]. Nat Commun, 2018, 9(1): 4106.

[17] EISAMAN M D, FAN J, MIGDALL A, et al. Invited review article: Single-photon sources and detectors [J]. Rev Sci Instrum, 2011, 82(7): 071101.

[18] HONG C K, OU Z Y, MANDEL L. Measurement of subpicosecond time intervals between two photons by interference [J]. Physical Review Letters, 1987, 59(18): 2044-6.

[19] BATALOV A, JACQUES V, KAISER F, et al. Low temperature studies of the excited-state structure of negatively charged nitrogen-vacancy color centers in diamond [J]. Phys Rev Lett, 2009, 102(19): 195506.

[20] MAZE J R, GALI A, TOGAN E, et al. Properties of nitrogen-vacancy centers in diamond: the group theoretic approach [J]. New Journal of Physics, 2011, 13(2).

[21] BALASUBRAMANIAN G, LAZARIEV A, ARUMUGAM S R, et al. Nitrogen-Vacancy color center in diamond—emerging nanoscale applications in bioimaging and biosensing [J]. Current Opinion in Chemical Biology, 2014, 20: 69-77.

[22] RONDIN L, TETIENNE J P, HINGANT T, et al. Magnetometry with nitrogen-vacancy defects in diamond [J]. Rep Prog Phys, 2014, 77(5): 056503.

[23] GOTTSCHOLL A, KIANINIA M, SOLTAMOV V, et al. Initialization and read-out of intrinsic spin defects in a van der Waals crystal at room temperature [J]. Nat Mater, 2020, 19(5): 540-5.
[24] KOEHL W F, BUCKLEY B B, HEREMANS F J, et al. Room temperature coherent control of defect spin qubits in silicon carbide [J]. Nature, 2011, 479(7371): 84-7.
[25] MU Z, ZARGALEH S A, VON BARDELEBEN H J, et al. Coherent Manipulation with Resonant Excitation and Single Emitter Creation of Nitrogen Vacancy Centers in 4H Silicon Carbide [J]. Nano Lett, 2020.
[26] SOLTAMOV V A, SOLTAMOVA A A, BARANOV P G, et al. Room temperature coherent spin alignment of silicon vacancies in 4 h-and 6 h-sic [J]. Physical review letters, 2012, 108(22): 226402.
[27] ROCCAFORTE F, GIANNAZZO F, RAINERI V. Nanoscale transport properties at silicon carbide interfaces [J]. Journal of Physics D: Applied Physics, 2010, 43(22).
[28] TESFAYE A. SiC Semiconductor Devices Technology, Modeling, and Simulation [J]. PhD dissertation, 2004.
[29] WORT C J H, BALMER R S. Diamond as an electronic material [J]. Materials Today, 2008, 11(1-2): 22-8.
[30] BI W W, KUO H H, KU P, et al. Handbook of GaN semiconductor materials and devices [M]. CRC Press, 2017.
[31] PHAM L M, BAR-GILL N, LE SAGE D, et al. Enhanced metrology using preferential orientation of nitrogen-vacancy centers in diamond [J]. Physical Review B, 2012, 86(12): 121202.
[32] FALK A L, BUCKLEY B B, CALUSINE G, et al. Polytype control of spin qubits in silicon carbide [J]. Nat Commun, 2013, 4: 1819.
[33] JANZéN E, GALI A, CARLSSON P, et al. The silicon vacancy in SiC [J]. Physica B: Condensed Matter, 2009, 404(22): 4354-8.
[34] CSóRé A, VON BARDELEBEN H J, CANTIN J L, et al. Characterization and formation of NV centers in 3C, 4H, and 6H SiC: An ab initio study [J]. Physical Review B, 2017, 96(8).
[35] IVADY V, DAVIDSSON J, DELEGAN N, et al. Stabilization of point-defect spin qubits by quantum wells [J]. Nat Commun, 2019, 10(1): 5607.
[36] BURKARD G. Diamond Spins Shining Bright [J]. Physics, 2014, 7.
[37] TRUSHEIM M E, WAN N H, CHEN K C, et al. Lead-related quantum emitters in diamond [J]. Physical Review B, 2019, 99(7).
[38] THIERING G, GALI A. Ab Initio Magneto-Optical Spectrum of Group-IV Vacancy Color Centers in Diamond [J]. Physical Review X, 2018, 8(2).
[39] CLARK C D, KANDA H, KIFLAWI I I, et al. Silicon defects in diamond [J]. Phys Rev B Condens Matter, 1995, 51(23): 16681-8.
[40] DEBROUX R, MICHAELS C P, PURSER C M, et al. Quantum control of the tin-vacancy spin qubit in diamond [J]. arXiv preprint arXiv:210600723, 2021.
[41] PINGAULT B, BECKER J N, SCHULTE C H, et al. All-optical formation of coherent dark states of silicon-vacancy spins in diamond [J]. Phys Rev Lett, 2014, 113(26): 263601.
[42] BRADAC C, GAO W, FORNERIS J, et al. Quantum nanophotonics with group IV defects in diamond [J]. Nat Commun, 2019, 10(1): 5625.
[43] SIYUSHEV P, METSCH M H, IJAZ A, et al. Optical and microwave control of germanium-vacancy center spins in diamond [J]. Physical Review B, 2017, 96(8).
[44] TRUSHEIM M E, PINGAULT B, WAN N H, et al. Transform-Limited Photons From a Coherent Tin-Vacancy Spin in Diamond [J]. Phys Rev Lett, 2020, 124(2): 023602.
[45] MULLER T, HEPP C, PINGAULT B, et al. Optical signatures of silicon-vacancy spins in diamond [J]. Nat Commun, 2014, 5: 3328.
[46] ROGERS L J, JAHNKE K D, METSCH M H, et al. All-optical initialization, readout, and coherent preparation of single silicon-vacancy spins in diamond [J]. Phys Rev Lett, 2014, 113(26): 263602.
[47] ROGERS L J, JAHNKE K D, TERAJI T, et al. Multiple intrinsically identical single-photon emitters in the solid state [J]. Nat Commun, 2014, 5: 4739.
[48] PINGAULT B, JARAUSCH D D, HEPP C, et al. Coherent control of the silicon-vacancy spin in diamond [J]. Nat Commun, 2017, 8: 15579.

[49] BECKER J N, PINGAULT B, GROSS D, et al. All-Optical Control of the Silicon-Vacancy Spin in Diamond at Millikelvin Temperatures [J]. Phys Rev Lett, 2018, 120(5): 053603.
[50] SUKACHEV D D, SIPAHIGIL A, NGUYEN C T, et al. Silicon-Vacancy Spin Qubit in Diamond: A Quantum Memory Exceeding 10 ms with Single-Shot State Readout [J]. Phys Rev Lett, 2017, 119(22): 223602.
[51] FARAON A, BARCLAY P E, SANTORI C, et al. Resonant enhancement of the zero-phonon emission from a colour centre in a diamond cavity [J]. Nature Photonics, 2011, 5(5): 301-5.
[52] EVANS R E, BHASKAR M K, SUKACHEV D D, et al. Photon-mediated interactions between quantum emitters in a diamond nanocavity [J]. Science, 2018, 362(6415): 662-5.
[53] RIEDRICH-MOLLER J, KIPFSTUHL L, HEPP C, et al. One- and two-dimensional photonic crystal microcavities in single crystal diamond [J]. Nat Nanotechnol, 2011, 7(1): 69-74.
[54] SIPAHIGIL A, EVANS R E, SUKACHEV D D, et al. An integrated diamond nanophotonics platform for quantum-optical networks [J]. Science, 2016, 354(6314): 847-50.
[55] CHU Y, DE LEON N P, SHIELDS B J, et al. Coherent optical transitions in implanted nitrogen vacancy centers [J]. Nano Lett, 2014, 14(4): 1982-6.
[56] FARAON A, SANTORI C, HUANG Z, et al. Coupling of nitrogen-vacancy centers to photonic crystal cavities in monocrystalline diamond [J]. Phys Rev Lett, 2012, 109(3): 033604.
[57] BHASKAR M K, SUKACHEV D D, SIPAHIGIL A, et al. Quantum Nonlinear Optics with a Germanium-Vacancy Color Center in a Nanoscale Diamond Waveguide [J]. Phys Rev Lett, 2017, 118(22): 223603.
[58] CASTELLETTO S, JOHNSON B C, IVADY V, et al. A silicon carbide room-temperature single-photon source-si [J]. Nat Mater, 2014, 13(2): 151-6.
[59] CHRISTLE D J, FALK A L, ANDRICH P, et al. Isolated electron spins in silicon carbide with millisecond coherence times [J]. Nat Mater, 2015, 14(2): 160-3.
[60] VON BARDELEBEN H J, CANTIN J L, RAULS E, et al. Identification and magneto-optical properties of the NV center in4H−SiC [J]. Physical Review B, 2015, 92(6).
[61] CHRISTLE D J, KLIMOV P V, DE LAS CASAS C F, et al. Isolated Spin Qubits in SiC with a High-Fidelity Infrared Spin-to-Photon Interface [J]. Physical Review X, 2017, 7(2).
[62] SINGH H, ANISIMOV A N, NAGALYUK S S, et al. Experimental characterization of spin-$\frac{3}{2}$ silicon vacancy centers in $6H$-SiC [J]. Physical Review B, 2020, 101(13): 134110.
[63] NAGY R, NIETHAMMER M, WIDMANN M, et al. High-fidelity spin and optical control of single silicon-vacancy centres in silicon carbide [J]. Nature Communications, 2019, 10(1): 1954.
[64] VON BARDELEBEN H J, CANTIN J L, CSóRé A, et al. NV centers in3C,4H, and6Hsilicon carbide: A variable platform for solid-state qubits and nanosensors [J]. Physical Review B, 2016, 94(12).
[65] NAGY R, NIETHAMMER M, WIDMANN M, et al. High-fidelity spin and optical control of single silicon-vacancy centres in silicon carbide [J]. Nat Commun, 2019, 10(1): 1954.
[66] WANG J F, YAN F F, LI Q, et al. Coherent Control of Nitrogen-Vacancy Center Spins in Silicon Carbide at Room Temperature [J]. Phys Rev Lett, 2020, 124(22): 223601.
[67] WANG J-F, LIU Z-H, YAN F-F, et al. Experimental Optical Properties of Single Nitrogen Vacancy Centers in Silicon Carbide at Room Temperature [J]. ACS Photonics, 2020, 7(7): 1611-6.
[68] FALK A L, KLIMOV P V, BUCKLEY B B, et al. Electrically and Mechanically Tunable Electron Spins in Silicon Carbide Color Centers [J]. Physical Review Letters, 2014, 112(18): 187601.
[69] STANWIX P L, PHAM L M, MAZE J R, et al. Coherence of nitrogen-vacancy electronic spin ensembles in diamond [J]. Physical Review B, 2010, 82(20): 201201.
[70] ZARGALEH S A, HAMEAU S, EBLE B, et al. Nitrogen vacancy center in cubic silicon carbide: A promising qubit in the 1.5μm spectral range for photonic quantum networks [J]. Physical Review B, 2018, 98(16).
[71] ZARGALEH S A, VON BARDELEBEN H J, CANTIN J L, et al. Electron paramagnetic resonance tagged high-resolution excitation spectroscopy of NV-centers in 4H-SiC [J]. Physical Review B, 2018, 98(21).

[72] KHAZEN K, VON BARDELEBEN H J, ZARGALEH S A, et al. High-resolution resonant excitation of NV centers in 6H−SiC : A matrix for quantum technology applications [J]. Physical Review B, 2019, 100(20).
[73] BERNIEN H, CHILDRESS L, ROBLEDO L, et al. Two-photon quantum interference from separate nitrogen vacancy centers in diamond [J]. Phys Rev Lett, 2012, 108(4): 043604.
[74] LOHRMANN A, IWAMOTO N, BODROG Z, et al. Single-photon emitting diode in silicon carbide [J]. Nat Commun, 2015, 6: 7783.

Chapter III Optical Gating of Resonance Fluorescence from a Single Germanium Vacancy Color Center in Diamond

The application of color centers in quantum networks demands the coherent excitation of quantum emitters. Nevertheless, many solid-state systems could enter in a dark state which inhibits the emission. In this chapter, I show our observation of the dark state in the diamond GeV^- center system upon resonant excitation. I present that the resonance fluorescence of the single GeV^- center could be recovered and amplified by employing an additional gating laser. With this gating laser, the GeV^- centers exhibit stable resonance fluorescence, proving diamond GeV^- centers as reliable building blocks for quantum networks applications. I further present the investigation and simulation of the systems' dynamical behavior upon pulsed laser excitation [1].

3.1 Introduction

The coherent control and manipulation of "Atomic-like" systems are of great importance for future quantum network applications[2, 3]. Recently, the group IV split vacancy centers like SiV^- [4] or the GeV^-[5-10] have attracted much attention since they have an inversion symmetry[11]. Therefore the optical transitions of these centers are not sensitive to the electric-field fluctuation, promising narrow emission linewidths and indistinguishable emissions of separated emitters[12]. Moreover, compared to diamond NV^- centers, these systems have a high Deby-Waller factor[6, 13], i.e., a large concentration of photons is emitted coherently. This makes the resonance fluorescence of group IV centers appealing for quantum applications including quantum communication[14], quantum teleportation[15], and entanglement swapping[16].

Unfortunately, these group IV split vacancy centers might undergo a nonradiative transition to a dark state under resonant excitation, leading to a quenched resonance fluorescence (RF). Regarding the diamond NV^- centers[17], similar behavior has been reported and the underlying mechanism is attributed to a charge state conversion from the negative to neutral state[18, 19]. This detrimental process leads to diminished photon emission under resonant excitation, hindering the applications like single-shot spin readout[20, 21], and quantum network[22]. In this Chapter, I report the quenched RF behavior of the GeV^- centers. Fortunately, the quenched RF could be switched on by using a week 532 nm nonresonant laser but not introducing any additional spectral diffusion on the emitter. This nonresonant laser gate controlled the RF of the emitter, which could be modeled by a three-level model including a ground state, an excited state, and a dark state.

3.2 Experimental settings

3.2.1 Sample preparation

The GeV^- center is generated by Ge^+ ions implantation into an electronic grade diamond (Type IIa). The pristine host was first washed in hot Piranha acid for one hour (150℃ 3 : 1 = H_2SO_2 : H_2O_2). After cleaning, the diamond substrate was coated with a 10 nm Gold/Palladium film by sputter coating so as to mitigate charges during the following fabrications. The solid immersion lens (SILs) are developed by using Ga^+ ions beam milling (30 kV, 7 nA). The resulted SILs have approximately a diameter of 5 μm (A representative SIL is shown in Figure 3.1(c)). The Au/Pd film was then etched out with Aqua Regia (100 ℃ 3 : 1 = HCl : HNO_3) to allow the

following high energy Ge^{4+} ion implantation (7 MeV, fluence of 5 $\times 10^{10}$ cm^{-2}, current of 1.5 nA). The diamond host was again cleaned in hot Piranha Acid. The sample is subsequently annealed in high vacuum (2 $\times$ 10^{-6} mbar) at 900℃ for 2 hours. After annealing, there are approximately 3 to 5 GeV^- centers per SIL.

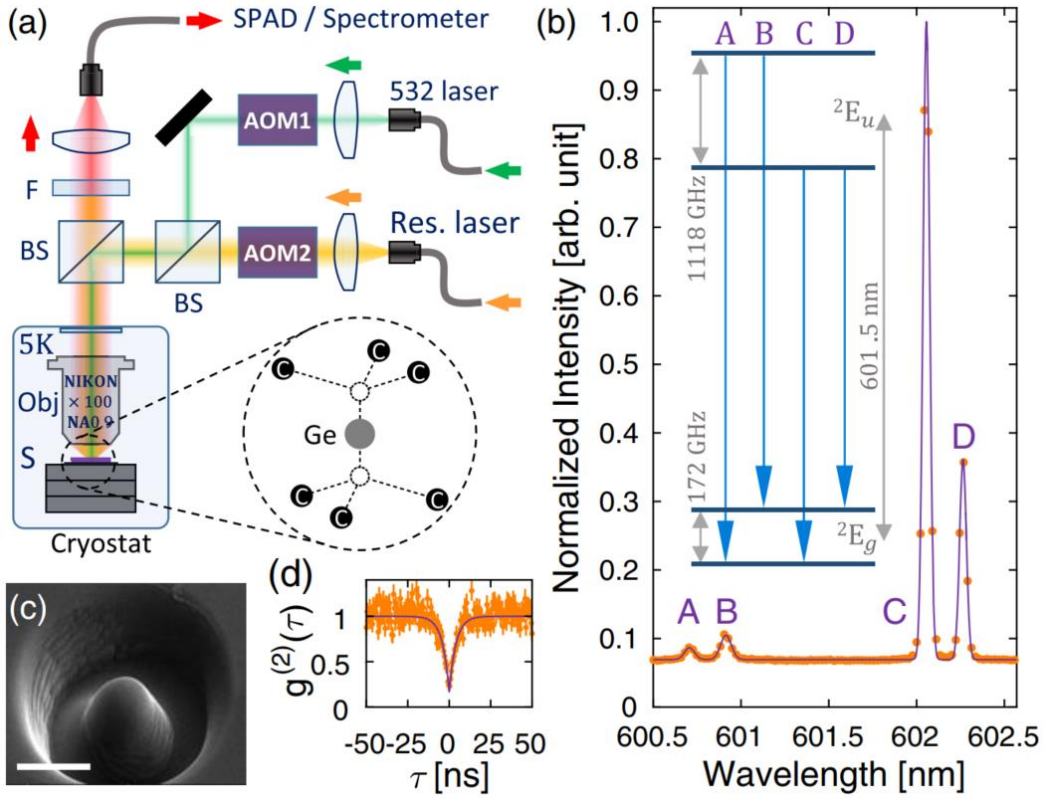

Figure 3.1[1]: (a) Experimental setup. BS, 50:50 nonpolarizing beam splitter; AOM, acousto-optic modulator; S, sample; Obj, objective; F, spectral filter; SPAD, single-photon avalanche detector. Inset, schematic of a GeV^- center. (b) A representative PL spectrum of GeV^- color center at 5 K, which is excited nonresonantly by a 532 nm laser (Power of 0.4 mW ($0.06P_1$)). The integration time is 5 s. The orange dots are the raw data while the purple line refers to the fitting with four Gaussian functions. The Gaussian peaks are labeled as A, B, C, and D. Inset, the energy structure of the GeV^- center associated with the four transitions. The GS and ES splitting are indicated according to the fitting results. (c) Scanning electron microscope imaging of the investigated SIL. The scale bar is 3 μm. (d) The $g^{(2)}(\tau)$ of the GeV^- center under nonresonant excitation (532 nm, ∼1 mW) at room temperature. An antibunching dip of $g^{(2)}(0) = 0.17 \pm 0.03$ is obtained with a two-level model fitting. Reproduced with permission [1]. Copyright 2019, American Physical Society.

3.2.2 Experimental setup

In this study, a home-built confocal microscope was used to perform all the optical measurements (Figure 3.1(a)). The sample is loaded into a closed-cycle helium-flow Montana

Cryostation at 5 K. The sample position is controlled with a low-temperature XYZ piezo stepper stage which allows us to move the desired SIL to the focal point of the objective (NA = 0.9). A 532 nm laser is used for the nonresonant excitation of the GeV^- center, and gating of RF after passing through an acousto-optic modulator (AOM). For the photoluminescence excitation experiment, a tunable continuous wave (CW) laser is employed to address the GeV^- center resonantly. The collection arm of the confocal microscope is equipped with a series of filters which promised different measurement purposes: a 600 ± 7 nm bandpass filter is used in PL spectrum characterization (only ZPL is detected) while a 650 ± 20 nm bandpass filter is employed in the PLE and gating experiment (only PSB is collected).

3.2.3 Single GeV^- emitter identification

The GeV^- center exhibit the molecular configuration shown in Figure 3.1 (a), in which two vacancies replaced two bonded carbon sites while the Ge atom is located at the center of these two vacancies. Due to this molecular configuration, the GeV^- center has a D_{3d} symmetry. Both the ground state (^2E_g) and excited state (^2E_u) of the GeV^- center are orbital doublets that are split with different splitting energy (Δ_{GS} and Δ_{ES}) due to the strong spin-orbit coupling[23], giving a typical four-line structure in the ZPL emission spectrum (Figure 3.1(b)). Each orbital level includes two degenerated spin sublevels whose degeneracy could be lifted by applying an external magnetic field. A single photon emitter is firstly identified with the nonresonant excitation for the following investigation (Figure 3.1(d)).

3.3 Optical gating of resonance fluorescence with a nonresonant laser

The gating effect is observed for both the transitions C and D. As compared in Figure 3.2(a), the PLE spectra for both transitions can only be detected when the gating laser is on, from which the linewidth of the emissions could be determined. Compared to the gating-off case, the emission is enhanced by about 500 times when the gating laser is on (Figure 3.2B). However, the gating laser power is just $\sim 10^{-4}$ of non-resonant saturation power $P_1 = 6.8 \pm 0.1$ mW (see APPENDIX Figure A1(b)). There is no detectable emission if the resonant laser is turning off while keeping the gating laser is on (Figure 3.2b right panel). Hence, the main role of the gating laser is to switch ON and OFF the RF of the emitter. Besides the 532 nm laser, the 405 nm laser could play the same gating role (Figure 3.2(a) purple curve).

To realize all-optical manipulation of the orbital states of defects, the states are often prepared into an orbital level by optical pumping. As presented in Chapter 2, the ground state

orbital relaxation time ($T_1^{orbital}$) is about 20 ns[24]. However, this lifetime is orders of magnitude faster than the gating dynamics investigated here. Hence, our observations could not be explained by the possible optical pumping between two ground states. Instead, a long-live dark state to account for the observation is introduced here. As shown in Figure 3.2(c), there is a bunching plateau range from μs to ms range in the second-order correlation function measurement. The presence of the bunching plateau, along with the stochastic jumping of the RF shown in the inset of Figure 3.2(c) [25, 26], both evidence suggested the presence of a dark state.

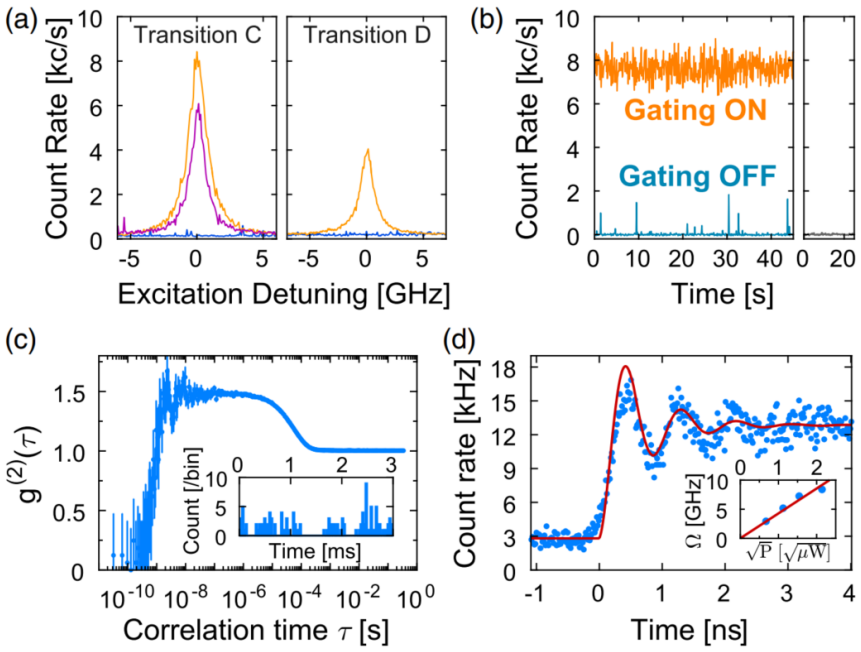

Figure 3.2[1]: Photoluminescence excitation spectra of transitions C (left) and D (right) when the gating laser is off (blue) and on (orange). The orange line refers to a gating laser at 532 nm while the purple at 405 nm. These curves are detuned from 602.2903 and 602.4828 nm for C and D, respectively. (b) Time-resolved RF intensity of C-transition when gating off (blue) and on (orange). Right, PL intensity under merely gating laser excitation. The dark count has been subtracted. The binsize is 100 ms. (c) $g^{(2)}(\tau)$ of the GeV^- center when C-transition is resonantly pumped. $g^{(2)}(0) = 0.07$. The oscillating signal near 5 ns is related to Rabi oscillation. Inset, stochastic emission of the transition C under resonant excitation. The binsize is 33 μs. (d) Rabi oscillations of C-transition under pulsed resonant excitation. The red curve is the fitting with a two-level mode (details in APPENDIX A). Inset, the Rabi frequency verse the square root of the resonant power along with a linear fit (red line). The resonant power in (a) and (b) is 200 nW, 300 nW in (c), and 2.4 μW in (d). The gating power is set to 1.2 μW (1.8×10^{-4} P_1) for all. Reproduced with permission [1]. Copyright 2019, American Physical Society.

Interestingly, regardless of the dark state, it is still possible to coherently control the ground and excited states, as demonstrated by the Rabi experiment. From the Rabi oscillations of the transitions C in Figure 3.2(d), the extracted dephasing time is about 366 ± 20 ps. This implies

that the coherence between the ground and excited states could be maintained for the hundreds ps range. During the experiment, multiple peaks around the transition C are observed [see APPENDIX Figure A5(a)] which may be associated with transitions of nearby GeV^- centers. By contrast, there is a single peak near transition D. To simplify the following investigation, I focused on transition D for the photo-dynamics study.

3.4 Photodynamics of the GeV^- center

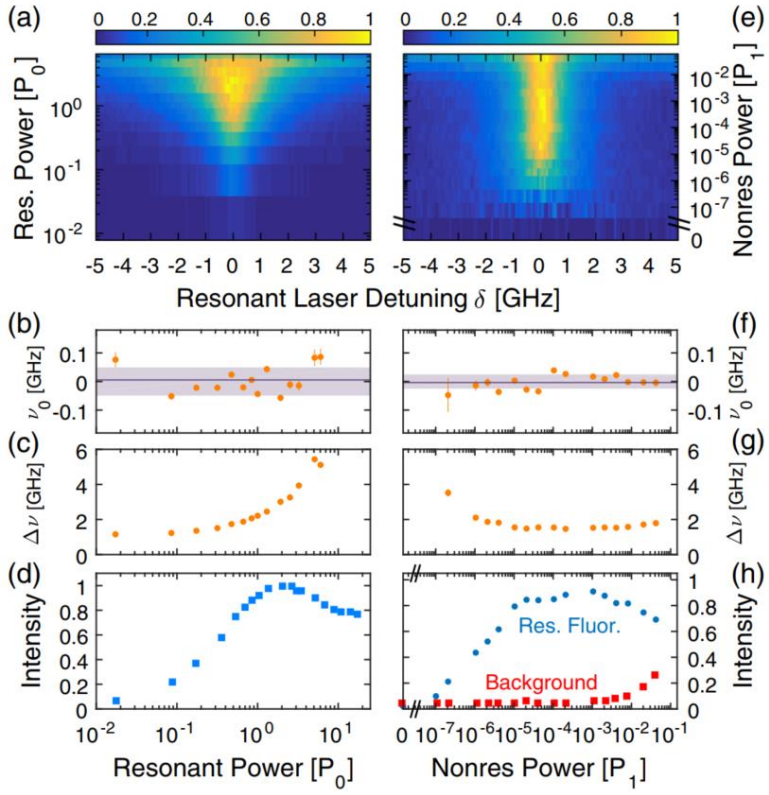

Figure 3.3[1]: 2-dimensional mapping of the normalized PLE spectra by tunning either the resonant excitation power (a) or the gating laser power (e). The normalization count for is 10 kcnt/s (a) and 4 kcnt/s (e). Gating power in (a), $7 \times 10^{-5} P_1$; resonant power in (e), 0.35 P_0. (b) and (f) are the center emission frequency ν_0 of each line in (a) and (e), extracted from Lorentzian fitting. The shadow area indicated the standard deviation of ν_0, giving (b) $\sigma \sim 50$ MHz, and (f) $\sigma \sim 25$ MHz. (c) and (g) are the Lorentzian linewidth $\Delta\nu$ of each spectrum in (a) and (e). (d) Resonant-power dependence of RF, measured by setting the resonant laser at zero detuning. (h) Gating-power dependence of RF (blue), evaluated by subtracting the background from the maximum count rate of each line in (e). Background count rate (red) is measured at a far detuning of ~10 GHz. Reproduced with permission [1]. Copyright 2019, American Physical Society.

To investigate the underlying photodynamics, the study employed both the resonant (Figure 3.3(a)) and gating (Figure 3.3(e)) power-dependent RF. Each PLE spectrum is fit with a Lorentzian function, from which the center transition frequency, the linewidth, and the counts

are determined. These extracted data are compared and analyzed in Figure 3.3. In detail, the center transition frequency remains the same at different resonant or gating laser power (Figure 3.3 (b) and (f)), which is granted by the inversion symmetry of the GeV^- center. As expected, the emission linewidth exhibits a power broadening (Figure 3.3(c)). However, the RF intensity under varied resonant power excitation exhibits an abnormal power dependence. There is a RF intensity drop at $\sim 3P_0$ (Figure 3.3(d)), where $P_0 = 1.15 \pm 0.39$ μW is the resonant saturation power and is obtained by using a pulse measurement scheme [details in APPENDIX A]. The observation of RF drop consolidated the presence of the dark state and suggests the opposite role of the resonant laser as compared to the gating laser. The resonant laser is likely to shelve the population into a dark state. Regarding the gating laser dependence, the PLE spectrum begins to recover as the gating power increases and finally stabilizes at $\sim 10^{-5}P_1$ (Figure 3.3(e)). Even though this evolution, the C-transition exhibit the same transition energy (Figure 3.3(f)) and a constant excitation linewidth (Figure 3.3(g)). Again, these superior optical properties are closely related to the D_{3d} symmetry of the center[24], which is in stark contrast to the NV^- centers under non-resonant excitation[27]. Regarding the broad emission linewidth at a low gating power range ($<10^{-6}P_1$), it is attribute to the detuning-dependent shelving efficiency of the system. Considering a constant deshelving rate, the shelving is stronger when the excitation wavelength is less detuned. As a result, there is a flatterning of the PLE spectrum, reslting in a broader linewidth [see APPENDIX A] when the gating power is in the weak range. Similar linewidth broadening is observed in SiV^- center system at millikelvin working temperature, for which the spin pumping is responsible for the shelving[28]. While the gating laser power increases, the gating laser-based dynamical rates are increased and would finally dominate the population dynamics over the resonant laser, thus resulting in a constant linewidth. When the gating laser power surpasses $10^{-3}P_1$, the intensity of the RF begins to reduce along with an increase of the PLE background due to the non-resonant excitation (Figure 3.3(h)). At this phase, there is a competition between the non-resonant and resonant excitations.

3.5 Gating and shelving dynamics - A phenomenological picture

During the experiment, the resonant laser-induced shelving effect could be demonstrated by turning ON and OFF of the resonant laser while keeping the nonresonant always on. As shown in Figure 3.4(a), there is an immediate RF intensity decay after the resonant laser is ON, which revealed the shelving process. The instant peak intensity reflects the excited state population before being influenced by the shelving process. After a while of competing between the

shelving and deshelving process, the whole system enters into an equilibrium state and shows a plateau intensity. Based on these observations, a three-level model including a ground state (G), an excited state (E), and a dark state (D) is employed to simulate the photodynamics, as shown in Figure 3.4(b). In detail, the G population could be resonantly promoted to the E with a coupling strength of Ω. The E population could decay radiatively to the G via spontaneous decay process (a rate of Γ_{sp}) or could be shelved into the D via a nonradiative channel (a rate of k_{ED}). The gating laser would speed up the population exchange between G and D at rates of k_{DG} and k_{GD}. Employing this semiclassical picture, the time evolution of the system is described by the following master equation

$$\frac{d}{dt}\begin{pmatrix}\rho_G\\ \rho_E\\ \rho_{GE}\\ \rho_{EG}\\ \rho_D\end{pmatrix}=\begin{pmatrix}-k_{GD} & \Gamma_{sp} & i\Omega/2 & -i\Omega/2 & k_{DG}\\ 0 & -\Gamma_{sp}-k_{ED} & -i\Omega/2 & i\Omega/2 & \rho_G\\ i\Omega/2 & -i\Omega/2 & -1/T_2 & 0 & 0\\ -i\Omega/2 & i\Omega/2 & 0 & -1/T_2 & 0\\ k_{GD} & k_{ED} & 0 & 0 & -k_{DG}\end{pmatrix}\begin{pmatrix}\rho_G\\ \rho_E\\ \rho_{GE}\\ \rho_{EG}\\ \rho_D\end{pmatrix} \tag{3.1}$$

where ρ_G, ρ_E, and ρ_D are the time-dependent population in G, E, and D states. ρ_{GE} and ρ_{EG} are the coherence between G and E, Ω is the resonant Rabi frequency, Γ_{sp} is the spontaneous decay rate, and T_2 is the coherence time of the excited state. It is worth mentioning that Equation (3-1) has already incorporated the stimulated emission, which should play a nontrivial role in the population dynamics of the investigated system. From the steady-state solution of Equation (3-1), the excitation linewidth is derived as equation (3-2).

$$\Delta\nu=\frac{1}{\pi T_2}\sqrt{1+\frac{\Omega^2 T_2}{2(\Gamma_{sp}+k_{ED})}\left(1+\frac{k_{ED}+k_{DG}}{k_{DG}+k_{GD}}\right)} \tag{3.2}$$

in the unit of linear frequency. The coherence time T_2 could be estimated by assuming that the asymptotic linewidth at $0P_0$ in Figure 3.3(c) equals the linewidth estimated by using Equation (3-2) with Ω = 0. From Figure 3.3(c), a 1 GHz linewidth is determined and a coherence of (T_2) 316 ± 20 ps is estimated. This figure agrees with the coherence time estimated from the Rabi experiment (Figure 3.2(d)). In practice, the detected RF fluorescence could be estimated as (3-3)

$$I_{PL}(t)=\eta\Gamma_{sp}\rho_E(t) \tag{3.3}$$

where $\eta = 9\times10^{-5}$ is the overall efficiency which takes both the quantum yield of GeV^- center [29] and the system detection efficiency into consideration [details in APPENDIX A].

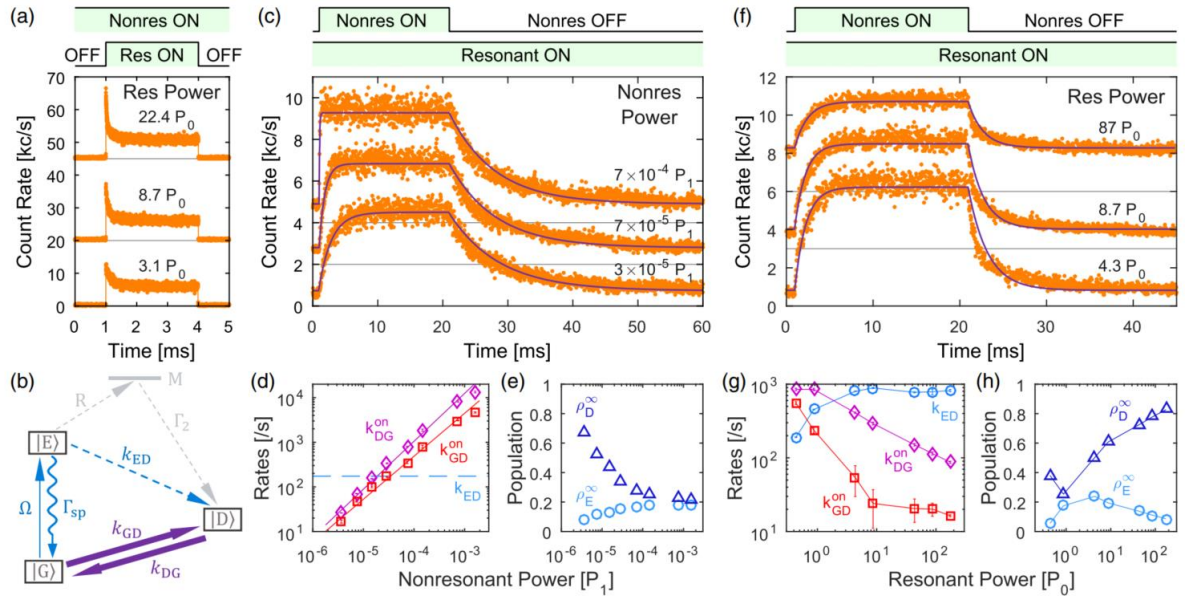

Figure 3.4: Gating and shelving dynamics[1]. (a) Time-resolved PL by modulating the resonant beam while keeping a constant non-resonant power of $7 \times 10^{-7} P_1$. (b) Physical model. G, E, D, and M: ground, excited, dark, and metastable state; k_{GD}, k_{DG}, and k_{ED}: population transfer rates from G to D, D to G, and E to D. Ω: resonant Rabi frequency; $\Gamma_{sp} = 1/T_1 = 280$ MHz: spontaneous decay rate, determined by lifetime measurement [APPENDIX Figure A1]. Gray arrows indicate the possible physical processes underlying k_{ED}. (c) and (f) is the time-resolved PL by modulating the gating laser power while (c) keeping a constant resonant power ($0.9P_0$) or (f) a constant gating power ($7 \times 10^{-5} P_1$). Black curves are the fittings by employing equation (3-3). (d) and (g) are the dynamical rates extracted from the fittings in (c) and (f), respectively. Dashed blue horizontal lines in (d) depict k_{ED}, representing its trivial non-resonant-power dependence in this experiment. Solid straight lines in (d) are the fittings with $k_{GD}^{on} = 3.5 \times 10^6 \times P^{0.96}$ (red) and $k_{DG}^{on} = 2.1 \times 10^7 \times P^{1.07}$ (purple), where P denotes the gating power in the unit of P_1. (e) and (h) are the on-period steady-state population of the dark state ρ_D^∞ and two-level system ρ_E^∞, evaluated by using the rates in (d) and (g), respectively. In (a), (c), and (f), raw data (orange dots) are vertically shifted for clarity, with the zero-intensity level indicated by the gray horizontal lines. Top panel: modulation protocol. Reproduced with permission [1]. Copyright 2019, American Physical Society.

To obtain the dynamical gating and shelving rates, I perform another time-resolved experiment where the gating laser is modulated while the resonant laser is constantly turning on. In detail, the PL intensity shown in Figure 3.4(c) exhibits the same modulation pattern as the gating laser and shows a gating-power-dependent rising edge. According to the results in the last section, the gating laser would have little impact on k_{ED}. Hence, this rate is treated as a constant and is determined by a global fitting. It is found that the k_{GD} and k_{DG} rates increase linearly over the gating power (Figure 3.4(d)). This linear dependence suggests the shelving and deshelving process induced by the gating laser is a single photon process. As the gating power increases,

the population of the ground and excited states in the steady-state increases but also exhibits a saturation behavior (Figure 3.4(e)).

By comparison, the main impact of the resonant excitation at higher excitation powers is to accelerate the shelving process (k_{ED}), which in return reduced indirectly the k_{GD} and k_{DG} rates (Figure 3.4(g)). Particularly, the k_{ED} presents a saturation behavior that could be explained by considering a two-step shelving model. This two-step model is mediated by a metastable state M (gray arrows in Figure 3.4(b)). The first step describes the pumping (R) process from the excited state to the metastable state and is quantified by the k_{ED}. The second step involves a non-radiative decay from the metastable state to the dark state with a kHz decay rate of Γ_2. Here, while the rate of k_{ED} is resonant power dependent, the rate of Γ_2 is not sensitive to the laser power. The presence of a maximum steady-state population ρ_E^∞ at several P_0 in Figure 3.4(h) implies that there is an optimal resonant power to maximize the RF intensity at a given gating power.

3.6 Discussions and conclusions

In the end, I discuss the possible photophysics of the GeV^- centers by drawing experience from other systems which exhibit a similar behavior including NV^- centers in diamond[18, 29] and InGaAs self-assembled quantum dots (QD)[30, 31]. For these two systems, the dark state is a different charge state of the emitter, neutrally charged NV center[32], and positively charged QD[25]. Hence, it is plausible to associate the dark state to another charge state of the GeV center (e.g. the neutral state)[23]. Among all the three systems, the RF gating could be achieved by using a small amount of gating laser. Regarding the NV centers and QDs, the gating laser produces a local free-charge carrier bath whose presence is in favor of the resonant excitation. Similarly, the GeV^- system might share a similar mechanism. This could be substantiated with the following two observations: (1) both k_{DG} and k_{GD} (Figure 3.4(d)) exhibit a linear power dependence; (2) Both 405 and 532 nm laser provide identical gating efficiency (Figure 3.2(a)). However, these three systems do have some degree of difference regarding the shelving mechanism. In detail, there is no report of the shelving channel for QDs. The charge state conversion in the diamond NV centers involves a two-photon ionization or deionization process, leading to quadratic power dependence of the dynamical rates[18, 19]. By comparison, the two-step shelving of the GeV^- center is mediated by a metastable state along with a nonradiative decay channel. Finally, the rates decrease of both k_{GD} and k_{DG} in Figure 3.4(g) are likely caused by the decreased free charge carrier density. This is because more charge traps in

the resonant laser illuminated area are created when the resonant laser power is stronger [details in APPENDIX A].

In conclusion, the shelving effect of the resonant laser in GeV^- centers and the deshelving effect of the gating laser are revealed. The underlying photodynamics of the shelving and deshelving processes could be quantitatively explained by introducing a dark state, though the nature of this dark state needs further investigation. This RF quenching is also observed in SnV^- system and the RF is also recovered with this technique[33]. Hence, the gating phenomenon is a quite general technique in the color center community [see APPENDIX A]. The stabilized RF with gating laser is important for color center-based quantum information science including the demonstration of spin-photon entanglement[34, 35] and photon interferences[12].

References

[1] CHEN D, MU Z, ZHOU Y, et al. Optical Gating of Resonance Fluorescence from a Single Germanium Vacancy Color Center in Diamond [J]. Phys Rev Lett, 2019, 123(3): 033602.

[2] AHARONOVICH I, NEU E. Diamond nanophotonics [J]. Advanced Optical Materials, 2014, 2(10): 911-28.

[3] ATATüRE M, ENGLUND D, VAMIVAKAS N, et al. Material platforms for spin-based photonic quantum technologies [J]. Nature Reviews Materials, 2018, 3(5): 38-51.

[4] NEU E, STEINMETZ D, RIEDRICH-MöLLER J, et al. Single photon emission from silicon-vacancy colour centres in chemical vapour deposition nano-diamonds on iridium [J]. New Journal of Physics, 2011, 13(2): 025012.

[5] IWASAKI T, ISHIBASHI F, MIYAMOTO Y, et al. Germanium-vacancy single color centers in diamond [J]. Scientific reports, 2015, 5(1): 1-7.

[6] PALYANOV Y N, KUPRIYANOV I N, BORZDOV Y M, et al. Germanium: a new catalyst for diamond synthesis and a new optically active impurity in diamond [J]. Scientific reports, 2015, 5(1): 1-8.

[7] BHASKAR M K, SUKACHEV D D, SIPAHIGIL A, et al. Quantum nonlinear optics with a germanium-vacancy color center in a nanoscale diamond waveguide [J]. Physical review letters, 2017, 118(22): 223603.

[8] HäUßLER S, THIERING G, DIETRICH A, et al. Photoluminescence excitation spectroscopy of SiV− and GeV− color center in diamond [J]. New Journal of Physics, 2017, 19(6): 063036.

[9] BRAY K, REGAN B, TRYCZ A, et al. Single crystal diamond membranes and photonic resonators containing germanium vacancy color centers [J]. ACS Photonics, 2018, 5(12): 4817-22.

[10] SIAMPOUR H, KUMAR S, DAVYDOV V A, et al. On-chip excitation of single germanium vacancies in nanodiamonds embedded in plasmonic waveguides [J]. Light: Science & Applications, 2018, 7(1): 1-9.

[11] HEPP C, MüLLER T, WASELOWSKI V, et al. Electronic structure of the silicon vacancy color center in diamond [J]. Physical Review Letters, 2014, 112(3): 036405.

[12] SIPAHIGIL A, JAHNKE K D, ROGERS L J, et al. Indistinguishable photons from separated silicon-vacancy centers in diamond [J]. Physical review letters, 2014, 113(11): 113602.

[13] NEU E, FISCHER M, GSELL S, et al. Fluorescence and polarization spectroscopy of single silicon vacancy centers in heteroepitaxial nanodiamonds on iridium [J]. Physical Review B, 2011, 84(20): 205211.

[14] DUAN L-M, LUKIN M D, CIRAC J I, et al. Long-distance quantum communication with atomic ensembles and linear optics [J]. Nature, 2001, 414(6862): 413-8.

[15] BOUWMEESTER D, PAN J-W, MATTLE K, et al. Experimental quantum teleportation [J]. Nature, 1997, 390(6660): 575-9.

[16] PAN J-W, BOUWMEESTER D, WEINFURTER H, et al. Experimental entanglement swapping: entangling photons that never interacted [J]. Physical review letters, 1998, 80(18): 3891.

[17] DOHERTY M W, MANSON N B, DELANEY P, et al. The nitrogen-vacancy colour centre in diamond [J]. Physics Reports, 2013, 528(1): 1-45.

[18] WALDHERR G, BECK J, STEINER M, et al. Dark states of single nitrogen-vacancy centers in diamond unraveled by single shot NMR [J]. Physical review letters, 2011, 106(15): 157601.

[19] SIYUSHEV P, PINTO H, VöRöS M, et al. Optically controlled switching of the charge state of a single nitrogen-vacancy center in diamond at cryogenic temperatures [J]. Physical review letters, 2013, 110(16): 167402.

[20] VAMIVAKAS A N, LU C-Y, MATTHIESEN C, et al. Observation of spin-dependent quantum jumps via quantum dot resonance fluorescence [J]. Nature, 2010, 467(7313): 297-300.

[21] SUKACHEV D D, SIPAHIGIL A, NGUYEN C T, et al. Silicon-vacancy spin qubit in diamond: a quantum memory exceeding 10 ms with single-shot state readout [J]. Physical review letters, 2017, 119(22): 223602.

[22] KIMBLE H J. The quantum internet [J]. Nature, 2008, 453(7198): 1023-30.

[23] THIERING G, GALI A. Ab initio magneto-optical spectrum of group-IV vacancy color centers in diamond [J]. Physical Review X, 2018, 8(2): 021063.
[24] SIYUSHEV P, METSCH M H, IJAZ A, et al. Optical and microwave control of germanium-vacancy center spins in diamond [J]. Physical Review B, 2017, 96(8): 081201.
[25] NGUYEN H S, SALLEN G, ABBARCHI M, et al. Photoneutralization and slow capture of carriers in quantum dots probed by resonant excitation spectroscopy [J]. Physical review B, 2013, 87(11): 115305.
[26] DELTEIL A, GAO W-B, FALLAHI P, et al. Observation of quantum jumps of a single quantum dot spin using submicrosecond single-shot optical readout [J]. Physical review letters, 2014, 112(11): 116802.
[27] WOLTERS J, SADZAK N, SCHELL A W, et al. Measurement of the ultrafast spectral diffusion of the optical transition of nitrogen vacancy centers in nano-size diamond using correlation interferometry [J]. Physical review letters, 2013, 110(2): 027401.
[28] BECKER J N, PINGAULT B, GROß D, et al. All-optical control of the silicon-vacancy spin in diamond at millikelvin temperatures [J]. Physical review letters, 2018, 120(5): 053603.
[29] FU K-M, SANTORI C, BARCLAY P, et al. Conversion of neutral nitrogen-vacancy centers to negatively charged nitrogen-vacancy centers through selective oxidation [J]. Applied Physics Letters, 2010, 96(12): 121907.
[30] NGUYEN H-S, SALLEN G, VOISIN C, et al. Optically gated resonant emission of single quantum dots [J]. Physical review letters, 2012, 108(5): 057401.
[31] CHEN D, LANDER G R, KROWPMAN K S, et al. Characterization of the local charge environment of a single quantum dot via resonance fluorescence [J]. Physical Review B, 2016, 93(11): 115307.
[32] ASLAM N, WALDHERR G, NEUMANN P, et al. Photo-induced ionization dynamics of the nitrogen vacancy defect in diamond investigated by single-shot charge state detection [J]. New Journal of Physics, 2013, 15(1): 013064.
[33] GöRLITZ J, HERRMANN D, FUCHS P, et al. Coherence of a charge stabilised tin-vacancy spin in diamond [J]. arXiv preprint arXiv:211005451, 2021.
[34] TOGAN E, CHU Y, TRIFONOV A S, et al. Quantum entanglement between an optical photon and a solid-state spin qubit [J]. Nature, 2010, 466(7307): 730-4.
[35] DE GREVE K, YU L, MCMAHON P L, et al. Quantum-dot spin–photon entanglement via frequency downconversion to telecom wavelength [J]. Nature, 2012, 491(7424): 421-5.

Chapter IV Observation of binary spectral jumps in color centers in diamond

In Chapter III, I report the resonant laser excitation assisted state transition to a dark state in a GeV^- center system. This transition is attributed to the complicated environment that the defects reside in. In this chapter, we report the observation of states conversion in Ge^+ ions implanted diamond sample. The states conversion occurs within two emissive states upon non-resonant excitation. Thanks to the low jumping rates, the emission dynamics is directly monitored. The quadratic power dependence of the conversion rates suggests the quantum jumps are related to a two-photon ionization process. This work provides extra insights into the photodynamics of the spectral jumps on defect-based single-photon emitters hosted in wide-bandgap semiconductors[1].

4.1 Introduction

During the past several decades, color centers in diamond have been extensively investigated from quantum applications[2, 3] including quantum sensing [4, 5], quantum communication[6], and quantum computing[7, 8]. Among these defects, the NV^- center in diamond attracted the most attention[9], based on which the superior optical properties including lifetime limited linewidth emission[10] and indistinguishable photon generation from different emitters[11] have been demonstrated. Nevertheless, NV^- centers exhibit a small Debye-Waller (DW) factor due to strong electron-phonon interaction[12], and their emissions are sensitive to the fluctuating electrical field[13, 14]. Both drawbacks would have a negative impact on the application of NV^- centers into quantum networks. By contrast, the negatively charged group IV split-vacancy centers in diamond (silicon-vacancy (SiV^-)[15] and germanium-vacancy (GeV^-)[16, 17] centers) exhibit superior optical properties[18-22] and long spin coherence time[23]. These emitters have high ZPL ratios and their emissions are less sensitive to the electrical field fluctuation thanks to the inversion symmetry of the defects' molecular structures[24, 25]. Unlike the NV^- centers in diamond, indistinguishable photon emission from two SiV^- emitters has been demonstrated without using any spectral tunning method.

However, when these emitters are embedded into nanostructures and nanodiamonds, they might exhibit emission intermittency[26, 27] or spectral jumps[28-32]. Even though similar emission behaviors have been investigated on several low-dimensional systems, including nanorods, quantum dots, and molecules[26, 33, 34], the exact photophysical mechanism behind these color centers systems is still unknown and may exhibit some differences compared to the low-dimensional systems. For example, some group IV split vacancy centers show a narrow range spectral diffusion due to their low sensitivity to the fluctuations of the local electric field [35, 36] while the others exhibit emission wavelengths distributed within a wide range along with clear bimodular photon statistics[38]. However, there is no complete understanding of these phenomena till now.

In this Chapter, I present the observation of spectral jumps from single-photon emitters in diamond upon off-resonant excitation. The simultaneously recorded fluorescence from two blinking states exhibit a complete anti-correlation between them, proving both states are originated from the same defect which is confirmed to be a single photon emitter according to the g^2 measurement. Given the stochastic nature of the spectral jumps, only two states are involved. Moreover, the jump rates between states exhibit a quadratic laser-power-dependence, suggesting the states conversion might be a two-photon ionization process. Along with

previous works[30, 37], this study demonstrates that fluorescence intermittency is a ubiquitous phenomenon in solid-state color centers systems, which is mostly associated with a photon-induced ionization process.

4.2 Experimental section

4.2.1 Sample description

The sample is an electronic grade diamond (Type-IIa [N] <1 ppb). To enhance the emitter emission collection, solid immersion lenses (SIL) with a radius of 2.5 μm are fabricated by using focused ion beam milling (Ga^+, flux of 7 nA, 30 keV). After SILs fabrication, the diamond is cleaned with hot Piranha acid for one hour. Then the diamond substrate is exposed to a 7 MeV energy Ge^{4+} ions irradiation, which allows the generation of massive vacancies. To generate GeV^- centers, the sample is annealed in a high vacuum (1×10^{-6} hPa) at 900 °C for two hours.

4.2.2 Experimental setup

The sample is loaded in a Montana cryostat. The sample could be moved in XYZ directions since an XYZ piezo-stepper is employed. To realize a 2D mapping, the incident laser beam path is controlled by an XY Galvo system. We used a 532 nm diode laser to excite the sample or a 513 nm pulsed laser to measure the lifetime. The fluorescence of the sample is collected with a single-mode fiber which could be guided to either a spectrometer for PL measurements or to an avalanche photon diode (APDs) for the count or time-tagged registration. A proper combination of a short pass and long-pass filter is used to suppress the laser scattering or to select a specific emission.

4.3. Spectral jumps

In the following section, the optical properties of the defects are mainly investigated at low temperatures (20 K). I first introduce the investigation of the emitter E1. As shown in Figure 4.1(b), the emitter E1 exhibits a two-line structure (doublet) for both state A (red) and state B (blue). To prove whether both state A and state B belong to the same defect, a g^2 measurement is conducted by using a 600 nm long-pass filter, i.e., the emissions from both states are registered. It turns out that both states belong to the same defect since an antibunching dip deeper than 0.5 is observed (Figure 5.1(c)). The data is fit with a two-level g^2 function

$$g^{(2)}(\tau) = 1 - \alpha \times \exp\left(-\frac{|\tau|}{\tau_{\text{dip}}}\right) \tag{4.1}$$

where τ_{dip} and α represent the width and the depth of the antibunching dip, respectively. An antibunching dip of $g^{(2)}(0) = 0.19 \pm 0.02$ is obtained without any background correction. This proves that these four lines belong to the same emitter which is a single defect.

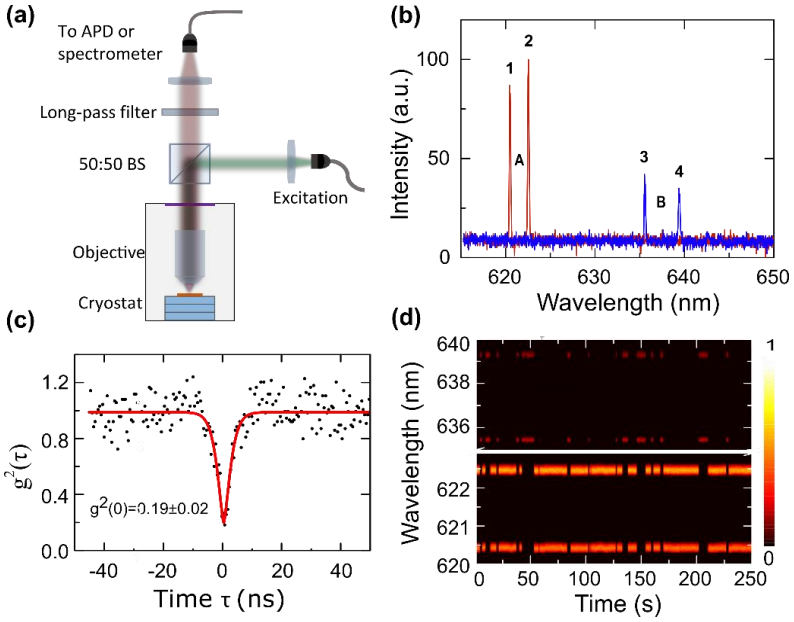

Figure 4.1: Spectral jump of an emitter E1[1]. (a) Cryostation equipped with confocal microscopy. (b) PL spectra of states "A" and "B" were acquired at two different times. The peak 1, 2 of the state "A" spectrum is coded in red, the peak 3, 4 of the state "B" is in blue. Both spectra are recorded at 20 K with an integration time of 0.5 s. (c) g^2 measurement of the emitter E1. The dark dots represent the raw data without background correction. The red curve refers to the fit using a two-level model (equation (4.1)), giving a dip of $g^{(2)}(0) = 0.19 \pm 0.02$). (d) Consecutive and continuous acquisition of 250 spectra, with an exposure time of 0.5 s for each spectrum. Clear anti-correlation between state A and state B is observed. Reproduced with permission [1]. Copyright 2020, Wiley-VCH.

In Figure 4.1(b), the emission energy difference between the shorter and longer wavelengths is greater than 47 meV. Hence, this is unlikely related to the local strain or E-field fluctuations in the diamond[10, 29, 38, 39]. Moreover, the spectral splitting for the short wavelength pair is 6.7 meV while that for the longer wavelength pair is 11.6 meV. Taking these observations into consideration, it might imply that the two doublets in Figure 5.1(b) belong to two different states but are associated with the same emitter. The spectral jumps indicate the states conversion between them. Hence, here the short-wavelength pair (peak 1 and 2) is assigned to state "A" of E1, while the long-wavelength doublet (peak 3 and 4) to state "B". To demonstrate

that there is no additional state involved, a series of spectra are recorded continuously and consecutively over 250 s, with an integration time of 0.5 s per frame. As shown in Figure 4.1 (d), there is no simultaneous detection of both states, no additional states (dark or bright) is involved. Hence, the following spectral dynamics just take states "A" and "B" into consideration.

4.4. Lifetime and temperature dependence

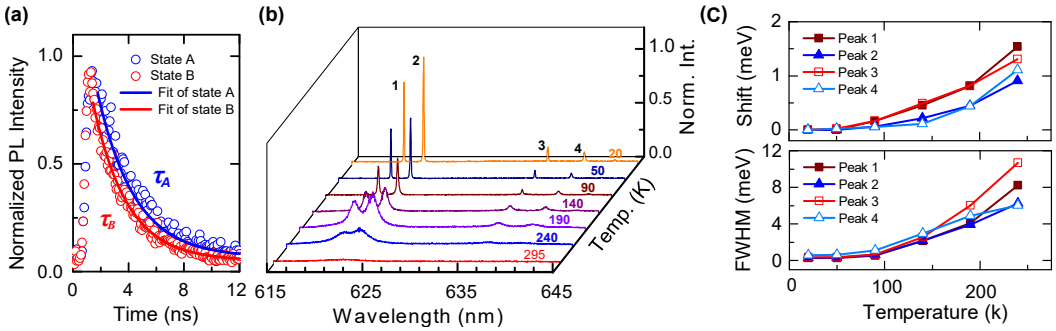

Figure 4.2[1]: (a) Excited state of lifetimes of states "A" and "B" of the emitter E1. The lifetime is measured with a 513 nm pulsed laser under an average excitation power of 200 μW. The emission of states "A" and "B" is selected by using a band-pass filter of 620 ± 7 nm and 640 ± 7 nm respectively. The dot raw data are fit with a single exponential decay (solid line), giving a lifetime of states "A" (τ_A = 2.43 ± 0.03 ns) and "B" (τ_B = 2.67 ± 0.05 ns) respectively. (b) PL spectra of the emitter E1 at different temperatures. A 15 s exposure time per line is used to ensure statistical recording of all four peaks. (c) Temperature-dependent peak wavelengths shifts and FWHM of all peaks extracted by Lorentzian fittings of spectra in (b). Reproduced with permission [1]. Copyright 2020, Wiley-VCH.

The dwell time of an emitter in the excited can be characterized by either the half-width of an antibunching dip or by the lifetime measurement. This dwell time is estimated to be τ_{dip} = 2.44 ± 0.29 ns with first method, which is almost equal to the lifetimes of states "A" and "B" (Figure 4.2(a)). This implies that both states "A" and "B" share a similar radiative quantum efficiency when an off-resonant laser excitation is employed.

To get more insight into the nature of the emitter E1, the temperature-dependent emissions of the emitter E1 are investigated (Figure 4.2(b)). When the working temperature changes from 20 K to 295 K, all transitions exhibit an evident linewidth broadening due to the enhanced coupling to the phonon bath. These emissions at different temperatures could be well fit with four Lorentzian functions, from which the emission center wavelength and linewidth of each peak are extracted and compared (Figure 4.2(c)). All emission lines show almost the same amount of homogeneous broadening from 20 K to 190 K, implying that all transitions have

similar coupling strength to the phonon bath. Moreover, peaks 1 and 3 exhibit a red shift of 1.4 meV; while peaks 2 and 4 red-shifted by 1 meV when the working temperature increases from 20 K to 240 K, implying that the energy level related to transitions 1 and 3 (transitions 2 and 4) might have a similar electronic structure. As such, the electronic structures of transitions 1 and 3 (transitions 2 and 4) could respond similarly to the distortions and lattice vibrations when the temperature changes. Nevertheless, all transitions at 20 K show narrow linewidths less than 0.6 meV and do not exhibit evident PSB up to 290 K.

4.5 ON and OFF time analysis

To delve into the mechanism of the state conversion processes, the PL intermittency duration of both states "A" and "B" are analyzed in this section. In practice, the state "A" exhibits a higher emission count than state "B". Hence, it is possible to determine the state of the emitter by just registering the time-tagged PL intensity (Inset of Figure 4.3(a)). Here, the median of state "A" emission count (120 kcps) and state "B" emission count (60 kcps) is set as the threshold (90 kcps) to determine the ON period duration of state "A". After a histogramming of the ON period of state "A", the statistical occurrences could be cumulatively summed. This gives the occurrence that there is no conversion from state "A" to state "B" within time t, in other words, the fluorescence of state "A" is still ON after time t. By normalizing to the summed conversion events, the probability to have the emitter stay in state "A" for at least a dwell time of t is obtained (Figure 4.3 (a)). This probability should follow a single exponential decay according to the quantum jump theory of incoherent excitation[40]

$$P(t) = \exp(-R_{AB} \times t) \tag{4.2}$$

where $R_{AB} = 1/\tau_{AB}$ is the conversion rate from state A to state B and τ_{AB} is the characteristic time. At such a characteristic time, the state conversion is likely to happen. From the fitting, the $\tau_{AB} = 1/R_{AB} = 4.03 \pm 0.02$ s is obtained when the excitation power is 0.846 mW (see Figure 4.3(a)). These conversion processes are not sensitive to temperature as shown in APPENDIX B Figure B1.

Moreover, the state conversion process speeds up in both directions as the laser power increases (Figure 4.3(b, c)). In particle, both rates R_{AB} and R_{BA} exhibit quadratic dependence over the power follows $R = \beta P^2$ where β defines the conversion efficiency (Figure 4.3(d)). The fact of $\beta_{BA} > \beta_{AB}$ suggests that state "A" should possess lower energy than state "B" (the lower energy one is energy favorable state), though state "A" exhibits higher emission energy than the latter. Since both conversion rates have quadratic power dependences, the emitter would spend $\beta_{AB}/(\beta_{AB} + \beta_{BA})$ proportion of time in state B at equilibrium regardless of the laser power.

Here, it is worth mentioning that the PL energy could not reflect the energies of states A and B, which requires detailed investigations into the local environment including the Fermi level, stains, etc.

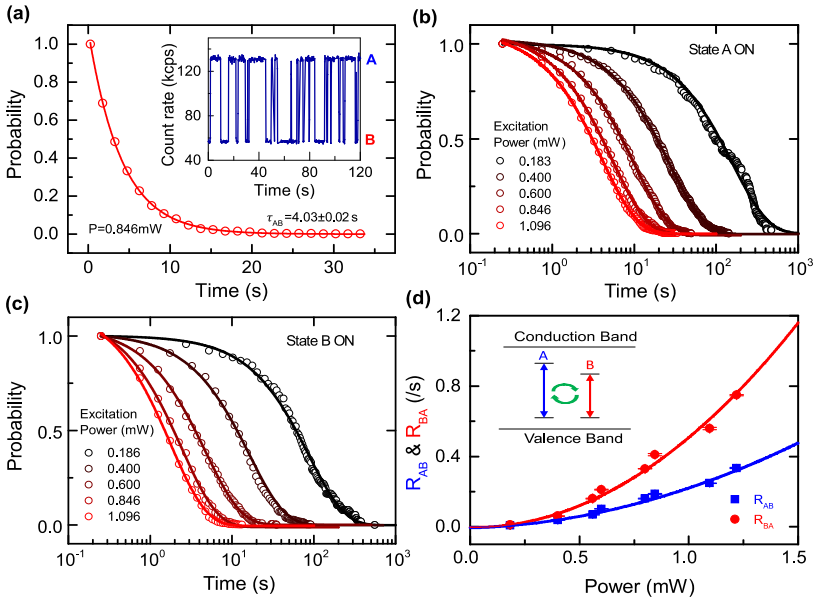

Figure 4.3: Spectral jumps statistics of the emitter E1 at 20 K[1]. (a) Statistics of the "ON" period for state A when the emitter E1 is excited with a 532 nm non-resonant laser (power of 0.846 mW). The red dots are raw data that are extracted from the time-tagged emission. The total acquisition time is about 3 hours. The raw data is fit with a single exponential decay function, resulting in a characteristic time of τ_{AB} = 4.03 ± 0.02 s. Inset: time-tagged fluorescence intensity with a bin size of 0.1 s when both emissions of states "A" and "B" are included with a 600 nm long-pass filter. The dark count is about 100 cps. (b-c) Power dependent probability distribution of the duration of the "ON" period for state "A" (b), and state "B" (c). The solid lines are the fit with a single exponential decay function. (d) State conversion rates from B to A (R_{BA}) and from A to B (R_{AB}). The R is defined by the inverted characteristic times in (b) and (c). The red and blue dots are the raw data, which are fit by $R = \beta P^2$ (P refers to the excitation power and β denotes the state conversion strength). In detail, β_{AB} = 0.24±0.02 Hz mW^{-2} and β_{BA} = 0.51±0.05 Hz mW^{-2}. Inset: Schematic showing of possible conversion processes between the two states. Reproduced with permission [1]. Copyright 2020, Wiley-VCH.

The quadratic power dependence conversion rates have been reported on diamond NV centers [43]. The two-photon ionization process is responsible for the charge state conversion between NV^- and NV^0 centers [30, 41]. Our system may share the same physical process. In detail, the quadratic power dependence is also reported on NV centers in diamond[42], where a two-photon ionization process is proposed to account for the charge state conversions in the NV centers, i.e., between NV^- and NV^0[30, 41]. Similar physics might take place in our system as well: a first

non-resonant photon promotes an electron to the excited level of state “A”, followed by absorption of a second photon which “kicks” out the electron into the conduction band of the host. This “kicks” the emitter into the ground level of state “B” (Figure 4.3(d)). To bring the system back to state “A”, the emitter in state “B” will first absorb a photon, and the electron is shelved into the excited level of state “B”, followed by capturing a free electron which is kicked out from the valence band of the host by a second photon. This brings the emitter into the ground state of state “A”.

4.6 Additional emitters and intensive laser exposure

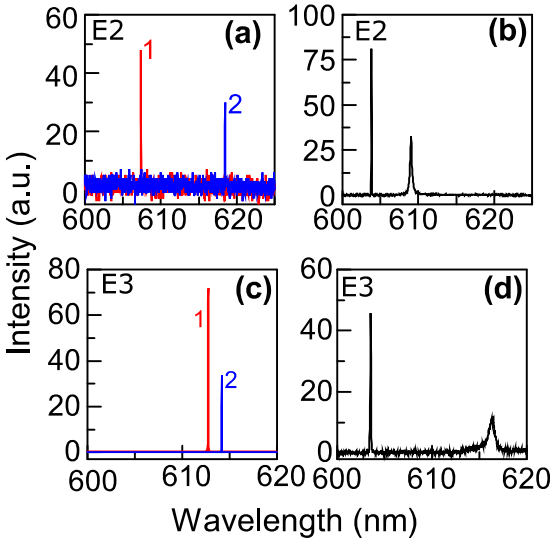

Figure 4.4:Two emitters (E2 and E3) exhibiting spectral jumps[1]. (a) An emitter E2 with spectral jumps between state “1” (607.3 nm) and state “2” (618.5 nm). The E2 is under a 532 nm laser excitation with a power of 0.5 mW. The spectrum integration time is 0.5 s. (b) The Emitter E2 emission after a 30 minutes laser exposure (2 mW). The spectrum is taken for 15 s and is normalized to 0.5 s for comparison. The stabilized peak wavelengths are 603.8 nm and 609.1 nm. (c) An emitter E3 with spectral jumps between state “1” (612.7 nm) and state “2” (614.2 nm). The E2 is under a 532 nm laser excitation with a power of 1 mW. The spectrum is taken for 10 s and is normalized to 0.5 s for comparison. (b) The Emitter E2 emission after an hour of laser exposure (1 mW). The spectrum is taken for 10 s and is normalized to 0.5 s for comparison. The stabilized peak wavelengths are 603.5 nm and 614.4 nm. Reproduced with permission [1]. Copyright 2020, Wiley-VCH.

Besides the emitter E1, binary spectral jumps have also been observed on other emitters (E2 and E3 in Figure 4.4). Different from the doublet spectral structure of the emitter E1, emitters E2 and E3 have just a single line structure at different energies (Figure 4.4). Their different emission wavelengths and spectral structures may be related to the different local strains coupled to different emitters, as observed in the diamond SiV^- system[43, 44]. Despite these

differences, the ON-OFF statistics of both emitters E2 and E3 also follow the single exponential decay (Appendix B Figure B2(b)). Interestingly, the spectral jumps could be quenched if the emitters are exposed to intensive laser power for several hours (APPENDIX B Figure B2(c)). These emitters are stabilized into different emission wavelengths compared to their associated jumping wavelengths. Specifically, the stabilized state of emitters E2 and E3 exhibit emissions near 603 nm (Figure 4.4 (b,d), which are almost identical to the GeV^- color center emission (602 nm). In this regard, these defects may be Ge-related. Even though these defects show spectral jump, they did not exhibit photobleaching or fluorescence reduction during the experiments.

4.7 Discussions and conclusions

In this section, I discuss the possible nature of the above-mentioned observations. The emitters reside in a germanium implanted diamond, however, their emissions are red-shifted by several to tens nanometers and do not show the typical four lines. These behaviors are indeed reported for some strained SiV^- centers in diamond which exhibit a wide range of emission wavelength and do not show the typical four lines[45]. Hence, these emitters in this Chapter may be related to some strain GeV^- centers. In addition, this assumption could be supported by the similar lifetime of these emitters with the GeV^- centers investigated in Chapter 3[46]. However, it is also possible that there are defects presented in the diamond before the Ge^{4+} implantation. These defects are activated after annealing.

Additionally, the investigated emitters in this Chapter could be related to some kind of Ge complexes by drawing experience from the SiV^- center counterpart. It was reported that some Si^+ implanted diamond hosts defects exhibiting red-shifted emissions as compared to the typical emission wavelengths of SiV^- centers. And their emission wavelengths are distributed in a wide range. To explain this phenomenon, people performed the DFT calculation and they associated these defects with abnormal emission wavelength to Si complexes like SiV2, SiV: H1, and so on[45, 47]. Since our observation is quite similar to their case, the deduction of Ge complexes is reasonable.

In this study, the emission wavelengths difference between the two reported blinking state ranges from several tens of nanometer. This figure is way smaller than that of NV^- centers ($\sim$200 nm)[48, 49] and SiV^- centers ($\sim$200 nm)[50], but much greater than the separation reported in semiconductor quantum dots[51]. Given the complete anti-correlation between the two blinking states (Figure 4.1(d)) and all four peaks belonging to the same single-photon emitter

(Figure 4.1c)), the underlying mechanism is unlikely related to charge transfer between several defects.

The blinking and spectral diffusion behaviors of NV centers are generally attributed to the charge dynamics between the emitter and its nearby charge traps[52] (especially emitters near the nanostructure surface) or between the emitter and the conduction or valence band. However, the investigated emitters reside in a SIL which is about 2 μm beneath the sample surface. Hence the emitters are unlikely affected by the traps. A plausible explanation is the local Fermi level fluctuation because of the deionization and ionization of charge traps (P1 centers as an example) surrounding the emitters. The energy of the green laser is sufficient to ionize these traps in diamond. The observation of the disappeared spectral jumps after a long-time high-laser-power exposure might be explained by considering the permanent change of the local Fermi level. This change is allowed via strain relaxations which endows the emitter new configuration.

In conclusion, the spectral jumps of emitters in diamond is observed and investigated closely. The power-dependent spectral jumps rates imply that the jumping process is possibly related to photo-induced ionization. These spectral jumps of these emitters could be eliminated by an intensive laser exposure (Figure 4.4 and Figure B2) or by Fermi level engineering. This is generally realized by p- or n-doping of the host with some atoms with a pre-determined concentration. As such, the local Femi is pinned to support preferred charge states, as demonstrated on SiV^- centers[50] and NV^- centers[53] in diamond.

In the end, I highlight several possible works which may help clarify the nature of the state "A" and "B". The states "A" and "B" are found to have different emission intensities though both states have a comparable radiative lifetime. Additional experiments on the absorption/emission polarization dependence of these two states shed light on this phenomenon. Similar to the diamond SiV^- centers, it is also of importance to look into the magnetic-field-dependent emission of these blinking defects.

References

[1] MU Z, ZHOU Y, CHEN D, et al. Observation of Binary Spectral Jumps in Color Centers in Diamond [J]. Advanced Optical Materials, 2020, 8(19): 2000495.

[2] AHARONOVICH I, ENGLUND D, TOTH M. Solid-state single-photon emitters [J]. Nature Photonics, 2016, 10(10): 631-41.

[3] AWSCHALOM D D, HANSON R, WRACHTRUP J, et al. Quantum technologies with optically interfaced solid-state spins [J]. Nature Photonics, 2018, 12(9): 516-27.

[4] KUCSKO G, MAURER P C, YAO N Y, et al. Nanometre-scale thermometry in a living cell [J]. Nature, 2013, 500(7460): 54-8.

[5] TOYLI D M, DE LAS CASAS C F, CHRISTLE D J, et al. Fluorescence thermometry enhanced by the quantum coherence of single spins in diamond [J]. Proc Natl Acad Sci U S A, 2013, 110(21): 8417-21.

[6] ATATüRE M, ENGLUND D, VAMIVAKAS N, et al. Material platforms for spin-based photonic quantum technologies [J]. Nature Reviews Materials, 2018, 3(5): 38-51.

[7] LADD T D, JELEZKO F, LAFLAMME R, et al. Quantum computers [J]. Nature, 2010, 464(7285): 45-53.

[8] WEBER J R, KOEHL W F, VARLEY J B, et al. Quantum computing with defects [J]. Proc Natl Acad Sci U S A, 2010, 107(19): 8513-8.

[9] DOHERTY M W, MANSON N B, DELANEY P, et al. The nitrogen-vacancy colour centre in diamond [J]. Physics Reports, 2013, 528(1): 1-45.

[10] TAMARAT P, GAEBEL T, RABEAU J R, et al. Stark shift control of single optical centers in diamond [J]. Phys Rev Lett, 2006, 97(8): 083002.

[11] BERNIEN H, CHILDRESS L, ROBLEDO L, et al. Two-photon quantum interference from separate nitrogen vacancy centers in diamond [J]. Phys Rev Lett, 2012, 108(4): 043604.

[12] DAVIES G. Vibronic spectra in diamond [J]. Journal of Physics C: Solid State Physics, 1974, 76(20): 3797.

[13] MANSON N B, HARRISON J P, SELLARS M J. Nitrogen-vacancy center in diamond: Model of the electronic structure and associated dynamics [J]. Physical Review B, 2006, 74(10): 104303.

[14] TAMARAT P, MANSON N B, HARRISON J P, et al. Spin-flip and spin-conserving optical transitions of the nitrogen-vacancy centre in diamond [J]. New Journal of Physics, 2008, 10(4): 045004.

[15] NEU E, STEINMETZ D, RIEDRICH-MöLLER J, et al. Single photon emission from silicon-vacancy colour centres in chemical vapour deposition nano-diamonds on iridium [J]. New Journal of Physics, 2011, 13(2): 025012.

[16] IWASAKI T, ISHIBASHI F, MIYAMOTO Y, et al. Germanium-Vacancy Single Color Centers in Diamond [J]. Sci Rep, 2015, 5: 12882.

[17] PALYANOV Y N, KUPRIYANOV I N, BORZDOV Y M, et al. Germanium: a new catalyst for diamond synthesis and a new optically active impurity in diamond [J]. Sci Rep, 2015, 5: 14789.

[18] ROGERS L J, JAHNKE K D, TERAJI T, et al. Multiple intrinsically identical single-photon emitters in the solid state [J]. Nat Commun, 2014, 5: 4739.

[19] DITALIA TCHERNIJ S, LüHMANN T, HERZIG T, et al. Single-Photon Emitters in Lead-Implanted Single-Crystal Diamond [J]. ACS Photonics, 2018, 5(12): 4864-71.

[20] EVANS R E, BHASKAR M K, SUKACHEV D D, et al. Photon-mediated interactions between quantum emitters in a diamond nanocavity [J]. Science, 2018, 362(6415): 662-5.

[21] BRADAC C, GAO W, FORNERIS J, et al. Quantum nanophotonics with group IV defects in diamond [J]. Nat Commun, 2019, 10(1): 5625.

[22] TRUSHEIM M E, PINGAULT B, WAN N H, et al. Transform-Limited Photons From a Coherent Tin-Vacancy Spin in Diamond [J]. Phys Rev Lett, 2020, 124(2): 023602.

[23] SUKACHEV D D, SIPAHIGIL A, NGUYEN C T, et al. Silicon-Vacancy Spin Qubit in Diamond: A Quantum Memory Exceeding 10 ms with Single-Shot State Readout [J]. Phys Rev Lett, 2017, 119(22): 223602.

[24] HEPP C, MULLER T, WASELOWSKI V, et al. Electronic structure of the silicon vacancy color center in diamond [J]. Phys Rev Lett, 2014, 112(3): 036405.
[25] BHASKAR M K, SUKACHEV D D, SIPAHIGIL A, et al. Quantum Nonlinear Optics with a Germanium-Vacancy Color Center in a Nanoscale Diamond Waveguide [J]. Phys Rev Lett, 2017, 118(22): 223603.
[26] FRANTSUZOV P, KUNO M, JANKó B, et al. Universal emission intermittency in quantum dots, nanorods and nanowires [J]. Nature Physics, 2008, 4(7): 519-22.
[27] BRADAC C, GAEBEL T, NAIDOO N, et al. Observation and control of blinking nitrogen-vacancy centres in discrete nanodiamonds [J]. Nat Nanotechnol, 2010, 5(5): 345-9.
[28] SIYUSHEV P, JACQUES V, AHARONOVICH I, et al. Low-temperature optical characterization of a near-infrared single-photon emitter in nanodiamonds [J]. New Journal of Physics, 2009, 11(11): 113029.
[29] MüLLER T, AHARONOVICH I, LOMBEZ L, et al. Wide-range electrical tunability of single-photon emission from chromium-based colour centres in diamond [J]. New Journal of Physics, 2011, 13(7): 075001.
[30] ASLAM N, WALDHERR G, NEUMANN P, et al. Photo-induced ionization dynamics of the nitrogen vacancy defect in diamond investigated by single-shot charge state detection [J]. New Journal of Physics, 2013, 15(1): 013064.
[31] BERTHEL M, MOLLET O, DANTELLE G, et al. Photophysics of single nitrogen-vacancy centers in diamond nanocrystals [J]. Physical Review B, 2015, 91(3): 035308.
[32] DHOMKAR S, ZANGARA P R, HENSHAW J, et al. On-demand generation of neutral and negatively charged silicon-vacancy centers in diamond [J]. Physical review letters, 2018, 120(11): 117401.
[33] GALLAND C, GHOSH Y, STEINBRüCK A, et al. Two types of luminescence blinking revealed by spectroelectrochemistry of single quantum dots [J]. Nature, 2011, 479(7372): 203-7.
[34] EFROS A L, NESBITT D J. Origin and control of blinking in quantum dots [J]. Nat Nanotechnol, 2016, 11(8): 661-71.
[35] EVANS R E, SIPAHIGIL A, SUKACHEV D D, et al. Narrow-linewidth homogeneous optical emitters in diamond nanostructures via silicon ion implantation [J]. Physical Review Applied, 2016, 5(4): 044010.
[36] SIYUSHEV P, METSCH M H, IJAZ A, et al. Optical and microwave control of germanium-vacancy center spins in diamond [J]. Physical Review B, 2017, 96(8): 081201.
[37] ANDERSON C P, BOURASSA A, MIAO K C, et al. Electrical and optical control of single spins integrated in scalable semiconductor devices [J]. Science, 2019, 366(6470): 1225-30.
[38] DREISER J, ATATüRE M, GALLAND C, et al. Optical investigations of quantum dot spin dynamics as a function of external electric and magnetic fields [J]. Physical Review B, 2008, 77(7): 075317.
[39] DE LAS CASAS C F, CHRISTLE D J, UL HASSAN J, et al. Stark tuning and electrical charge state control of single divacancies in silicon carbide [J]. Applied Physics Letters, 2017, 111(26): 262403.
[40] COOK R J, KIMBLE H J. Possibility of direct observation of quantum jumps [J]. Phys Rev Lett, 1985, 54(10): 1023-6.
[41] SIYUSHEV P, PINTO H, VöRöS M, et al. Optically Controlled Switching of the Charge State of a Single Nitrogen-Vacancy Center in Diamond at Cryogenic Temperatures [J]. Physical Review Letters, 2013, 110(16): 167402.
[42] CHEN X, ZOU C, GONG Z, et al. Subdiffraction optical manipulation of the charge state of nitrogen vacancy center in diamond [J]. Light: Science \& Applications, 2015, 4(1): e230-e.
[43] STERNSCHULTE H, THONKE K, SAUER R, et al. 1.681-eV luminescence center in chemical-vapor-deposited homoepitaxial diamond films [J]. Phys Rev B Condens Matter, 1994, 50(19): 14554-60.
[44] NEU E, HEPP C, HAUSCHILD M, et al. Low-temperature investigations of single silicon vacancy colour centres in diamond [J]. New Journal of Physics, 2013, 15(4).

[45] LINDNER S, BOMMER A, MUZHA A, et al. Strongly inhomogeneous distribution of spectral properties of silicon-vacancy color centers in nanodiamonds [J]. New Journal of Physics, 2018, 20(11): 115002.
[46] CHEN D, MU Z, ZHOU Y, et al. Optical Gating of Resonance Fluorescence from a Single Germanium Vacancy Color Center in Diamond [J]. Phys Rev Lett, 2019, 123(3): 033602.
[47] THIERING G, GALI A. Complexes of silicon, vacancy, and hydrogen in diamond: A density functional study [J]. Physical Review B, 2015, 92(16).
[48] FU K-M, SANTORI C, BARCLAY P, et al. Conversion of neutral nitrogen-vacancy centers to negatively charged nitrogen-vacancy centers through selective oxidation [J]. Applied Physics Letters, 2010, 96(12): 121907.
[49] GROTZ B, HAUF M V, DANKERL M, et al. Charge state manipulation of qubits in diamond [J]. Nat Commun, 2012, 3: 729.
[50] ROSE B C, HUANG D, ZHANG Z H, et al. Observation of an environmentally insensitive solid-state spin defect in diamond [J]. Science, 2018, 361(6397): 60-3.
[51] WARBURTON R J. Single spins in self-assembled quantum dots [J]. Nat Mater, 2013, 12(6): 483-93.
[52] RONDIN L, DANTELLE G, SLABLAB A, et al. Surface-induced charge state conversion of nitrogen-vacancy defects in nanodiamonds [J]. Physical Review B, 2010, 82(11).
[53] FAVARO DE OLIVEIRA F, ANTONOV D, WANG Y, et al. Tailoring spin defects in diamond by lattice charging [J]. Nat Commun, 2017, 8(1): 15409.

Chapter V Coherent manipulation with resonant excitation and single emitter creation of nitrogen-vacancy centers in 4H silicon carbide[1]

5.1 Introduction

Since the discovery of diamond NV^- center, color centers in materials like Si, SiC, and diamond have been intensively investigated for various quantum applications[2-6]. Regarding the diamond NV^- center, the most promising application are the quantum network and quantum sensing[2, 7-12]. However, the visible emission wavelength of NV^- center makes it incompatible with the current fiber-based network, which is a big barrier for long-distance quantum key distribution. Moreover, diamond is a less investigated material in the industry. The cost for high purity diamond growth is always expensive.

By comparison, the industry community had devoted lots of resources to the SiC. The n- and p-doping techniques have been developed, making the PIN junction fabrication feasible[13]. Other benefits include the matured inch-scale wafer growth and nanofabrication techniques. Recently, color centers in SiC exhibit emissions ranging from the visible to the telecom range[14-31]. These defects also have a spin degree of freedom, making them potential spin-photon interfaces. Amongst these SiC defects, the silicon vacancies (V_{Si}^-)[24, 28, 32, 33], and divacancies (VV^0) attracted the most attention. Both the optical and spin properties are them are extensively investigated. Their coherent spin manipulation has also been demonstrated at both room and low temperatures[13-16, 33-35]. However, their emissions are still not in the telecom window.

In the past few years, a new family of defects in SiC are assigned to the $N_CV_{Si}^-$ centers with the combined efforts of the density functional theory (DFT) calculation and the low-temperature electron paramagnetic resonance (EPR) measurements. These $N_CV_{Si}^-$ centers could exist in different polytype hosts of SiC. The $N_CV_{Si}^-$ centers are composed of a nitrogen atom replacing the carbon site and a nearby vacancy on the silicon site. According to the DFT calculation, the $N_CV_{Si}^-$ centers share the energy structure as the diamond NV^- center, including an $^3A_2$ ground state and an ^3E excited state[9], and an intermediate singlet state. Similar to the diamond NV^- center, the presence of the intersystem crossing promises the spin being polarized into a specific ground state. These defects exhibit sharp zero phonon lines at low temperatures.

Accordingly, their ZPLs are closer to the telecom band compared to the V_{Si}^- and VV^0 counterparts, making them appealing for the quantum network application. Compared to these two kinds of defects, the coherent manipulation of $N_CV_{Si}^-$ centers spins has not been realized and the related spin coherence time is still unknown.

In this Chapter, I present the investigation of the optical and spin properties of nitrogen-vacancy centers ($N_CV_{Si}^-$) in 4H-SiC. I first demonstrate the selectively addressing of each kind of $N_CV_{Si}^-$ center via the low-temperature resonant excitation. As such, the optically detected magnetic resonance (ODMR) spectrum of each kind of defect has been characterized. It allows clear identification of ground state zero-field splitting (ZFS) of each kind of defect. After knowing the right excitation wavelength and the ZFS, the coherent manipulation of $N_CV_{Si}^-$ centers has been achieved. From the Rabi and Ramsey experiment, a 400 ns spin dephasing time is extracted. In the end, I show that the single $N_CV_{Si}^-$ center is generated by using nitrogen ion implantation. The associated optical properties of single $N_CV_{Si}^-$ centers are also investigated.

5.2 Experimental settings

The experimental setup for the $N_CV_{Si}^-$ center investigation includes two parts: the optical part and the microwave part (Figure 5.1). For the optical setup, while an off-resonant excitation of a single $N_CV_{Si}^-$ center at room temperature is used, the resonant excitation at low temperature is employed and the phonon sideband of the $N_CV_{Si}^-$ ensemble is collected. In detail, the low dose ion implanted sample is loaded on a piezo-station to perform the 2-dimensional mapping. A 1039 nm laser is used to excite the sample (oil objective, Nikon, NA = 1.35 100X) since this wavelength will not excite the VV^0 centers. The laser is cleaned by using a 1050 nm short pass filter and the emission is collected to a single-mode fiber after passing through an 1150 nm dichroic mirror and a 1200 nm long pass filter. The collected photons are split into two channels and are guided into a superconducting detector (Scontel) to perform the g^2 measurement. To identify the generation of $N_CV_{Si}^-$ centers, the high-dose ion-implanted samples are loaded in a Montana Cryostation, equipped with an IR objective (Olympus, NA = 0.65, 50X). A 980 nm laser cleaned with a 1000 short pass is employed to excite the samples whose emissions are guided into a spectrometer (Andor, InGaAs detector). Regarding the resonant excitation, a diode laser operating from 1160 nm to 1250 nm is used. To get a high signal-noise ratio, the excitation laser is cleaned with suitable bandpass filters and only the emission of $N_CV_{Si}^-$ center into the phonon sideband is counted (a combination of 1250 nm long pass and a 1300 nm bandpass filter).

5.2.1 Experimental setup

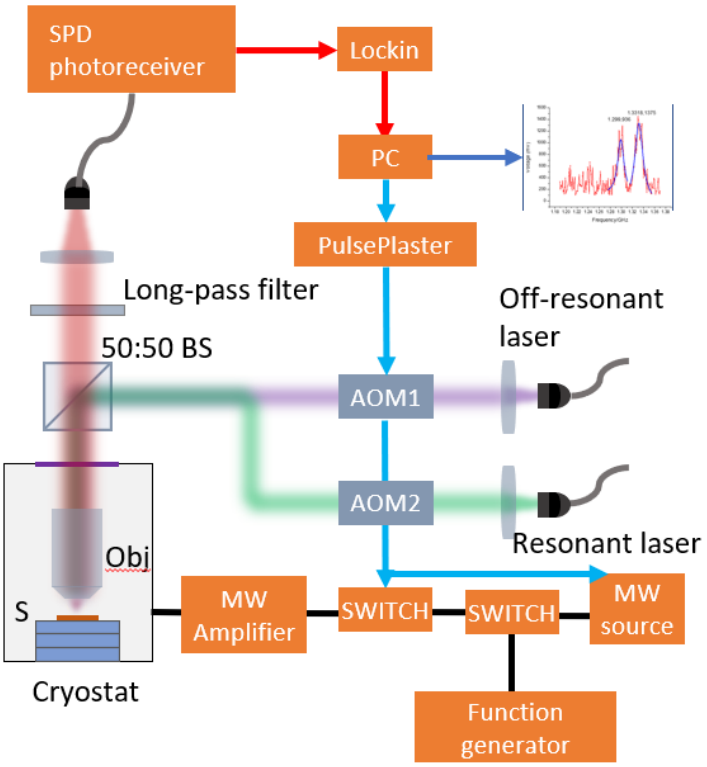

Figure 5.1: Experimental setup for $N_CV_{Si}^-$ centers measurements. The defects are loaded in a cryostat which is interfaced with lasers (off-resonant and resonant lasers) and MWs (CW or pulsed). The MW is gated with a PulsePlaster. The laser/MW sequences are controlled with the PulsePlaster. The emission photons are collected into either an SSPD or a photoreceiver. The ODMR signal could be extracted by a Lock-in amplifier.

To realize the spin control, a gold strip line with a linewidth of 20 μm or an 80 μm ring is fabricated on the SiC sample. These gold pads are wire bonded to chip carriers. A microwave source (Rohde&Schwarz SMIQ) is connected to a microwave switch (ZASWA-2-5-DRA+). The ON/OFF of this switch is controlled by a function generator. Then the chopped microwave is connected to an MW amplifier before feeding into the Montana Cryostation. Since the MW is switched ON/OFF periodically, the SSPD registered counts are time tagged which allows the extraction of photon count variation at the modulation frequency. For the pulsed experiment (Rabi and Ramsey), a second switch is employed. The second switch is utilized for the MW pulse generation[14, 36].

5.2.2 Sample preparation

In this study, two types of $N_CV_{Si}^-$ centers are fabricated based on a different purpose. To generate $N_CV_{Si}^-$ centers with high concentrations, a highly nitrogen doped SiC ($2x10^{17}/cm^3$)

substrate is employed. The substrate is irradiated with 12 MeV protons (fluency of $10^{16}/cm^2$). The $N_CV_{Si}^-$ centers are activated by high-temperature annealing (900 °C). The estimated $N_CV_{Si}^-$ centers concentration is about $10^{16}/cm^3$[37]. To get the microwave feeding through, the microwave guides are deposited on the SiC surface[36].

To generate single $N_CV_{Si}^-$ centers, the SiC substrates are irradiated with nitrogen ions. The substrate is purchased from Norstel. For both the bulk ion implantation and the focused ion beam implantation, the ion energy is fixed at 30 keV. The ion fluency and the dwell time at each site could be controlled to generate single defects. After irradiation, the substrate is annealed at either 800 °C or 1000 °C to form $N_CV_{Si}^-$ center. The annealed substrate is cleaned with hot Piranha acid (150 °C) for 1 hour.

5.3 Four types of $N_CV_{Si}^-$ centers in 4H-SiC

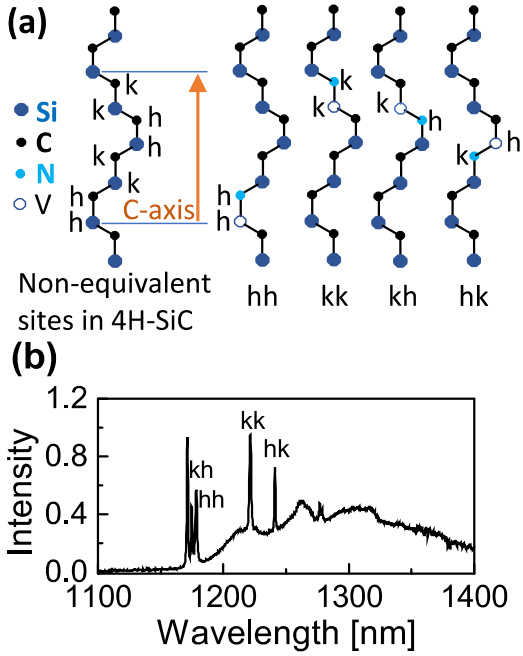

Figure 5.2: $N_CV_{Si}^-$ centers in 4H-SiC[1]. (a) $N_CV_{Si}^-$ centers configurations in 4H-SiC. The four types of $N_CV_{Si}^-$ centers are shown. The $N_CV_{Si}^-$ centers are composed of vacancies replacing the silicon sites and nitrogen atoms occupying the carbon sites. (b) PL spectrum of $N_CV_{Si}^-$ centers under 980 nm excitation at 10 K. The distinct ZPL of each kind of $N_CV_{Si}^-$ centers is indicated. Reproduced with permission [1]. Copyright 2020, American Chemical Society.

There are hexagonal and cubic sites for both the silicon and carbon atoms in 4H-SiC. It thus allows the 4H-SiC to host several types of $N_CV_{Si}^-$ centers. Generally, it is energy favorable that the nitrogen atoms replace the carbon sites rather than the silicon sites. As a result, there are four types of $N_CV_{Si}^-$ centers in the 4H-SiC (Figure 5.2a). These defects exhibit different optical

and spin properties. The successful generation of $N_CV_{Si}^-$ centers is demonstrated with the low-temperature emission spectra (Figure 5.2b), from which the zero-phonon line related to each kind of defect is labeled accordingly[19, 23, 38]. Besides this, the presence of $N_CV_{Si}^-$ centers is demonstrated by performing high-resolution electron magnetic resonance (EPR) measurements. From the EPR spectra (APPENDIX C Figure C2), the intrinsic hyperfine structure originated from the hyperfine interaction between the $N_CV_{Si}^-$ centers and the nitrogen nuclear spin (I = 1) is extracted. The hyperfine strength extracted from the triplet splitting matches well with the DFT calculations. Since there are co-exist of all four types of $N_CV_{Si}^-$ centers within the laser excitation volume, it is inevitable to excite all of them under off-resonant excitation. Hence, it complicates the signal identification associated with each kind of defect. In the following, we employed the resonant excitation to selectively address each kind of defect.

5.4 Optically and microwave-assisted resolved of fine structures of each type of $N_CV_{Si}^-$ centers

To realize individual defect manipulation, the idea is to perform resonant excitation at low temperatures. In practice, the absorption spectra associated with each kind of defect are identified by sweeping the laser wavelength across the ZPL wavelengths of them while monitoring their emission into the PSB. To minimize the simultaneous excitation of all defects, a laser power of 10 μW is employed and the sweeping wavelength step is set to 0.1 nm. As shown in Figure 5.3(a), when the laser is off-resonant with the defect, the normalized emission count is just at a background level. These defects exhibit narrow absorption linewidths about 1 nm. This highly selective absorption wavelength would promise ZFS identification of each kind of defect by just parking laser wavelength on the specific defect. Interestingly, the basal centers exhibit only one peak in the photoluminescence spectra, whereas the axial centers have a doublet structure showing a peak wavelength difference of 0.7 nm. The doublet peaks are labeled as PK1 and PK2 for hh centers and those for kk centers are named as PK1' and PK2'. According to [23, 38], this doublet structure may be related to the existence of two close excited states for axial $N_CV_{Si}^-$ centers. Because of the lower symmetry of basal centers, this doublet structure is not observed. However, a more detailed investigation is required to understand the origin of doublet and the different absorption behavior between the axial and basal centers.

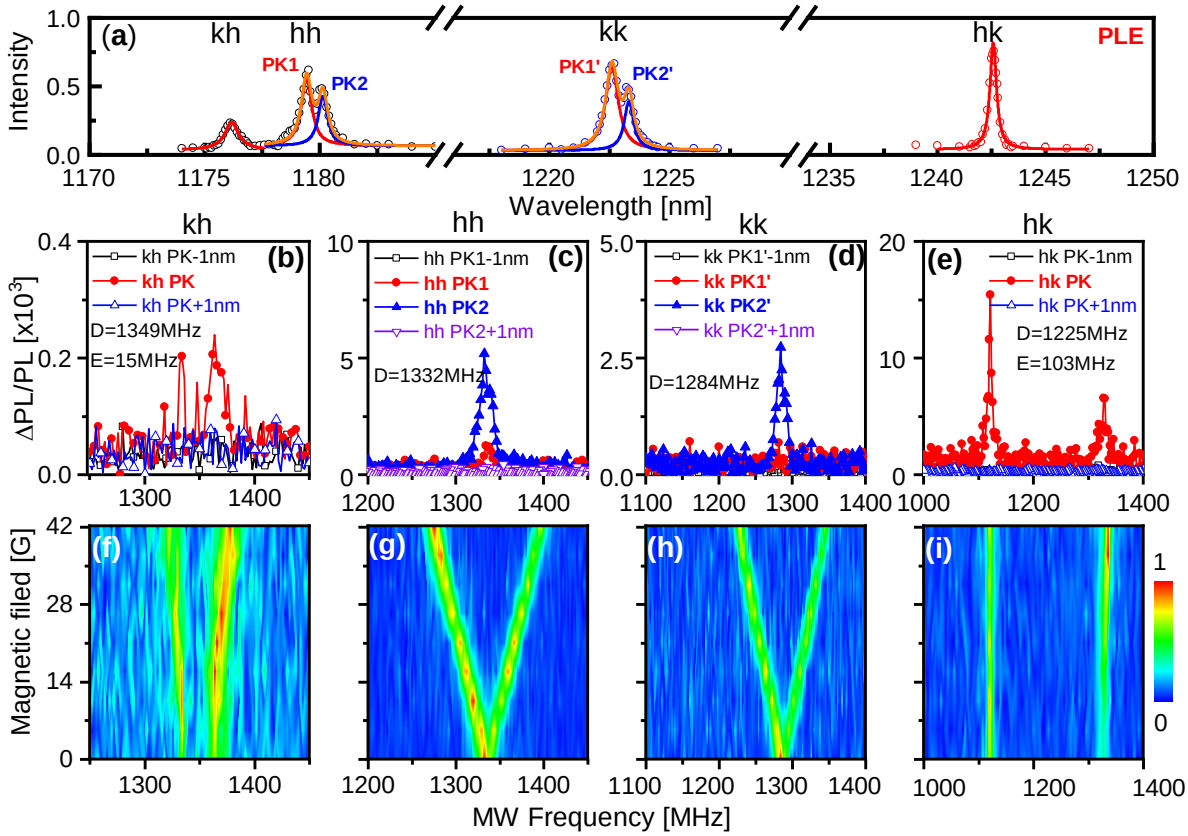

Figure 5.3: Low-temperature photoluminescence excitation of $N_CV_{Si}^-$ center and their ODMR spectra[1]. (a) Photoluminescence excitation of $N_CV_{Si}^-$ centers. Dots represent the experimental data. The absorption spectra are fit with Lorentz functions. The peak absorption wavelength and linewidth are 1176.170nm/0.731nm (kh), 1242.571 nm/0.366 nm (hk), 1179.419 nm/0.547nm (PK1 of hh) and 1180.130nm/0.497nm (PK2 of hh), 1222.596 nm/0.641 nm (PK1' of kk) and 1223.303 nm/0.473 nm (PK2' of kk). (b. c. d. e) The Zero-field ODMR spectra under resonant and off-resonant excitation (1 nm detuned from the peak in Figure 5.3a). (f.g.h.i) ODMR spectra under external magnetic field. Reproduced with permission [1]. Copyright 2020, American Chemical Society.

To realize efficient microwave-driven $N_CV_{Si}^-$ centers spins, microwave antennas are fabricated on the epitaxial layer side of SiC. By parking the laser on resonant with a specific type of $N_CV_{Si}^-$ center, the spins of the corresponding defect are then polarized into a certain state. The ZFS of this given defect could be identified by sweeping the MW frequency while monitoring the defect emission change. When the MW frequency is resonant with the ground state transitions, the emissions of the defect would be increased or decreased depending on the spin being polarized into a bright or dark state. During the experiment, a lock-in method is used to extract the count variation at different MW frequencies. In detail, the microwave is turned ON and OFF by a function generator with a frequency of 134 Hz. If the MW is resonant with the GS transition, the emission would exhibit a time-dependent emission at this frequency.

Hence, the count rate variation could be extracted by utilizing the Fourier transformation of a time-tagged count sequence [14, 36]. Figure 5.3(b-e) presents the ODMR spectra of all four types of $N_CV_{Si}^-$ centers under resonant and off-resonant excitation. During the experiment, the MW frequency is swept from 1 GHz to 1.4 GHz while the laser power is kept constant at different excitation wavelengths. As expected, only when the laser is resonant with the specific defect there are ODMR signals. The eigenstates of an S = 1 system could be estimated with the following Hamiltonian which includes the Zeeman effect but neglects the interaction with nuclear spins [15, 39]:

$$H = \mu_B g\boldsymbol{B}\cdot\boldsymbol{S} + \hbar D\left[S_Z^2 - \frac{1}{3}S(S+1)\right] + \hbar E(S_X^2 - S_Y^2) \qquad (5.1)$$

Where μ_B is the Bohr magneton, g is the Lande g-factor, B is the external magnetic field, and D and E are named the longitudinal and transverse zero-field splitting respectively. The Eparameter is zero for axial $N_CV_{Si}^-$ centers while it is non-zero for basal centers. This difference is because the axial centers have a high symmetry, but the basal centers have a lower symmetry which lifted the degeneracy of the $m_s = \pm 1$ sublevels. Hence, there is just a peak in the ODMR spectrum of axial centers; there are two peaks for basal centers (Figure 5.3(b-e) whose frequencies are defined by $D \pm E$. The D and E values for each defect are indicated in each figure. The D and E values acquired with our ODMR measurement and previous EPR results are summarized in Table S1 in the supplementary information. Since the ODMR measurement has a higher resolution, our works allow the refinement of the ZFS values of $N_CV_{Si}^-$ centers.

By looking closer into Figures 5.2(c) and (d), it is found that the two peaks wavelengths give different ODMR contrast. The doublet absorption associated with the hh and kk centers shown in Figure 5.2a had also been observed in the previously reported low-temperature EPR measurements. During the EPR measurements, the authors changed the laser excitation wavelengths which promise different spin polarization ratios. Meanwhile, they monitor how the microwave signal changes at different excitation wavelengths. If the spin polarization ratio is higher, the microwave signal change should be higher. The authors found that the EPR signals are most intensive when the laser wavelength is resonant with the $N_CV_{Si}^-$ centers; however, both peak wavelengths lead to comparable EPR signals, i.e., comparable spin polarization ratio. Unlike these results, the two peak wavelengths PK1 (PK1') verse PK2 (PK2') lead to different ODMR signals here. In detail, when a laser is parked at PK1, the ODMR intensity (Figure 5.2(c) red line) is about four time weaker than the case where a laser is parked at PK2 (Figure 5.2(c) blue line). This excitation wavelength selectivity is more evident for the

kk centers, for which the ODMR peak can only be revealed with laser parking on PK2'. Both results suggest that spin polarization is most efficient when the $N_CV_{Si}^-$ centers are excited into the lower excited states. Since the spin polarization is realized via the intersystem crossing process [9], our results may indicate the different coupling strength between the two excited states and the metastable state [9, 23]. The different coupling strength is responsible for the different spin initialization.

After knowing the zero-field splitting of each defect, their response to the external magnetic field is investigated. In practice, an external magnetic field is applied which formed a 4-degree angle with respect to the sample surface. The maximum magnetic field is 42 Gauss. The typical Zeeman splitting is observed for axial centers (Figure 5.3(g) and (h)), which is in good agreement with the microscopic model described by equation 5.1. Regarding the basal center, their transition frequencies shift weakly. Compared kh centers to hk centers, the transition frequencies of the latter ones are less sensitive to the external magnetic field due to the larger transverse splitting. The transition frequencies of the axial and basal centers under external magnetic field follow the $\sqrt{(g\mu_B B/\hbar)^2 + E^2}$, where B represents the components projected onto the quantization axis of the axial and basal centers.

5.5 Coherent manipulation of ensemble $N_CV_{Si}^-$ centers

The spin dephasing and coherence time of defects are of importance for quantum gate operation and quantum sensing. The dephasing time could be extracted by performing the Ramsey experiment while the coherent transfer spin population is demonstrated with the Rabi experiment. In this work, I demonstrate the coherent manipulation of kk axial centers. Since it is an axial center, a weak magnetic field (18 Gauss) is applied to lift the degeneracy of $m_s = \pm 1$ states. Then the high transition frequency is selected to perform the spin manipulation. The initialization and readout laser pulsed are set to 5 μs. For the Rabi measurement, the MW pulse length changes from 10 ns to 2 μs. In Figure 5.4(a), the coherent manipulation of $N_CV_{Si}^-$ centers is demonstrated with the observed oscillating population in the $m_s = 0$ states. The population evolution process is fit with a decaying sinusoidal function (equation 5.2), which gives a Rabi frequency of 3.12 ± 0.11 MHz along with an amplitude decay time of 376 ± 24 ns.

$$I = A + B\cos(2\pi f t)\exp(-t/T) \tag{5.2}$$

From the Rabi experiment, the π/2 pulse length is estimated. The Ramsey experiment is performed employing the known π/2 pulse length to extract the associated dephasing time (T_2^*)

of kk centers by a 2 MHz detuned microwave pulse (Figure 5.4(b) Inset). The dephasing time is then obtained by fitting the data with equation (5-3), from which a spin dephasing time of 388 ± 136 ns is estimated.

$$I = A' + B' \cos(2\pi f' t + \varphi') \exp(-t/T_2') \tag{5.3}$$

This result is comparable with the dephasing time of the kk divacancy center in 4H-SiC (T_2^* ~ 185 ns)[14]. The current measurement was based on a sample with high nitrogen impurity and high nitrogen-vacancy concentration. The spin-spin interaction between the $N_C V_{Si}^-$ centers and nitrogen impurity might shorten the dephasing[21]. Hence, a longer dephasing could be expected if the spin manipulation is at a single level.

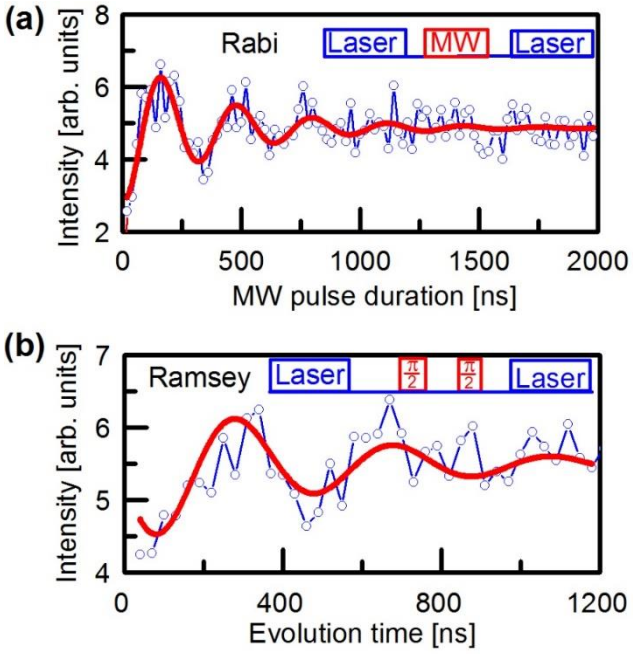

Figure 5.4: Coherent manipulation of kk centers under an 18 Gauss magnet[1]. (a) The Rabi oscillation. (b) The Ramsey fringe. Reproduced with permission [1]. Copyright 2020, American Chemical Society.

5.6 Single $N_CV_{Si}^-$ centers generation with nitrogen implantation

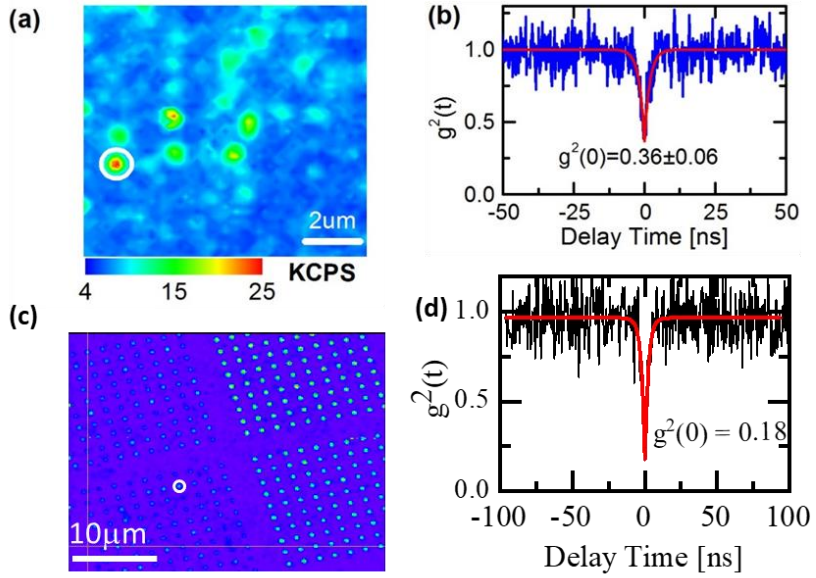

Figure 5.5: Single $N_CV_{Si}^-$ center generation with bulk and focused ion beam implantation[1]. (a) The 2D mapping of a low-dose nitrogen implanted sample. The single $N_CV_{Si}^-$ center is highlighted with a white circle. (b) The g^2 measurement of the circled emitter without background correction. The blue line is the experimental result and the red line is the fit. A dip of 0.36 ± 0.06 is obtained from the fit. Reproduced with permission [1]. Copyright 2020, American Chemical Society. (c) The 2D mapping of defects array generated with focused ion beam implantation. The scale bar is 10 μm. (d) The g^2 measurement of the circled spots in (c). The $g^2(0) = 0.18$ according to the fit.

The benefit of proton irradiation is to generate a high density of emitters since it could penetrate the sample by tens μm if hundreds of keV energy is employed. By comparison, the low-energy ion implantation is preferred for single defect generation because the ions brought by the implantation could determine the position and the number of defects. Here, both bulk ion implantation and focused ion beam implantation are employed to generate single $N_CV_{Si}^-$ centers. To generate single defects, the nitrogen implantation fluency and dwell time are delicately controlled. The irradiated sample is then annealed at 1000 °C for 1 hour in a high vacuum environment. The $N_CV_{Si}^-$ centers generation is demonstrated by measuring the photoluminescence of the sample at 10 K. As shown in Figure C3 (APPENDIX C), only ZPL related to $N_CV_{Si}^-$ centers are observed under 980 nm laser excitation. This on one hand proves the generation of $N_CV_{Si}^-$ centers with nitrogen implantation. On the other hand, the negligible emission of divacancy proves that the major generated defects in the host are $N_CV_{Si}^-$ centers.

By carefully tuning the implantation dose, single $N_CV_{Si}^-$ centers are observed in a sample irradiated with a dost of $10^{10}/cm^2$. Shown in Figure 5.5(a), several emitters are scattered in a 10 μm x 10 μm area. To suppress the potential emission coming from the divacancies, a 980 nm is used for the excitation and photons are collected with a 1200 nm long-pass filter. The circled spots are proved to be a single photon emitter by performing the HBT measurement. The normalized raw data is shown in the blue line. The curve is fit with a two-level system, from which a $g^2(0) = 0.36 \pm 0.06 < 0.5$ is extracted. The non-ideal single-photon emission is due to the moderate signal-noise ratio, i.e., the saturation emission of the single emitter is just 17 K after background correction while the background emission is about 10 K. The $g^2(0)$ equals 0.01 after background correction. (Shown in APPENDIX C Figure C4). From the fitting, an excited state lifetime of 2.21 ns is estimated, which is much shorter than that of the VV^0 centers [16]. Moreover, the single-photon emission of the investigated emitter is demonstrated by its saturated emission. When the excitation laser power increases, the electron will be pumped into a metastable state. Hence, the bunching effect is observed in the g^2 curve (as shown in APPENDIX C Figure C7). From the fitting, a metastable lifetime of several hundreds of nanoseconds is acquired. Besides this defect, the optical properties of other single-photon emitters could be found in Figure C6 (APPENDIX C).

5.7 Discussions and conclusions

It is always on demand that the optical and spin properties of defects could be investigated at a single level. However, the bulk host intrinsically brings collection loss due to the total reflection of the surface. Besides the collection, the quantum efficiency of emitters is also of importance. In this regard, it is of importance to couple the emitter to cavities or nanostructures. To enhance either the emission or boost the collection efficiency, the relative position of the defects and the nanofabricated structure is of vital importance. This demand, in return, requires the deterministic generation of single defects with high spatial precision. Here, with the focused ion beam implantation, I demonstrate massive generation of single $N_CV_{Si}^-$ centers in SiC (shown in Figure 5.5(c) and (d)). Hence, the next step is to find a proper method to combine the defect with nanostructures.

In conclusion, the distinct ODMR spectra associated with each kind of $N_CV_{Si}^-$ center is obtained by utilizing the low-temperature resonant excitation. This method is proved to be a powerful method to selectively identify the spin properties of one kind of defect among many defects. Thanks to this, the coherent spin manipulation is realized, and based on which a

dephasing time of 400 ns is estimated. To go further, I successfully generated single $N_CV_{Si}^-$ centers and observed their weak emission compared to the diamond NV^- center. This highlights the importance of enhancing $N_CV_{Si}^-$ centers' emission with nanostructures like photonic crystal cavities [40, 41] or solid immersion lenses [18, 42]. The study on the single $N_CV_{Si}^-$ center generation with ion beam implantation would pave the way to future quantum applications with enhanced single $N_CV_{Si}^-$ center emission.

References

[1] MU Z, ZARGALEH S A, VON BARDELEBEN H J, et al. Coherent Manipulation with Resonant Excitation and Single Emitter Creation of Nitrogen Vacancy Centers in 4H Silicon Carbide [J]. Nano Lett, 2020.

[2] CHILDRESS L, HANSON R. Diamond NV centers for quantum computing and quantum networks [J]. MRS Bulletin, 2013, 38(2): 134-8.

[3] ATATüRE M, ENGLUND D, VAMIVAKAS N, et al. Material platforms for spin-based photonic quantum technologies [J]. Nature Reviews Materials, 2018, 3(5): 38-51.

[4] AWSCHALOM D D, HANSON R, WRACHTRUP J, et al. Quantum technologies with optically interfaced solid-state spins [J]. Nature Photonics, 2018, 12(9): 516-27.

[5] BRADAC C, GAO W, FORNERIS J, et al. Quantum nanophotonics with group IV defects in diamond [J]. Nature Communications, 2019, 10(1): 5625.

[6] BUTERAKOS D, BARNES E, ECONOMOU S E. Deterministic Generation of All-Photonic Quantum Repeaters from Solid-State Emitters [J]. Physical Review X, 2017, 7(4): 041023.

[7] FUCHS G D, BURKARD G, KLIMOV P V, et al. A quantum memory intrinsic to single nitrogen–vacancy centres in diamond [J]. Nature Physics, 2011, 7(10): 789-93.

[8] SAITO S, ZHU X, AMSüSS R, et al. Towards Realizing a Quantum Memory for a Superconducting Qubit: Storage and Retrieval of Quantum States [J]. Physical Review Letters, 2013, 111(10): 107008.

[9] SCHIRHAGL R, CHANG K, LORETZ M, et al. Nitrogen-vacancy centers in diamond: nanoscale sensors for physics and biology [J]. Annu Rev Phys Chem, 2014, 65: 83-105.

[10] CUJIA K S, BOSS J M, HERB K, et al. Tracking the precession of single nuclear spins by weak measurements [J]. Nature, 2019, 571(7764): 230-3.

[11] DEGEN C L, REINHARD F, CAPPELLARO P. Quantum sensing [J]. Reviews of Modern Physics, 2017, 89(3): 035002.

[12] SHI F, KONG X, WANG P, et al. Sensing and atomic-scale structure analysis of single nuclear-spin clusters in diamond [J]. Nature Physics, 2014, 10(1): 21-5.

[13] ANDERSON C P, BOURASSA A, MIAO K C, et al. Electrical and optical control of single spins integrated in scalable semiconductor devices [J]. Science, 2019, 366(6470): 1225-30.

[14] KOEHL W F, BUCKLEY B B, HEREMANS F J, et al. Room temperature coherent control of defect spin qubits in silicon carbide [J]. Nature, 2011, 479(7371): 84-7.

[15] FALK A L, BUCKLEY B B, CALUSINE G, et al. Polytype control of spin qubits in silicon carbide [J]. Nat Commun, 2013, 4: 1819.

[16] CHRISTLE D J, FALK A L, ANDRICH P, et al. Isolated electron spins in silicon carbide with millisecond coherence times [J]. Nat Mater, 2015, 14(2): 160-3.

[17] VON BARDELEBEN H J, CANTIN J L, RAULS E, et al. Identification and magneto-optical properties of the NV center in 4H−SiC [J]. Physical Review B, 2015, 92(6): 064104.

[18] WIDMANN M, LEE S Y, RENDLER T, et al. Coherent control of single spins in silicon carbide at room temperature [J]. Nat Mater, 2015, 14(2): 164-8.

[19] VON BARDELEBEN H J, CANTIN J L, CSóRé A, et al. NV centers in3C,4H, and6Hsilicon carbide: A variable platform for solid-state qubits and nanosensors [J]. Physical Review B, 2016, 94(12): 121202.

[20] ZARGALEH S A, EBLE B, HAMEAU S, et al. Evidence for near-infrared photoluminescence of nitrogen vacancy centers in4H-SiC [J]. Physical Review B, 2016, 94(6): 060102.

[21] KOEHL W F, DILER B, WHITELEY S J, et al. Resonant optical spectroscopy and coherent control ofCr4+spin ensembles in SiC and GaN [J]. Physical Review B, 2017, 95(3): 035207.

[22] WANG J, ZHANG X, ZHOU Y, et al. Scalable Fabrication of Single Silicon Vacancy Defect Arrays in Silicon Carbide Using Focused Ion Beam [J]. ACS Photonics, 2017, 4(5): 1054-9.

[23] ZARGALEH S A, VON BARDELEBEN H J, CANTIN J L, et al. Electron paramagnetic resonance tagged high-resolution excitation spectroscopy of NV-centers in 4H-SiC [J]. Physical Review B, 2018, 98(21): 214113.

[24] BANKS H B, SOYKAL Ö O, MYERS-WARD R L, et al. Resonant Optical Spin Initialization and Readout of Single Silicon Vacancies in 4H-SiC [J]. Physical Review Applied, 2019, 11(2): 024013.
[25] DILER B, WHITELEY S J, ANDERSON C P, et al. Coherent control and high-fidelity readout of chromium ions in commercial silicon carbide [J]. arXiv preprint arXiv:190908778, 2019.
[26] GILARDONI C M, BOSMA T, VAN HIEN D, et al. Spin-relaxation times exceeding seconds for color centers with strong spin-orbit coupling in SiC [J]. arXiv preprint arXiv:191204612, 2019.
[27] KHAZEN K, VON BARDELEBEN H J, ZARGALEH S A, et al. High-resolution resonant excitation of NV centers in 6H−SiC: A matrix for quantum technology applications [J]. Physical Review B, 2019, 100(20): 205202.
[28] NAGY R, NIETHAMMER M, WIDMANN M, et al. High-fidelity spin and optical control of single silicon-vacancy centres in silicon carbide [J]. Nat Commun, 2019, 10(1): 1954.
[29] SPINDLBERGER L, CSóRé A, THIERING G, et al. Optical Properties of Vanadium in 4H Silicon Carbide for Quantum Technology [J]. Physical Review Applied, 2019, 12(1): 014015.
[30] VON BARDELEBEN H J, ZARGALEH S A, CANTIN J L, et al. Transition metal qubits in $4H$-silicon carbide: A correlated EPR and DFT study of the spin $S=1$ vanadium ${\mathrm{V}}^{3+}$ center [J]. Physical Review Materials, 2019, 3(12): 124605.
[31] WOLFOWICZ G, ANDERSON C P, DILER B, et al. Vanadium spin qubits as telecom quantum emitters in silicon carbide [J]. arXiv preprint arXiv:190809817, 2019.
[32] SIMIN D, KRAUS H, SPERLICH A, et al. Locking of electron spin coherence above 20 ms in natural silicon carbide [J]. Physical Review B, 2017, 95(16): 161201.
[33] SOLTAMOV V A, KASPER C, POSHAKINSKIY A V, et al. Excitation and coherent control of spin qudit modes in silicon carbide at room temperature [J]. Nature Communications, 2019, 10(1): 1678.
[34] CHRISTLE D J, KLIMOV P V, DE LAS CASAS C F, et al. Isolated Spin Qubits in SiC with a High-Fidelity Infrared Spin-to-Photon Interface [J]. Physical Review X, 2017, 7(2): 021046.
[35] MIAO K C, BOURASSA A, ANDERSON C P, et al. Electrically driven optical interferometry with spins in silicon carbide [J]. Science Advances, 2019, 5(11): eaay0527.
[36] ZHOU Y, WANG J, ZHANG X, et al. Self-Protected Thermometry with Infrared Photons and Defect Spins in Silicon Carbide [J]. Physical Review Applied, 2017, 8(4): 044015.
[37] ZARGALEH S A, VON BARDELEBEN H J, CANTIN J L, et al. Electron paramagnetic resonance tagged high-resolution excitation spectroscopy of NV-centers in 4H-SiC [J]. Physical Review B, 2018, 98(21).
[38] CSóRé A, VON BARDELEBEN H J, CANTIN J L, et al. Characterization and formation of NV centers in $3C, 4H$, and $6H$ SiC: An ab initio study [J]. Physical Review B, 2017, 96(8): 085204.
[39] RONDIN L, TETIENNE J P, HINGANT T, et al. Magnetometry with nitrogen-vacancy defects in diamond [J]. Reports on Progress in Physics, 2014, 77(5): 056503.
[40] SCHRODER T, TRUSHEIM M E, WALSH M, et al. Scalable focused ion beam creation of nearly lifetime-limited single quantum emitters in diamond nanostructures [J]. Nat Commun, 2017, 8: 15376.
[41] LIU J, SU R, WEI Y, et al. A solid-state source of strongly entangled photon pairs with high brightness and indistinguishability [J]. Nature Nanotechnology, 2019, 14(6): 586-93.
[42] CHEN D, MU Z, ZHOU Y, et al. Optical Gating of Resonance Fluorescence from a Single Germanium Vacancy Color Center in Diamond [J]. Physical Review Letters, 2019, 123(3): 033602.

Chapter VI Conclusions and outlooks

6.1 Conclusions

In conclusion, I investigated two types of spin-photon interfaces. For diamond Group-IV split vacancy centers, we observed a dark state besides the typical quartet ground and excited states. This dark state quenches GeV^- centers' emissions upon a resonant excitation. It may be related to another charged state of GeV^- centers and could be brought back to a bright state with an extra non-resonant excitation. Importantly, the application of an additional non-resonant laser does not deteriorate the coherence properties of the GeV^- centers. Without losing generality, this method could be applied to other solid-state systems. This result is important for the scalable quantum network application.

I also observed the binary spectral jumps of Ge-related defects upon off-resonant excitation. The spectral jumps between two states are suggested to be originated from the localized Fermi level pinning. This pinning effect is likely to happen during ion implantation and nanostructure fabrication. Hence, it underscores the importance of knowing and controlling the charge environment of color centers. This study provides extra insight into the two aspects (charge and optical properties) of SPEs, which would benefit the fabrication of a scalable quantum network from a sample preparation perspective.

The search for SPEs with telecom wavelength emission is still vital for the color centers community. I successfully generated single $N_CV_{Si}^-$ centers in SiC with ion implantation and focused ion implantation. The optical properties of single $N_CV_{Si}^-$ centers (lifetime, emission counts, stability) were investigated. Moreover, our work revealed the ground state ZFS associated with each $N_CV_{Si}^-$ center type. These results would pave the way for the optical and microwave control of single $N_CV_{Si}^-$ centers in the short term.

6.2 Outlooks

As mentioned in Chapter 1, the ultimate goal of the solid-state color centers community is to construct the quantum network. Referring to the standards of an ideal spin-photon interface in Chapter 1, I outlook the possible works based on this thesis toward building up better spin-photon interfaces based on the GeV^- center in diamond and the $N_CV_{Si}^-$ centers in SiC. In detail:

In section 6.2.1, I stress the importance of learning other charge states of the GeV center in diamond and the $N_CV_{Si}^-$ centers in SiC. The observation of the quenched emission is attributed to another charge state of GeV^- centers. It also has been reported that (1) the neutral charge

state of SiV centers exhibits near IR emission, (2) NV^- centers in diamond and VV^0 centers in SiC would be pumped into other charge states. Thus, it is essential to look into the performance of other charge states of GeV and NV centers and the charge-state conversion mechanism among different charge states.

In Chapter 2, I highlighted the importance of knowing of color centers' energy structures and presented associated methods to characterize their structures. I observed different photoluminescence excitation spectra of axial and basal $N_CV_{Si}^-$ centers in the experiment. Thus, it is essential to delve into this difference by studying the energy levels of $N_CV_{Si}^-$ centers. However, single $N_CV_{Si}^-$ centers exhibit weak emission, preventing them from doing the resonant excitation and applying them into quantum applications. Hence, I highlight the approaches to enhance the emission of single $N_CV_{Si}^-$ centers by integrating them into nanostructures.

In the end, I outlook two schemes to realize the spin-photon entanglement.

6.2.1 Charge state study

6.2.1.1 Neutral germanium vacancy in diamond

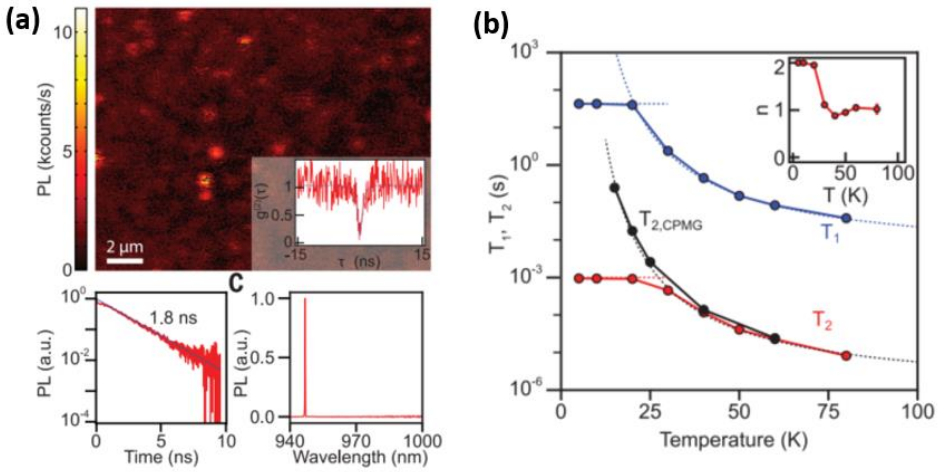

Figure 6.1: Optical and spin properties of SiV^0 centers in diamond. (a) Optical properties of a single SiV^0 center in diamond (The emission wavelength at 946 nm; the lifetime is 1.8 ns). (b) The spin lifetime and spin coherence time[1]. Reproduced with permission [1]. Copyright 2018, American Association for the Advancement of Science.

It has been pointed out that a good platform should have emission compatible with the current fiber work. Regarding SiV^- centers in diamond, its emission is at 738 nm. To convert the visible photon into an infrared region, people used a nonlinear PPLN crystal[2]. In return, this renders a less compact system. Fortunately, several groups find that the neutral state of SiV (SiV^0) is

also bright [1, 3-7]. The SiV^0 centers show emission near 946 nm (Figure 6.1(a)), giving less optical loss than the SiV^- centers. **More importantly, the SiV^0 state has a non-zero ground state spin splitting, providing a direct spin-photon interface. The ground state spin could be polarized under the resonant or off-resonant excitation**. This system shows a long spin-relaxation time and spin coherence time. Figure 6.1(b) shows that the T_1 and T_2 are independent of temperature when the sample temperature is less than 20 K. The T_1 is about 43 s, and the T_2 is about 1 ms. The T_2 could be prolonged to 255 ms at 15 K with CPMG pulses.

Similarly, it is tempting to study if the dark state of GeV in Chapter 3 is another charge state. There are few reports on the GeV^0 centers. One group reported the formation of GeV^0 centers with electrical control[8]. Another group has reported the observation of GeV^0 centers in diamond with EPR experiments[9]. However, there is no report on the optical and spin properties of the GeV^0 center. The difficulty for the study on GeV^0 lies in the formation of this defect.

The general methods to tune the charge state of color centers rely on the Femi-level tunning by terminating the sample surface with Hydrogen or Oxygen ions if the color center is near the surface[10, 11], by n- or p-type doping of the host with proper doses[12], and by constructing PIN, NIN,[13] and Schottky junctions[14]. In chapter 3, the dark state is believed to be another charge state of GeV centers. Hence, our experiment provided an approach to control the charge state. It is interesting to verify whether the dark state exhibits emission and if it is a paramagnetic defect. If the dark state is optically active and is a paramagnetic defect, it is interesting to look into its optical and spin properties. The next question is if it is possible to control the charge state with electrical fields. Even though a weak off-resonant laser is employed to avoid the off-resonant excitation of GeV^- centers, there is still a chance to excite them during a long exposure. Alternatively, one could use PIN junctions to control the charge state.

Besides the nature of the dark state, it is still important to investigate time-dependent emission behavior of the GeV^- centers. A good candidate for the quantum network should exhibit narrow emission linewidth and stable emission wavelength. In this context, it is essential to answer if the presence of a dark state would affect the emission stability of the GeV^- centers.

6.2.1.2 N_CV_{Si} centers charge-state competition

It has been widely observed that the charge-state conversion upon laser illumination in diamond N_CV_{Si} system ($N_CV_{Si}^0$ and $N_CV_{Si}^-$) and SiC divacancy system (VV^- and VV^0)[15]. **This charge**

state instability will be detrimental for quantum applications. It is yet known the charge-state dynamics in the SiC N_CV_{Si} system. Hence, it is of vital importance to look into the SiC N_CV_{Si} centers' charge state with the help of tools like EPR[15].

6.2.2 Energy levels of sing $N_CV_{Si}^-$ centers in SiC

N_CV_{Si} centers, as an emerging family of the spin-photon interfaces, still wait for detailed study. As a start, it is necessary to figure out their exact energy structures. The energy levels of SiC $N_CV_{Si}^-$ centers should share some similarities with that of diamond $N_CV_{Si}^-$ centers (shown in Figure 6.2). Nevertheless, what matters to us is their difference. As shown in Figure 6.2(a), the on-axis $N_CV_{Si}^-$ centers have a C_{3v} symmetry, the same as the diamond $N_CV_{Si}^-$; while the off-axis $N_CV_{Si}^-$ centers have a lowered symmetry of C_{1h}, resulting in the lifted degeneracy of the orbital states. In Chapter 5, I observed double absorption peaks for off-axis defects but single peaks for on-axis defects. These observations agree with the electron configurations shown in Figure 6.2. The a" orbit should be far away from the a' orbit for off-axis defects.

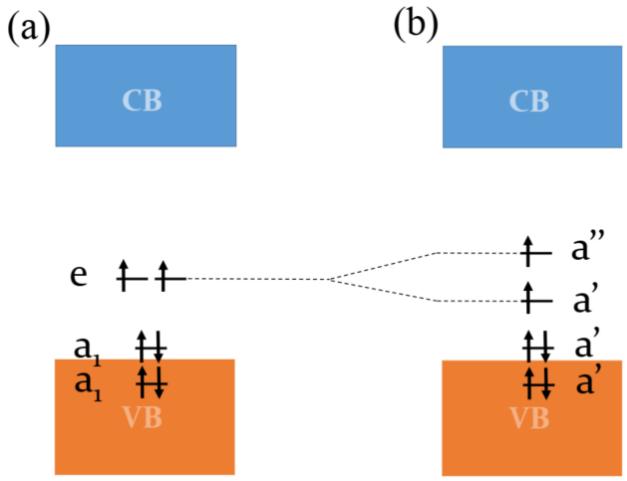

Figure 6.2: Ground state electron configuration of (a) on-axis $N_CV_{Si}^-$ centers and (b) off-axis $N_CV_{Si}^-$ centers[16] in SiC. Reproduced with permission [16]. Copyright 2018, American Physical Society.

To design an applicable scheme for spin-photon entanglement, it is necessary to know the transition rules. The resonant excitation was performed on ensemble $N_CV_{Si}^-$ centers in Chapter 5. Due to homogeneous and inhomogeneous linewidth broadening, it prevented us from resolving the fine structure of the $N_CV_{Si}^-$ centers and the linewidth of each transition. It thus demands study of optical and spin properties of single $N_CV_{Si}^-$ centers in SiC. **However, one technical barrier that prevents the single $N_CV_{Si}^-$ centers study is their low emission count rates.** In the next section, I will discuss several nanostructures to enhance the $N_CV_{Si}^-$ centers' emission.

6.2.3 On the origin of the Ge-related color centers in diamond and their spectral jumps

In chapter 4, I reported the binary spectral jump of color centers in diamond. The investigated defects is thought to be Ge-related since these defects are observed after Ge ion implantations. However, their exact origin and their atomic configuration are still unknown. It is also unclear why there is a spectral jump. To answer these two questions: (1) the origin of the investigated defects; (2) the mechanism of the binary spectral jump, the following experiments are necessary.

As explained in Chapter 2, resonant excitation is always helpful for probing the energy structures. The spectral jump rates of Ge-related defects are comparatively low when the off-resonant laser power is less than 0.2 mW. The resonant excitation, compared to the off-resonant excitation, is more efficient for color centers (Chapter 3). If the spectral jump rates are determined by the power of the excitation laser but the wavelength of the laser, there is a chance to perform the resonant excitation with one state of the color centers. Knowing the energy structures of the defects could provide necessary information for the ab-initio calculations. Hence, the origin of these two states could be determined. It is also important to explain why these two states exhibit different emission counts. It is essential to measure the two states' excitation and emission polarization dependence to understand this. Based on this knowledge of the color centers, the spectral jump behavior of the color centers could be treated by considering different models, e.g., the emission intermittency in QDs[17].

6.2.4 Integration of a single $N_CV_{Si}^-$ center into SiC nanostructures

Many demonstrations of quantum applications like QKD operate at the megahertz range[18]. This is partially limited by the brightness of the SPSs, which can be enhanced by engineering their environment. Moreover, the long-term goal of quantum internet demands SPSs, which are integrable to photonic integrated circuits[19-21]. In this regard, people have demonstrated the integration of SPSs into various nanostructures. Regarding the single $N_CV_{Si}^-$ centers in SiC, its weak emission prevents further studies like fine structure characterization and spin photon entanglement. Considering that the emissions from SiC $N_CV_{Si}^-$ centers are quite broad at room temperature while they are narrower at low temperature, nanostructures like nanopillars[22], solid immersion lens (SIL)[23], and gratings[24], are used for room temperature applications. In contrast, cavities are used at low temperatures [25, 26]. In the following, I will show the successful combination of SPEs (experience not limited to diamond or SiC systems) and nanostructures.

6.2.5.1 SILs and nanopillars

Both SIL and nanopillars are widely used in color centers communities. Due to the reflection and refraction at the interface between the crystal host and the objective medium, only a portion of photons could be collected by the objective. Similarly, when optical excitation is used, the light from the objective cannot couple effectively to the emitter[22, 23]. SIL and nanopillar can mitigate this problem resulting in enhanced collection and excitation efficiency.

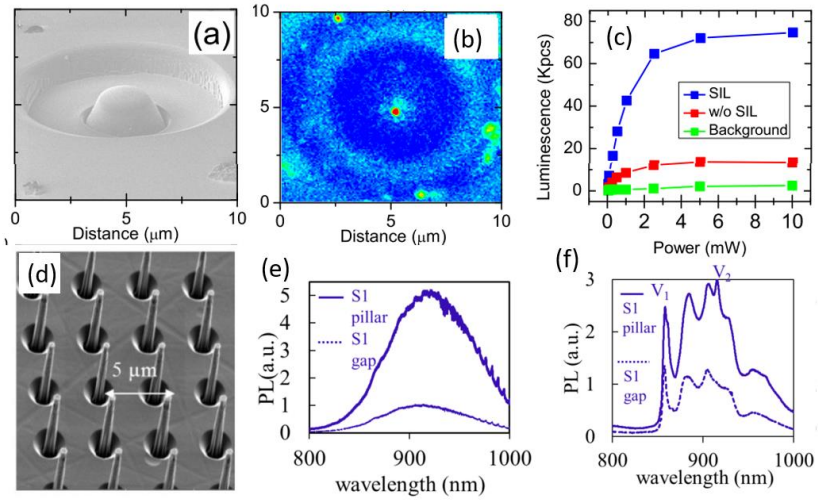

Figure 6.3: Color centers incorporated into SILs and nanopillars. (a) An SEM image of a diamond SIL. (b) A 2-dimensional confocal scanning of the SIL in (a). (c) Emission saturation curves of an NV^- center within the diamond SIL and outside the SIL. (d) An SEM image of an array of SiC nanopillars. Room (e) and cryogenic (f) temperature PL spectra of V_{Si}^- emitters in a pillar and the gap of the pillars. (a-c)[27]Reproduced with permission [27]. Copyright 2011, AIP publishing. (e-f)[22] Reproduced with permission [22]. Copyright 2019, The Authors, published by Beilstein Institute for the Advancement of Chemical Sciences.

Figure 6.3(a) shows the SEM image of a diamond SIL[27]. SPEs can be generated in the diamond by ion implantation along with high-temperature annealing. Several emitters are scattered around the SIL, and the emission count in the SIL is the highest. The saturation count in the SIL is about 8 times greater than emitters outside of the SIL.

Nanopillars, by comparison, are reported to give higher enhancement factors. Castelletto reported the emission of V_{Si}^- centers being enhanced by 20 times[22]. The authors first determined the proper parameters of nanopillars. The nanopillars are developed accordingly with ICP etching (Figure 6.3(d)). The enhancement effect is apparent at both room and cryogenic temperature according to the emission spectra (Figure 6.3(e) and 6.3(f)).

6.2.5.2 Cavities

Emitters like SiC VV^0, $N_CV_{Si}^-$, and rare-earth ions are potential testbed of spin-photon entanglement. For this application, not only a high count rate emission is required, but also a high ZPL ratio is preferred[28, 29]. In this regard, these systems are often cooled down to cryogenic temperature and are integrated into cavities such as micro-rings[25, 30] and nano-beams (Figure 6.4(a))[26], with nanobeam having a smaller effective mode volume.

Nanobeam cavities have been employed to enhance the VV^0 center emission[26]. They found that the collection efficiency is enhanced by 2-3 times while the Purcell factor of 50 is achieved. Moreover, the ZPL ratio increases from 5% to 70-75%. As shown in Figure 6.4(b), the ZPL of VV^0 centers is barely visible when there is no enhancement. It turns out to be a sharp and strong peak when the cavity is tuned to resonate with the VV^0 emission. **This achievement may pave the way toward the realization of spin-photon entanglement with SiC VV^0s.**

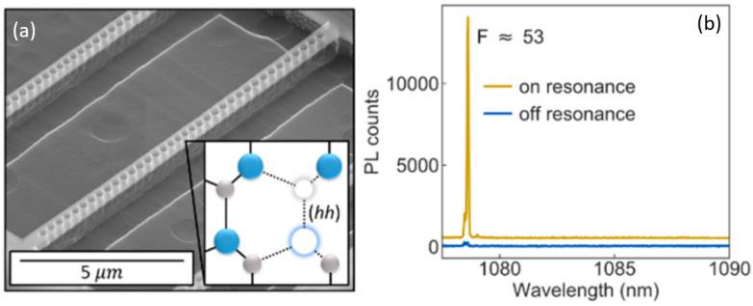

Figure 6.4: (a) Single VV^0 center embedded into nanobeam cavity. (b) Single VV^0 center emission spectra when VV^0 center is on resonance (yellow) or off-resonance (blue) with the cavity mode[26]. Reproduced with permission [26]. Copyright 2020, American Chemical Society.

6.2.5 Spin-photon entanglement

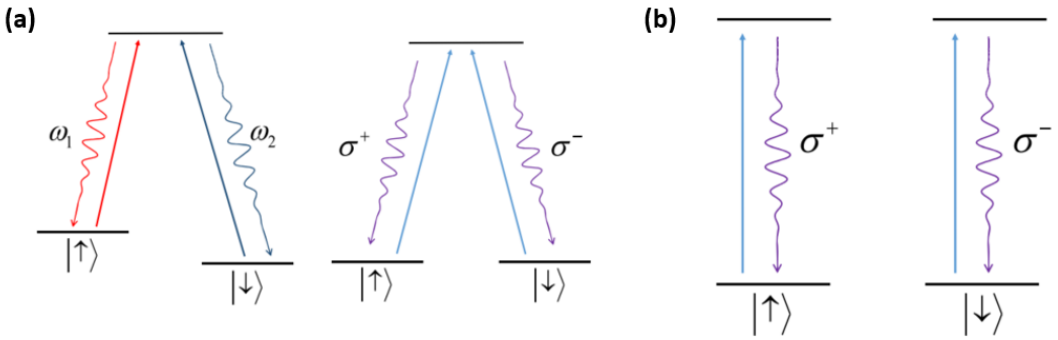

Figure 6.5: Entanglement scheme for (a) Λ and (b) II systems [31]. Reproduced with permission [31]. Copyright 2016, IOP Publishing.

The spin-photon interface is one of the most important benefits of using color centers in wide-bandgap materials for quantum internet applications. The realization of spin-photon entanglement is a vital experiment to demonstrate this advantage. People have realized spin-photon entanglement with diamond NV^- and quantum dots systems [29, 32, 33]. Apart from these two, people also show strong interest in silicon carbide defects, including V_{Si}^-, VV^0, and $N_CV_{Si}^-$ centers. Two schemes have been proposed to realize spin-photon entanglement[31]. To implement these schemes, one should first answer the following question: energy level structure, selection rules, and the ability to generate superpositions of excited states).

(a) Λ-scheme. Given the similar energy structure between diamond NV^- and SiC $N_CV_{Si}^-$ centers systems, it is natural to try the same spin-photon entanglement protocol demonstrated with the diamond NV^- centers system[31]. One aspect which should be taken care of is the crystal strain[31]. Depending on the sample strain, spins could be entangled with photons' polarization or frequency of freedom (Figure 6.5(a)).

(b) II-scheme. When defects are situated in a low-strain environment, the energy levels show degeneracy in both the ground and excited state (Figure 6.5(b)) for the SiC $N_CV_{Si}^-$ centers system[31]. In this case, the spins can only be entangled with the polarization of the photons.

Regarding GeV^- centers in diamond, it is also possible to construct Λ-systems by applying an external magnetic field[34]. However, the detailed scheme requires an understanding of the role of strains.

References

[1] ROSE B C, HUANG D, ZHANG Z-H, et al. Observation of an environmentally insensitive solid-state spin defect in diamond [J]. Science, 2018, 361(6397): 60-3.

[2] TCHEBOTAREVA A, HERMANS S L N, HUMPHREYS P C, et al. Entanglement between a Diamond Spin Qubit and a Photonic Time-Bin Qubit at Telecom Wavelength [J]. Phys Rev Lett, 2019, 123(6): 063601.

[3] ZHANG Z H, STEVENSON P, THIERING G, et al. Optically Detected Magnetic Resonance in Neutral Silicon Vacancy Centers in Diamond via Bound Exciton States [J]. Phys Rev Lett, 2020, 125(23): 237402.

[4] MOLIVER S S. Electronic structure of neutral silicon-vacancy complex in diamond [J]. Technical Physics, 2003, 48(11): 1449-53.

[5] GREEN B L, MOTTISHAW S, BREEZE B G, et al. Neutral Silicon-Vacancy Center in Diamond: Spin Polarization and Lifetimes [J]. Phys Rev Lett, 2017, 119(9): 096402.

[6] GREEN B L, DOHERTY M W, NAKO E, et al. Electronic structure of the neutral silicon-vacancy center in diamond [J]. Physical Review B, 2019, 99(16).

[7] BRAY K, FEDYANIN D Y, KHRAMTSOV I A, et al. Electrical excitation and charge-state conversion of silicon vacancy color centers in single-crystal diamond membranes [J]. Applied Physics Letters, 2020, 116(10).

[8] KRIVOBOK V S, EKIMOV E A, LYAPIN S G, et al. Observation of a 1.979-eV spectral line of a germanium-related color center in microdiamonds and nanodiamonds [J]. Physical Review B, 2020, 101(14): 144103.

[9] KOMAROVSKIKH A, UVAROV M, NADOLINNY V, et al. Spin Relaxation of the Neutral Germanium-Vacancy Center in Diamond [J]. physica status solidi (a), 2018, 215(22).

[10] HAUF M V, GROTZ B, NAYDENOV B, et al. Chemical control of the charge state of nitrogen-vacancy centers in diamond [J]. Physical Review B, 2011, 83(8).

[11] GROTZ B, HAUF M V, DANKERL M, et al. Charge state manipulation of qubits in diamond [J]. Nat Commun, 2012, 3: 729.

[12] GALI Á. Ab initio theory of the nitrogen-vacancy center in diamond [J]. Nanophotonics, 2019, 8(11): 1907-43.

[13] MAKINO T, KATO H, SHIMIZU M, et al. Chapter Five - Charge state control by band engineering [M]//NEBEL C E, AHARONOVICH I, MIZUOCHI N, et al. Semiconductors and Semimetals. Elsevier. 2020: 137-59.

[14] SCHREYVOGEL C, POLYAKOV V, WUNDERLICH R, et al. Active charge state control of single NV centres in diamond by in-plane Al-Schottky junctions [J]. Sci Rep, 2015, 5: 12160.

[15] WOLFOWICZ G, ANDERSON C P, YEATS A L, et al. Optical charge state control of spin defects in 4H-SiC [J]. Nat Commun, 2017, 8(1): 1876.

[16] CSóRé A, VON BARDELEBEN H J, CANTIN J L, et al. Characterization and formation of NV centers in 3C, 4H, and 6H SiC: An ab initio study [J]. Physical Review B, 2017, 96(8).

[17] FRANTSUZOV P, KUNO M, JANKó B, et al. Universal emission intermittency in quantum dots, nanorods and nanowires [J]. Nature Physics, 2008, 4(7): 519-22.

[18] YUAN Z, PLEWS A, TAKAHASHI R, et al. 10-Mb/s Quantum Key Distribution [J]. Journal of Lightwave Technology, 2018, 36(16): 3427-33.

[19] BOGAERTS W, PEREZ D, CAPMANY J, et al. Programmable photonic circuits [J]. Nature, 2020, 586(7828): 207-16.

[20] LUKIN D M, GUIDRY M A, VUČKOVIĆ J. Integrated Quantum Photonics with Silicon Carbide: Challenges and Prospects [J]. PRX Quantum, 2020, 1(2).

[21] WAN N H, LU T J, CHEN K C, et al. Large-scale integration of artificial atoms in hybrid photonic circuits [J]. Nature, 2020, 583(7815): 226-31.

[22] CASTELLETTO S, AL ATEM A S, INAM F A, et al. Deterministic placement of ultra-bright near-infrared color centers in arrays of silicon carbide micropillars [J]. Beilstein J Nanotechnol, 2019, 10: 2383-95.

[23] SARDI F, KORNHER T, WIDMANN M, et al. Scalable production of solid-immersion lenses for quantum emitters in silicon carbide [J]. Applied Physics Letters, 2020, 117(2).

[24] LI L, CHEN E H, ZHENG J, et al. Efficient Photon Collection from a Nitrogen Vacancy Center in a Circular Bullseye Grating [J]. Nano Letters, 2015, 15(3): 1493-7.
[25] SONG B-S, ASANO T, JEON S, et al. Ultrahigh-Q photonic crystal nanocavities based on 4H silicon carbide [J]. Optica, 2019, 6(8).
[26] CROOK A L, ANDERSON C P, MIAO K C, et al. Purcell Enhancement of a Single Silicon Carbide Color Center with Coherent Spin Control [J]. Nano Lett, 2020, 20(5): 3427-34.
[27] MARSEGLIA L, HADDEN J P, STANLEY-CLARKE A C, et al. Nanofabricated solid immersion lenses registered to single emitters in diamond [J]. Applied Physics Letters, 2011, 98(13): 133107.
[28] TOGAN E, CHU Y, TRIFONOV A S, et al. Quantum entanglement between an optical photon and a solid-state spin qubit [J]. Nature, 2010, 466(7307): 730-4.
[29] GAO W B, FALLAHI P, TOGAN E, et al. Observation of entanglement between a quantum dot spin and a single photon [J]. Nature, 2012, 491(7424): 426-30.
[30] LUKIN D M, DORY C, GUIDRY M A, et al. 4H-silicon-carbide-on-insulator for integrated quantum and nonlinear photonics [J]. Nature Photonics, 2019, 14(5): 330-4.
[31] ECONOMOU S E, DEV P. Spin-photon entanglement interfaces in silicon carbide defect centers [J]. Nanotechnology, 2016, 27(50): 504001.
[32] TOGAN E, CHU Y, TRIFONOV A S, et al. Quantum entanglement between an optical photon and a solid-state spin qubit [J]. Nature, 2010, 466(7307): 730-4.
[33] DE GREVE K, YU L, MCMAHON P L, et al. Quantum-dot spin-photon entanglement via frequency downconversion to telecom wavelength [J]. Nature, 2012, 491(7424): 421-5.
[34] SIYUSHEV P, METSCH M H, IJAZ A, et al. Optical and microwave control of germanium-vacancy center spins in diamond [J]. Physical Review B, 2017, 96(8).

Appendix A Supporting materials for Chapter 3

A1: SATURATION UNDER OFFRESONANT AND RESONANT EXCITATION

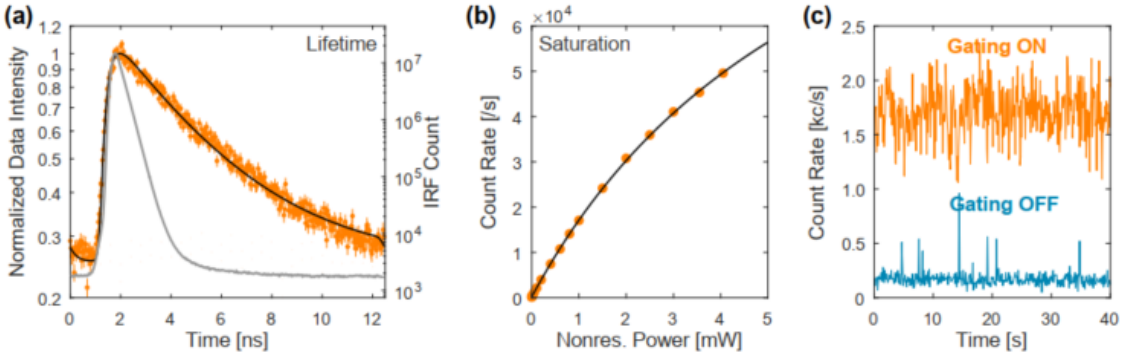

Figure A1[1]: (a) Time-resolved PL of the GeV$^-$ center at 5 K under picosecond-pulse excitation, plotted in semi-logarithmic scale. Orange dots are the raw data with the error bar representing shot-noise. The Grey curve is the IRF of the experimental setup. The black line is a fitting with an exponential decay after convolving with the IRF. (b) Non-resonant power dependence of PL at 5 K under 532 nm excitation. Orange dots are the raw data with the error bar reflecting statistical fluctuation of the count rate over ~2 mins. Solid purple curve is a fitting by using the conventional saturation function. (c) Resonance fluorescence intensity of transition D with gating on (orange) and gating off (blue). Resonant power: 200 nW (0.35 P_0); Non-resonant power: 20 nW (3 × 10-6 P_1); Binsize: 100 ms. No background subtraction. Reproduced with permission [1]. Copyright 2019, American Physical Society.

Lifetime T_1

The lifetime of the GeV$^-$ center is determined by time-resolved PL measurement, as shown in Figure A1(a). A train of 512-nm 80-ps pulses at a repetition rate of 80 MHz (from PiL051X) is focused onto the GeV$^-$ center. Zero-phonon line (ZPL) emission from the GeV$^-$ center is collected by using a combination of a 600 ± 7 nm band-pass and a 600 nm long-pass edge filter. The data is fitted with a single exponential decay convolving with the measured instrument response function (IRF, grey curve) of the setup, from which we determine the lifetime of the GeV$^-$ center to be T_1 = 3.57 ± 0:03 ns.

Non-resonant saturation power P_1

By fitting the power-dependent PL with a conventional saturation function, $I \propto P/(P+P_1)$, a non-resonant saturation power (at 532 nm) of P_1 = 6.8 ± 0.2 mW is extracted, as shown in Figure A1(b).

Gating of resonance fluorescence of transition D

The gating effect can also be demonstrated on transition D of the GeV^- center as shown in Figure A1(c). The PL intensity is enhanced by 200 times when switching on the gating laser (after background correction). The enhancement factor achieved here is 2.5 times lower than the value reported in the Chapter 3, mainly due to the lower gating power employed here.

Resonant saturation power P_0

To pinpoint the resonant saturation power P_0, we employ a pulsed measurement scheme to recover the saturation behavior of PL, as shown in Figure A2(a) and (b). In this experiment, the resonant beam is modulated by an acousto-optic modulator (AOM), while the non-resonant beam is kept in continuous-wave (CW) mode and held at constant power. The dwell time between two consecutive resonant pulses is chosen to be a few milli-seconds such that the GeV center can always relax back to the same equilibrium state for different resonant powers. We only select the PL counts within the transient window upon the arrival of excitation pulses, as indicated by the shaded grey area in Figure A2(a), for data analysis. Again, fitting the data with a conventional saturation function, we extract a resonant saturation power of $P_0 = 1.15 \pm 0.3$ μW, as shown in Figure A2(b).

IRF of acousto-optic modulator

Acousto-optic modulators (AOMs) were employed for dynamics investigations as shown in Figure 3.4 of the Chapter 3. and the characterization of resonant saturation power as shown in Figure. A2(a). The rise/fall time of AOMs is as short as 10 ns, as shown in Figure. A2(c), which is three orders of magnitude shorter than the characteristic time of the dynamics shown in Figure. 4 of the Chapter 3. But, it is still too slow to resolve the Rabi oscillations in Figure 3.2(d) of the Chapter 3. Instead, we employed a fast Mach-Zehnder-interferometer-based electro-optic modulator (EOM) to study this coherent phenomenon. Our EOM has a typical response time of ∼200 ps.

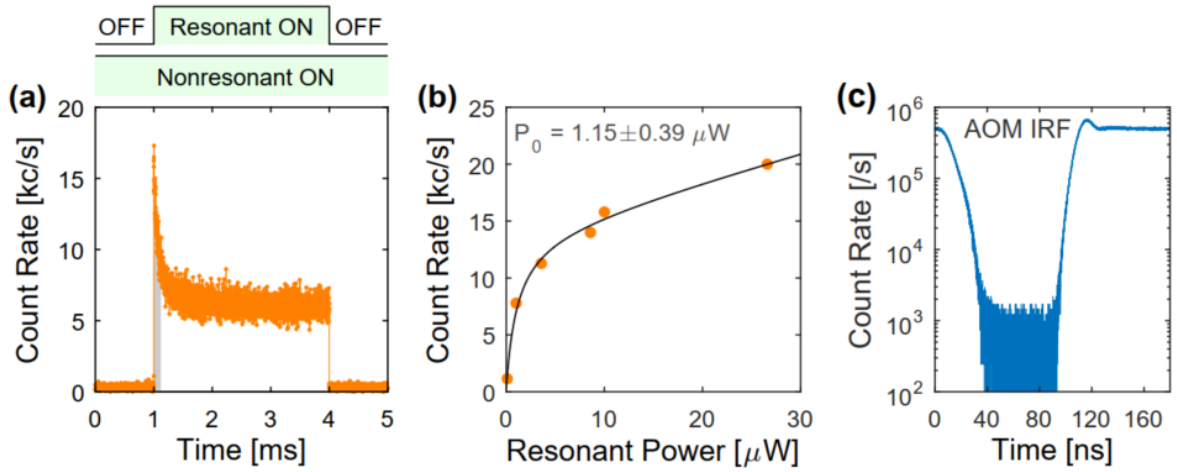

Figure A2[1]: (a) Time-dependent PL when modulating resonant laser while keeping the non-resonant laser in CW mode. The shaded grey region corresponds to the time window within which the effect of resonant pumping is negligible. Top panel: modulation protocol. Resonant power: 8.7 P_0. Non-resonant power: 7.4 × 10-5 P_1. (b) Saturation behavior of the PL. Orange dots are the extracted maximum intensities in (a). The black curve is a fitting by using the conventional saturation function: IPL = A×P/(P+P_0) + B×P+C. where the second term is the linear laser scattering and the last term corresponds to the background. Fitting parameters: A = 13.9±2.0 kHz; B = 0.24 ±0.10 kHz; and C = 0.29 kHz. (c) IRF of an AOM used for dynamics study, characterized at 532 nm. Reproduced with permission [1]. Copyright 2019, American Physical Society.

A2: MODEL - RABI OSCILLATIONS & DARK-STATE DYNAMICS

When resonantly pumping a 2-level system, the population in the excited state oscillates (known as Rabi oscillations) as a result of competition between resonant pumping (absorption) and stimulated emission. In reality, this coherent process is continuously disrupted by various dephasing mechanisms, such as spontaneous decay and phonon interaction, leading to damping of oscillations over a period of coherence time T_2 which defines the robustness of the coherence within ground-excited states manifold. Experimentally, one can investigate this coherent phenomenon by taking advantage of spontaneous decay to map the oscillatory population onto the PL intensity, providing an accurate timing of excitation pulses, which is usually realized with the help of an EOM. A 2-level system formulated in a semiclassical framework is accurate enough for a theoretical description of the oscillations. Time evolution of the system is dictated by the master equation, where spontaneous decay and pure dephasing are incorporated in Lindblad terms[2]

$$\frac{d}{dt}\begin{pmatrix}\rho_G\\ \rho_E\\ \rho_{GE}\\ \rho_{EG}\end{pmatrix}=\begin{pmatrix}-k_{GD} & \Gamma_{sp} & i\Omega/2 & -i\Omega/2 & k_{DG}\\ 0 & -\Gamma_{sp}-k_{ED} & -i\Omega/2 & i\Omega/2 & \rho_G\\ i\Omega/2 & -i\Omega/2 & -1/T_2 & 0 & 0\\ -i\Omega/2 & i\Omega/2 & 0 & -1/T_2 & 0\end{pmatrix}\begin{pmatrix}\rho_G\\ \rho_E\\ \rho_{GE}\\ \rho_{EG}\end{pmatrix} \qquad (A-1)$$

where ρ_G, ρ_E are the time-dependent population in the ground and excited state, ρ_{GE} and ρ_{EG} are the coherence between G and E, $\boldsymbol{\Omega}$ is the resonant Rabi frequency, Γsp is the spontaneous decay rate, and T_2 is the coherence time of the excited state. The time-dependent PL intensity is proportional to $\rho_E(t)\Gamma_{sp}$ to a constant that describes the efficiency of the entire system, including the quantum yield of the GeV^- center[3]. By solving Eqn. A1 numerically, we simultaneously fit multiple oscillations measured at different excitation powers to pinpoint a coherence time of $T_2 = 366 \pm 20$ ps. The extracted Rabi frequencies follow a linear dependence with respect to the square root of excitation power, as shown by the inset of Figure 3.2d in the Chapter 3. The success of the 2-level model indicates that within the short period of an excitation pulse, the population dynamics involving the dark-state is not important, which is in fact consistent with the main finds of the Chapter 3, i.e., dark-state dynamics is significantly slower compared to the spontaneous decay.

For CW excitation, the PL intensity is proportional to the steady-state population in the excited state

$$I_{PL} \propto \rho_E^{2-level} = \frac{1}{2}\frac{\Omega^2\Upsilon/\Gamma_{sp}}{\Delta\omega^2+\Upsilon^2+\Omega^{2\Upsilon}/\Gamma_{sp}} \qquad (A-2)$$

where $\Delta\omega$ is the excitation detuning, and $\gamma = 1/T_2$ is the dephasing rate of the excited state. By comparing Eqn. A2 to the conventional saturation function, i.e., $I_{PL} \propto P/(P + P_0)$, where P_0 denotes the resonant saturation power, we establish a connection between excitation power P and Rabi frequency Ω

$$\Omega = \sqrt{\Upsilon\Gamma_{sp}\frac{P}{P_0}} \qquad (A-3)$$

For the studies presented in Figure 3.4 of the Chapter 3, dark-state dynamics is directly measured and a 3-level model is needed for a complete description of the system. We formulate the model in a semiclassical picture to incorporate the coherent effect under resonant excitation. Besides the transition GE, no other transitions are resonantly pumped, rendering vanishing Rabi frequencies for all other states, i.e., zero off-diagonal elements for the block matrix spanned by elements ρ_{ED}, ρ_{GD}, and their associated complex conjugates. In other words, these

matrix elements are irrelevant to the solution of $\rho_E(t)$, and we can safely drop them when solving for $\rho_E(t)$. This leads us to the differential equation of Eqn.(A1) in the Chapter 3. Steady-state solution gives

$$\rho_E^{3-level} = \frac{1}{2}\frac{k_{DG}}{k_{DG}+k_{GD}}\left[\frac{(\Delta\omega^2+\Upsilon^2)\left(k_{ED}+\Gamma_{sp}\right)}{\Omega^2\Upsilon}+\frac{1}{2}\left(1+\frac{k_{ED}+k_{DG}}{k_{DG}+k_{GD}}\right)\right]^{-1} \qquad (A-4)$$

where k_{ED}, k_{GD}, and k_{DG} are the population transfer rates from excited to the dark, ground to dark, and dark to ground, respectively. In fact, Eqn. A2 is a special case of Eqn. A4 by setting k_{ED} and k_{GD} to zero. The resonant-power dependence of $k_{\alpha\beta}$ is responsible for the drop of RF at high power regime as shown in Figure.3.3d of the Chapter 3. Lacking of the knowledge on functional of power dependence prevents us from meaningfully fitting the measured intensity with Eqn. A4.

By solving for a detuning from Eqn. A4 for the half of maximum excited population, we find the full-width half maximum (FWHM) of excitation spectra (in linear frequency)

$$\Delta\nu = \frac{1}{\pi T_2}\sqrt{1+\frac{\Omega^2 T_2}{2\left(\Gamma_{sp}+k_{ED}\right)}\left(1+\frac{k_{ED}+k_{DG}}{k_{DG}+k_{GD}}\right)} \qquad (A-5)$$

which is Eqn. (2) in the Chapter 3. Again, without knowing the power dependence of $k_{\alpha\beta}$, it is impossible to quantitatively examine the linewidth in Figure 3.3. Nevertheless, we can still extract the coherence time T_2 by extrapolating the linewidth in Figure 3.3c to zero excitation power. In this limit, Eqn. S5 reduces to $\Delta\nu_0 = 1/(\pi T_2)$, and a coherence time $T_2 = 316 \pm 20$ ps can be obtained.

A3: PLE ANALYSIS

Non-resonant power dependence of PLE linewidth

Mathematically, the PLE linewidth is described by Eqn. A5. Here, we provide a physical explanation of linewidth broadening observed in the low gating power regime as shown in Figure 3.3g of the Chapter 3. This is caused by the detuning dependence of shelving efficiency of the entire system, which is not only dependent on the shelving/deshelving rates related to the dark state but also relies on the excitation efficiency of the ground-excited state transition. In PLE measurements, the collected PL intensity is proportional to the steady-state population in the excited state (ρ_E), which is determined by two factors: A) resonant excitation efficiency;

and B) the amount of population available for excitation, namely bright population $\rho_B = 1 - \rho_D$, where ρ_D denotes the steady-state population of dark-state. The decrease of the excitation efficiency (Mechanism A) for detuning would lead to a Lorentzian line shape of PLE spectrum only if ρ_B is a constant for all detunings. This is the case for 2-level systems, yet might not be true for a 3-level system involving a dark state.

For low non-resonant power, k_{ED} (induced by resonant laser) dominates over k_{GD} and k_{DG} (induced by nonresonant laser), which allows for an efficient transferring of the population from ρ_E to ρ_D. This population channel maps the detuning dependence of ρ_E onto ρ_D, leading to a greater ρ_D for a smaller detuning. Consequentially, the spectrum experiences a flattening effect and exhibits a wider linewidth as compared to the case of no dark-state involved, as shown by the simulations in Figure A3a and b.

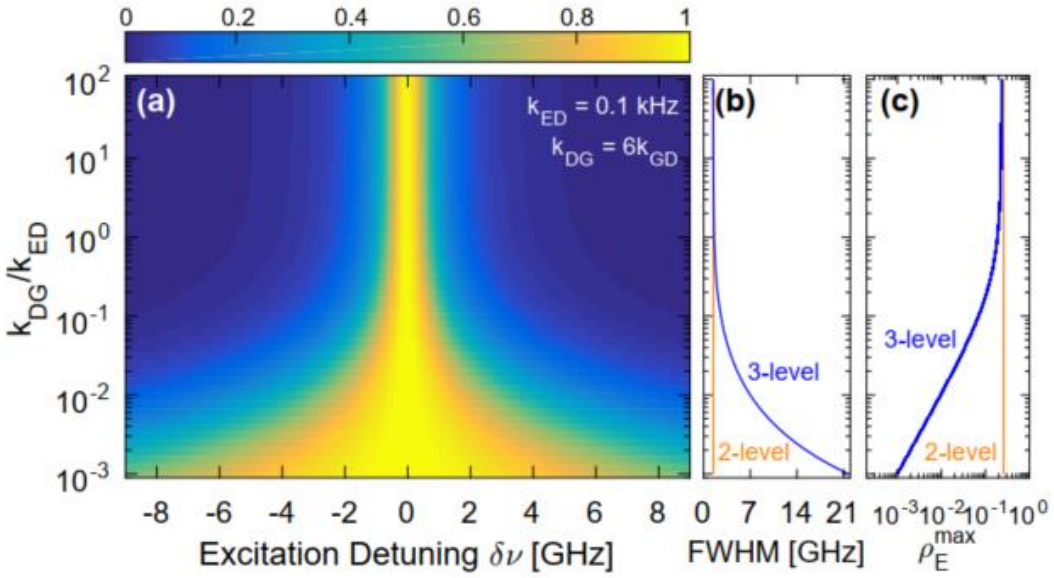

Figure A3[1]: (a) Simulated PLE spectra (normalized) by using Eqn. A4 with parameters determined by experiment (see text). The positive direction of Y-axis corresponds to the increase of non-resonant power. (b) Calculated full width at half maximum (FWHM) of a 3-level system (blue), and a 2-level system (orange), based on Eqn. A5 and Eqn. A2, respectively. (c) Calculated maximum population ρ_E (at zero-detuning) for a 3-level system (blue), and a 2-level system (orange). The blue curve serves as normalization constants to acquire (a). Reproduced with permission [1]. Copyright 2019, American Physical Society.

The situation is different for a high gating power. In this scenario, rates k_{DG} and k_{GD} are enhanced and dominate the population dynamics of the system. The steady-state population in dark state ρ_D is determined by ground state population ρ_G to a proportional factor relying on the ratio of k_{DG} and k_{GD}. Since $k_{DG}/k_{GD} \sim 6$ [see Figure 3.4(d) ofthe Chapter 3], only a small portion of the population resides in the dark state. Thereby, the variations of ρ_D caused by

detunings have a limited impact on bright population ρ_B, meaning that the extra reduction factor induced by the dark-state dynamics does not change for different detunings. Consequentially, a Lorentzian line shape should be observed for high gating power, as shown in Figure A3(a). In simulations presented in Figure A3, all parameters take experimentally determined values: Rabi frequency Ω = 1GHz; spontaneous decay rate Γ_{sp} = 280 MHz; dephasing rate γ = 3.61 GHz; k_{ED} = 100 Hz, and $k_{DG} = 6k_{GD}$. The positive direction of y-axis corresponds to the increase of non-resonant power based on the observation in Figure 3.4(d) of the Chapter 3. All PLE spectra in Figure A3(a) are normalized to the individual maximum population at zero-detuning, which is plotted in Figure A3(c). Calculations based on a 2-level system [by using Eqn. A2] are also shown for comparison.

Multiple peaks of transition C

Sometimes, we observe multiple peaks around transition C [see Figure A4(a)], which can be attributed to the emission from nearby GeV^- centers. Different emission energies reflect different strains experienced by GeV centers located at different positions under the SIL. However, the impact of the strain on four optical transitions is different. Previous studies on silicon-vacancy (SiV^-) and GeV^- centers[4-6] show that the strain is expected to have little impact on transition C but significant influence on transition D. Non-zero E_g-symmetric strains (perpendicular to the C_3 symmetry axis of SiV^- or GeV^- center) can enhance the fine structure splittings in both ground- and excited-manifold by pushing away the energy levels from each other in both manifolds. Since the magnitude of the enhancement is similar for both ground and excited states pairs, the absolute shift of each energy level is almost the same. This leads to a significant variation in transition energies for A and D lines while little change for B and C lines. Thereby, the D lines associated with the nearby GeV^- centers are possibly shifted out of the measurement window thanks to the different strains experienced by centers.

Gating at 405 nm

Figure A4(b) shows PLE scans of the original GeV^- center (GeV1) investigated in the Chapter 3 at different gating wavelengths, i.e., 405 nm (purple) and 532 nm (orange). Since the non-resonant power is kept at the same level of 1.3μW for both beams, the number of photons in the 405 nm beam is 76% of those in 532 nm beam, which quantitatively explains the reduction of PLE intensity for 405 nm gating, with a reduction factor of 72%. The consistency

of these two numbers indicates the same gating efficiency for 405 nm light and 532 nm light. In addition, the success of gating at different wavelengths proves that the non-resonant beam must interact with the system incoherently to generate the corresponding shelving and deshelving processes.

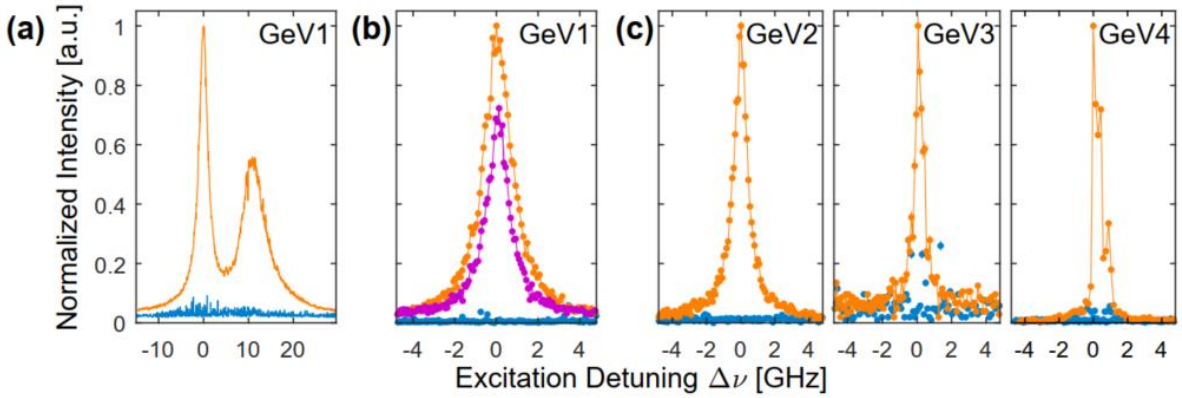

Figure A4[1]: (a) Normalized PLE scan of GeV1 (original GeV^- color center in the Chapter 3) with multiple peaks when gated with 532nm laser (orange). Normalization constant: 8.3×10^3 cnts/s. Zero detunings: 497.754 THz. (b) Normalized PLE scans of GeV1collected at different gating wavelengths, i.e., 532 nm (orange) and 405 nm (purple). Normalization constant: 8.4×10^3 cnts/s. The same figure as the left panel of Figure 3.2(a) in the Chapter 3. (c) Optical switching observed on the other three GeV^- centers. For each emitter, two PLE spectra (normalized) are present with gating on (orange) or off (blue). The gating laser is at 532 nm. Zero detunings corresponds to 497.7686 THz, 497.7585 THz, and 497.9935 THz for GeV2, GeV3, and GeV4, respectively; and the normalization constant is 4.5×10^3, 1.0×10^3, and 9.8×10^3 cnts/s, respectively. All spectra are measured at the same resonant power of 300 nW. Non-resonant power is 1.2±0.1 μW for both 532 nm and 405 nm. Blue trace corresponds to gating off. Reproduced with permission [1]. Copyright 2019, American Physical Society.

Other Germanium-vacancy centers

Optical gating of resonance fluorescence is not limited to GeV1, but a ubiquitous phenomenon that is observable on almost all GeV^- centers investigated so far, which is more than 20 centers from two crystals. Figure A4(c) shows three examples of them. Two PLE spectra are collected for each center with gating on and off. Resonance fluorescence of all three centers is quenched when the gating laser is off (blue trace), which is recovered when the gating laser is on (orange trace). In fact, a similar (RF) blinking phenomenon has been reported on an HPHT diamond, where the GeV^- centers are incorporated into the sample during the growth by using an Mg-Ge-C system[7].

A4: RATE ANALYSIS & POSSIBLE PHYSICAL PROCESS

In the study of the dynamics as shown in Figure 3.4 of the Chapter 3, several parameters in Eqn. (3-1) are fixed to constants to validate the fitting. Some of them are determined by separate measurements, for example, spontaneous decay rate $\Gamma sp = 1/T_1 = 280$ MHz via lifetime measurement, coherence time $T_2 = 316$ ps through linewidth analysis; and Rabi frequency Ω by using Eqn. A3 based on the measured excitation power. At a glance, T_2 should not be a constant, because of the introduction of the extra dephasing channel by the dark sate, the rates of which depend on both resonant and non-resonant powers, as shown in Figure 3.4(d) and (g) of the Chapter 3. However, these dynamics are too slow compared to the dephasing rate $1/T_2$, and can barely influence the latter.

In addition, the overall efficiency η in Eqn. (3-3) is fixed to 9×10^{-5} through the entire fitting analysis. In principle, η consists of two factors following $\eta = \eta_D \times \eta_Q$, where η_D is the overall detection efficiency of the entire experimental setup, and η_Q is the quantum yield of the GeV center. For our system, η_D is found to be ~0.3% by considering collection efficiency of the objective, fiber coupling efficiency, detector efficiency, beam-splitter ratio, optic loss, phononside band (PSB) branching ratio. Quantum yield η_Q is defined as the probability for a photon emission upon a transition from the excited state to the ground state, which is found to be 3% based on an absorption measurement by Boldyrev et al[3]. This number is close to the quantum yield of SiV^- center[8, 9], which is 2~9%.

For the modulation experiment in Figure 3.4(c) of the Chapter 3, the resonant laser is kept in CW mode with a constant power. Since k_{ED} is mainly affected by resonant pumping, this rate must be the same for when varying the nonresonant power. In addition, rates k_{GD}^{off} and k_{DG}^{off} are also set to be shared parameters for different non-resonant powers since the experimental conditions for off-period is the same for the entire experiment. Therefore, we employ a global fitting to determine these three rates, i.e, $k_{ED} = 173 \pm 16$ Hz, $k_{GD}^{off} = 92 \pm 28$ Hz, and $k_{DG}^{off} = 4 \pm 3$ Hz.

Following the same logic, when varying the resonant power as shown in Figure 3.4(f) of the Chapter 3, k_{ED} is expected to be the same only for on- and off-period of each single resonant power, i.e., $k_{ED}^{off} = k_{ED}^{on}$, but different for different resonant powers. Figure A5(a) shows all the extracted rates against the resonant power, including those shown in Figure 3.4(g) of the Chapter 3. Rates k_{GD}^{off} and k_{DG}^{off} show a slight variation over the resonant power, implying that

the resonant laser can also influence the shelving (GD) and deshelving (DG) channels on its own.

Figure A5(b) shows one possible physical picture underpinning the observed shelving and deshelving phenomena. As mentioned in the Chapter 3, the dark state (D) of the GeV^- center is possibly a differently charged species of the center, which depends on the local Fermi level. Here, we temporarily assign it to be a neutral state (GeV^0), considering the low doping level of the sample. Since GeV^0 possesses an energy structure that is different from GeV^-, the RF of the latter quenches when the center resides in the neutral state; the RF recovers when the charge state returns back to negative. This leads to the observed PL intermittency as shown in the inset of Figure 3.2(c) of the Chapter 3.

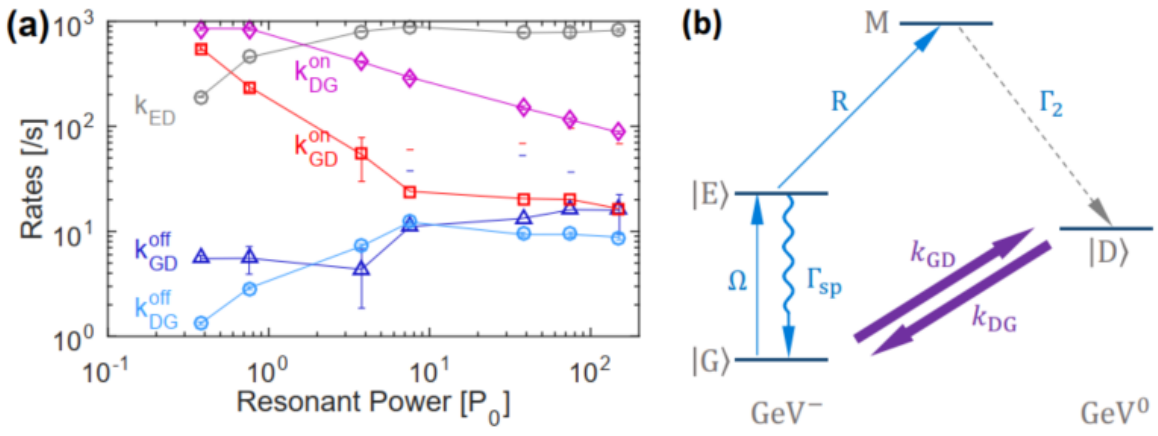

Figure A5[1]: Possible physical mechanism giving rise to the gating and shelving effects. States G, E, D, and M represent the ground, excited, dark, and meta-stable states of GeV center, respectively. k_{GD} is the transition rate from the ground state of GeV^- to the dark state (GeV^0) via losing an electron, and k_{DG} is the opposite process via losing a hole. **Ω** is Rabi frequency. sp is the spontaneous decay rate of the excited state. R represents a population pumping channel from the excited state to the metastable state M, which is active with a 602 nm laser. The population residing in M would relax to dark state D via non-radiative decay at rate Γ2. Reproduced with permission [1]. Copyright 2019, American Physical Society.

It is possible to stabilize the RF intensity by employing a weak non-resonant laser. This light produces a free-charge carrier bath around the GeV^- center by interacting with the local defects or impurities. These charge carriers modify the local Fermi level[10], and influence the charge dynamics of the emitter. Generally, a stronger non-resonant power corresponds to a higher charge-carrier density, thus promoting the speed of rates k_{GD} and k_{DG}, as shown by Figure 3.4(d) of the Chapter 3. Resonant laser, on the other hand, can shelve the population into the dark-state D via a meta-stable state M, as shown in Figure A5(b). The power-dependent

pumping rate R is responsible for the enhancement of k_{ED} for low resonant power, while the constant non-radiative relaxation rate from M to D accounts for the saturation behavior of k_{ED} for large excitation power, as shown in Figure A5(a).

When the center is solely pumped by a resonant laser, the most population would be shelved into the dark state, resulting in the quenching of RF. However, the slight background doping of the sample provides the charge carriers to momentarily set the emitter back to GeV^- state through k_{DG} channel, resulting in the short bursts of RF as observed in Figure 3.2(b) of the Chapter 3. In addition, the resonant laser can also interact with the local defects or impurities to produce empty charge traps that can effectively reduce the free charge carrier density as introduced by the non-resonant laser. This mechanism may explain the decrease of rates k_{GD} and k_{DG} as shown in Figure 3.4(g) of the Chapter 3.

Appendix B Supporting materials for Chapter 4

B1: SPECTRAL JUMPS OF EMITTER E1 AT DIFFERENT TEMPERATURE

Time-resolved spectral jumps of the emitter E1 are recorded with a constant excitation power at different temperatures from 50 K to 240 K. The ON time distributions of both state "A" and state "B" satisfy a single exponential decay (see Figure B(1a,b)). The extracted conversion rates R_{AB} and R_{BA} in Figure B1© show a 20% fluctuation over the average rates, corresponding to 11% of power fluctuation for a quadratic power dependence. We argue that the temperature dependence of the conversion rates is mainly caused by the variation of excitation power coupled to the color center. As the temperature changes, the distance between the objective and the sample can drift, causing variation of the excitation efficiency. Thus, we conclude the conversion process is insensitive to the temperature.

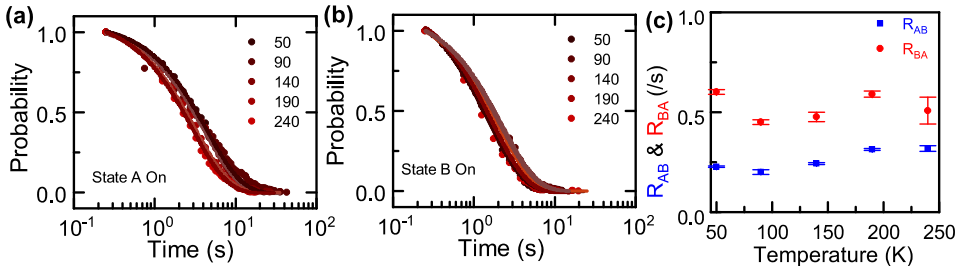

Figure B1[11]. Time constants at different temperatures for the emitter E1. Temperature dependence of the probability distribution of ON period for states A (a) and B (b) for the same emitter in the main text. The excitation power is 0.8mW. (c). Extracted conversion rates R_{AB} from (a) and R_{BA} from (b) at different temperatures. The conversion process between states A and B persist up to room temperature. Reproduced with permission [11]. Copyright 2020, Wiley-VCH.

B2: SPECTRAL JUMPS FROM OTHER QUANTUM EMITTERS

Spectral jumps of additional emitters E2 and E3 within the same Ge-implanted sample are shown in Figure B2(a) and Figure B2(d), respectively. Both emitters show a single line emission when they are in jumping states but emitting at different wavelengths after long-time exposure (as shown in Figure 4.4(b, d)). Similar to that of emitter E1, the ON-time distributions of state "1" and "2" can also be described by a single exponential function.

When using an intensive laser to continuously illuminate the color center, the spectral may disappear by showing a short period of high counts first as shown in Figure B2(c). Here, emitter E2 is exposed in a 2 mW 532 nm laser from the t=0. The count rate shows an abrupt increase

after 2100 s, which sustain for a period of time of ~90 s before dropping down to a low count rate state with the spectrum permanently changed as shown in Figure 4.4(b). We found that such a conversion process is irreversible.

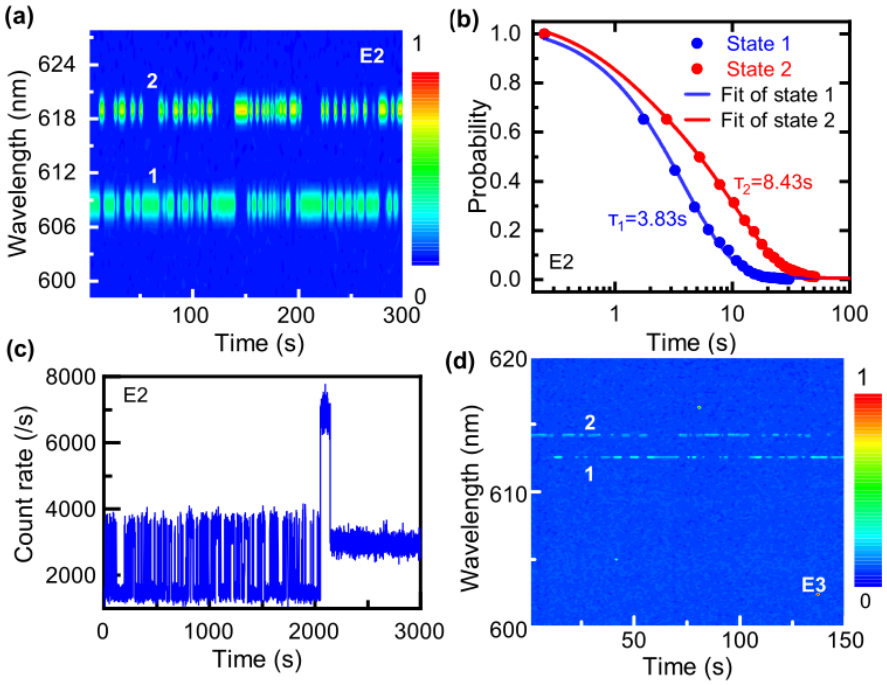

Figure B2. Spectral jumps of two additional color centers at 20 K[11]. (a) Repetitive collection of 300 PL spectra of the emitter E2, each exposed for 0.5 s. The two optical-active transitions are labeled as '1' and '2', respectively. (b) Distribution of the ON period for state '1' (blue) and state '2' (red) when the emitter E2 is under 0.5 mW excitation. The raw data is fit with a single exponential function, giving a characteristic state-conversion time of 3.83±0.04 s and 8.43±0.17 s for state '1' and '2', respectively. (c). Time trace for jumping elimination. The binsize is 0.1 s. The E2 sample is under 2 mW 532 nm laser illumination for the whole process. (d) Repetitive collection of 300 PL spectra of the emitter E3, each exposed for 0.5 s with laser power of 1mW. The two peaks are also labeled as '1' and '2'. Reproduced with permission [11]. Copyright 2020, Wiley-VCH.

Appendix C Supporting materials for Chapter 5

	EPR [MHz]		ODMR [MHz]	
	D	**E**	**D**	**E**
kk	1282	0	1284.35±0.32	0
hh	1331	0	1332.43±0.26	0
hk	1193	104	1225.85±0.36	103
kh	1328	15	1349.16±1.21	15

Table CI: D and E values comparison with resonant EPR and ODMR characterization. Overall, the results are in agreement with each other except that the D values acquired with the ODMR method for the basal center are greater compared to the EPR ones[12]. The different temperature needs to be considered for the difference.

Direct evidence of $N_CV_{Si}^-$ center creation in 4H-SiC is the hyperfine interaction with ^{14}N. We then compared the DFT calculated results with the electron magnetic resonance (EPR) resolved fine structure. In Figure C2, the experimental results are in good agreement with the theoretical predictions. The ground-state properties of the $N_CV_{Si}^-$ center in the 1- charge state can be described by the conventional spin Hamiltonian of a spin S=1 center:

$$H = \mu_B B \cdot g \cdot S + S \cdot D \cdot S + \sum_j (S \cdot A_j \cdot I_j + I_j \cdot P_j \cdot I_j - g_{Nj} \cdot \mu_N B \cdot I_j)$$

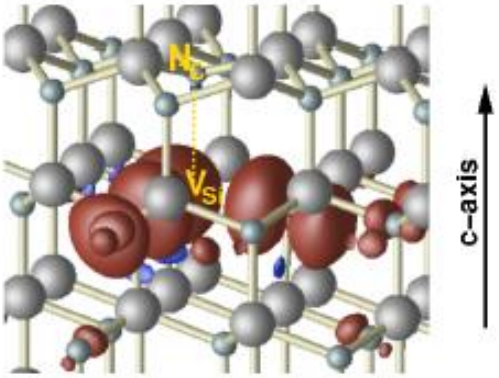

Figure C1[13]: spin density distribution of the axial $N_CV_{Si}^-$ center in 4H-SiC. The calculation shows a strong central hyperfine interaction with the central C atoms, a superhyperfine interaction with the three Si atoms near the C atoms, and a weak indirect hyperfine interaction due to core polarization on the N atom. Reproduced with permission [13]. Copyright 2020, American Chemical Society.

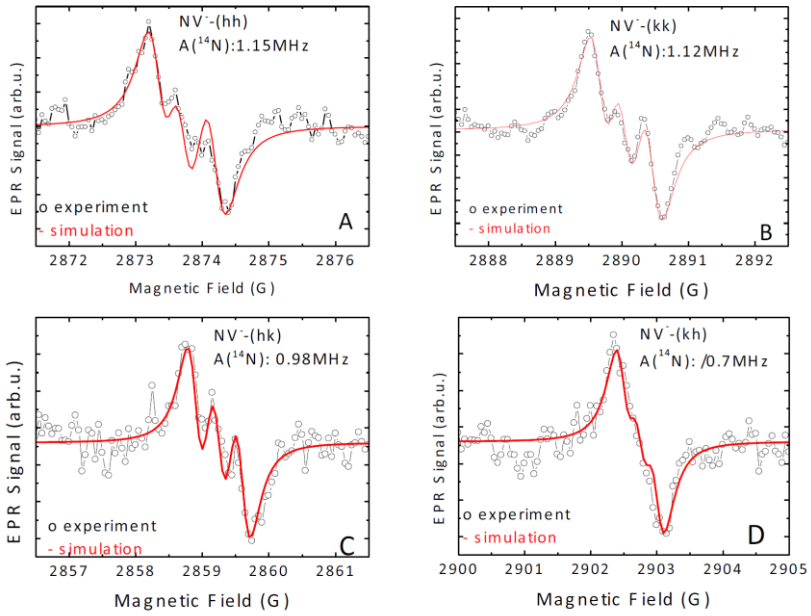

Figure C2[13]: EPR experimental results (dots) fit very well with the DFT simulation results (red curves) of electron spins and nuclear spins interaction. The theoretical A(^{14}N) value for kk center is -1.15 Mhz, hh center is -1.09 Mhz, hk center is -0.56 Mhz, and kh center is -0.84 Mhz. Experimental results for the A(^{14}N) amplitude for the four types of centers are 1.12 Mhz, 1.15 Mhz, 0.98 Mhz and 0.7 Mhz with error bars +/-0.1Mhz. Reproduced with permission [13]. Copyright 2020, American Chemical Society.

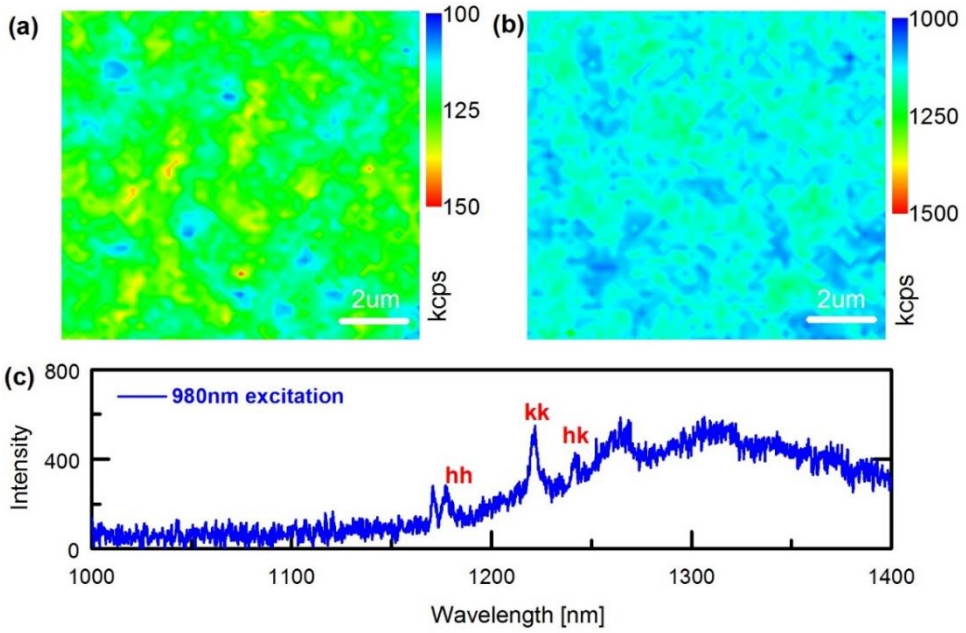

Figure C3[13]: 2D confocal PL mapping of nitrogen implanted 4H-SiC samples. (a) 2D mapping for the sample with an implantation dose of 10^{13}/cm^2. The maximum count rate is 150 K/s. (b) 2D mapping for the sample with an implantation dose of 10^{14}/cm^2. The maximum count rate is 1500 K/s. (c) Spectrum of the sample in (b) under 980 nm excitation at 10 K. The low-temperature spectrum of the Nitrogen irradiated sample clearly proves the creation of $N_CV_{Si}^-$ centers. Meanwhile, there are no evident peaks related to divacancy centers. According to the 2D mapping, the count rate is proportional to the implantation dose. This then makes single $N_CV_{Si}^-$ center generation at low dose implantation possible. Reproduced with permission [13]. Copyright 2020, American Chemical Society.

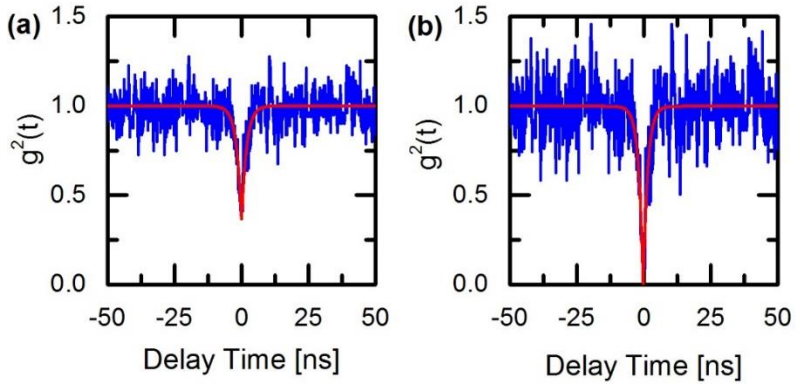

Figure C4[13]: g^2 (0) value raw data verse background corrected data. (a) $g^2(\tau)$ raw data (blue line) and its fit (red line) with $g^2(t) = A + B\exp(-|t|/\tau_0)$ giving a dip of 0.36 ± 0.06 and t_0 = 2.21 ± 0.22 ns. (b) $g^2(\tau)$ data with background corrected (blue line) and its fit (red line) giving a dip of 0.01 ± 0.02. The raw data is corrected with $g^2(t) = [N(t)/N_n - (1-\rho^2)]/\rho^2$, where $\rho = S/(S+B)$, with S refers to signal and B background respectively [7]. Here, we have a signal count rate of 16 K/s and a background level of 4 K/s. Reproduced with permission [13]. Copyright 2020, American Chemical Society.

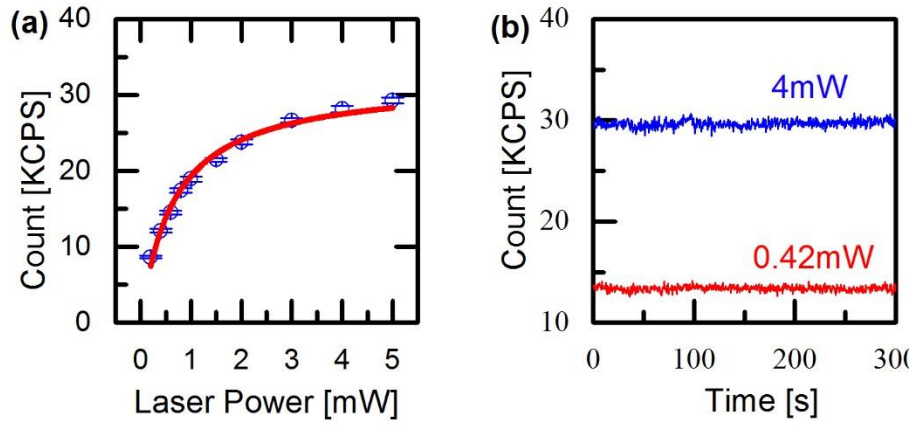

Figure C5[13]: The saturation behavior of the $N_CV_{Si}^-$ emitter. (a) Saturation curve of the learned $N_CV_{Si}^-$ single emitter in the main text. The saturation count is 27.1 ± 1.5 K, and the saturation power is 657.4 ± 1.6 μW. (b) time trace of the emission with under saturated and saturated excitation, showing the stable emission of the $N_CV_{Si}^-$ center. Reproduced with permission [13]. Copyright 2020, American Chemical Society.

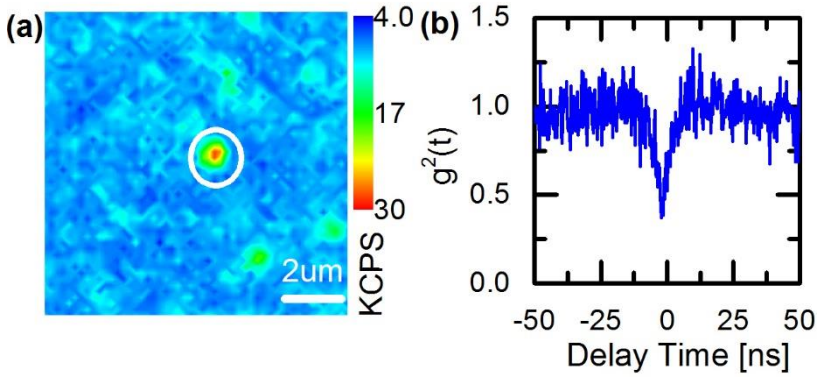

Figure C6[13]: Additional single $N_CV_{Si}^-$ emitter. (a) Confocal PL map of the same sample used in the Main text. The scale bar is 2 μm. The circled spot refers to the one with which the HBT is performed. (b) $g^2(\tau)$ measurement of the circled spot. The blue curve is the raw data without background correction, according to which the dip is lower than 0.5 (0.39) and confirms the single emission of the circled spot. As a high power of 4 mW is applied, there is a bunching behavior due to the shelving state in the excited states. Reproduced with permission [13]. Copyright 2020, American Chemical Society.

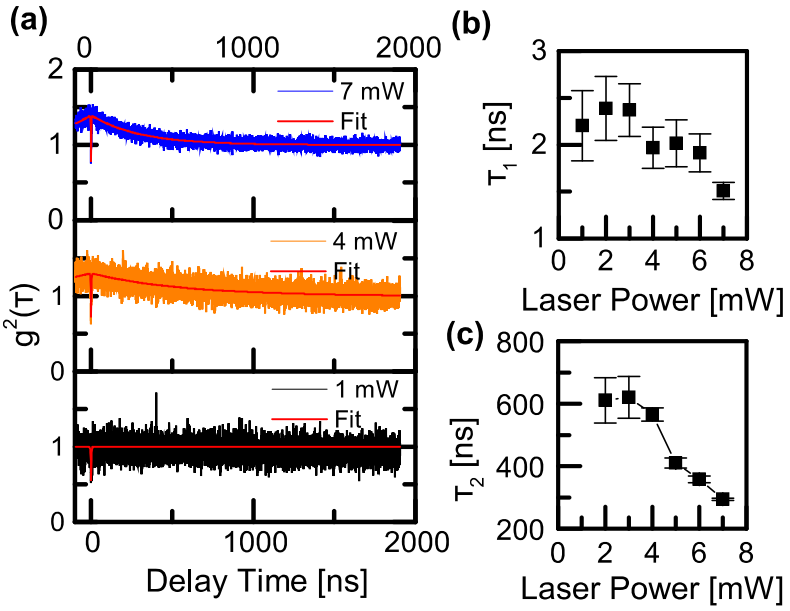

Figure C7[13]: (a) $g^2(t)$ measurements under unsaturated (1 mW) and saturated power (4 and 7 mW). The red lines refer to the fit with the two-level model (1mW only) and three-level model (the rest power); $g^2(t) = 1 - \alpha \exp\left(-\frac{|t|}{T_1}\right) + \beta \exp\left(-\frac{|t|}{T_2}\right)$. The *a, b* are the fitting parameters, and the T_1, T_2 refer to the lifetime of an exited and a metastable state. (b) The extracted lifetime of a $N_CV_{Si}^-$ excited state. (c) The lifetime of a $N_CV_{Si}^-$ metastable state. Reproduced with permission [13]. Copyright 2020, American Chemical Society.

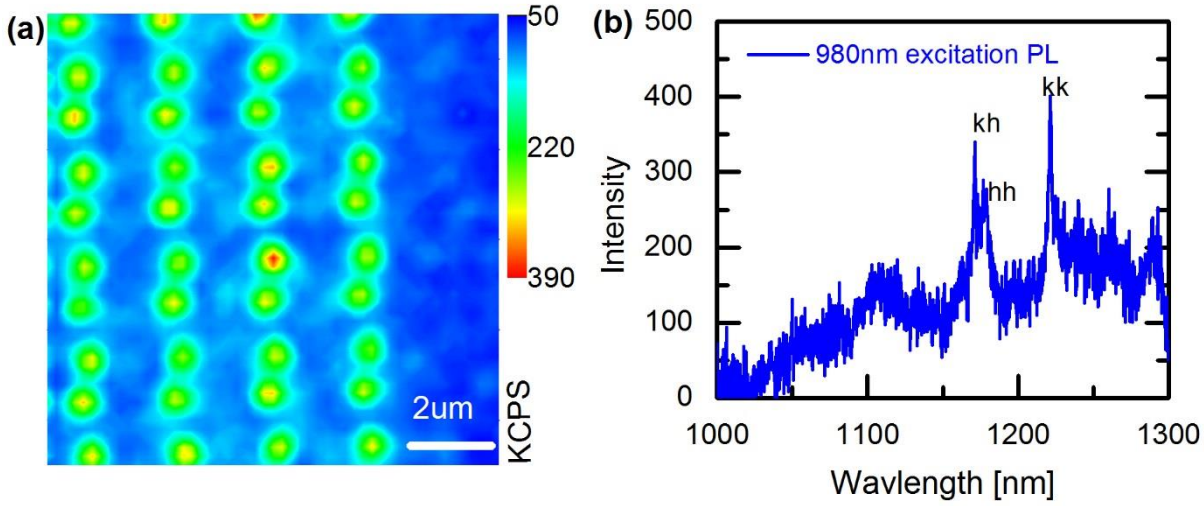

Figure C8[13]: (a) Confocal mapping of focused nitrogen ion beam implanted sample at room temperature. The scale bar is 2 μm. Due to the imperfection of the Nitrogen beam, one shot resulted in two implanted spots. (b) Spectrum related to the focused ion implantation sample at 10 K with 980 nm laser excitation and collection above 1000 nm. The peaks related to each kind of $N_CV_{Si}^-$ centers are labeled accordingly. Reproduced with permission [13]. Copyright 2020, American Chemical Society.

References

[1] CHEN D, MU Z, ZHOU Y, et al. Optical Gating of Resonance Fluorescence from a Single Germanium Vacancy Color Center in Diamond [J]. Phys Rev Lett, 2019, 123(3): 033602.

[2] LOUDON R. The quantum theory of light [M]. OUP Oxford, 2000.

[3] BOLDYREV K, MAVRIN B, SHERIN P S, et al. Bright luminescence of diamonds with Ge-V centers [J]. Journal of Luminescence, 2018, 193: 119-24.

[4] MAITY S, SHAO L, SOHN Y-I, et al. Spectral alignment of single-photon emitters in diamond using strain gradient [J]. Physical Review Applied, 2018, 10(2): 024050.

[5] MEESALA S, SOHN Y-I, PINGAULT B, et al. Strain engineering of the silicon-vacancy center in diamond [J]. Physical Review B, 2018, 97(20): 205444.

[6] SOHN Y-I, MEESALA S, PINGAULT B, et al. Controlling the coherence of a diamond spin qubit through its strain environment [J]. Nature communications, 2018, 9(1): 1-6.

[7] SIYUSHEV P, METSCH M H, IJAZ A, et al. Optical and microwave control of germanium-vacancy center spins in diamond [J]. Physical Review B, 2017, 96(8): 081201.

[8] TURUKHIN A, LIU C-H, GOROKHOVSKY A, et al. Picosecond photoluminescence decay of Si-doped chemical-vapor-deposited diamond films [J]. Physical Review B, 1996, 54(23): 16448.

[9] NEU E, AGIO M, BECHER C. Photophysics of single silicon vacancy centers in diamond: implications for single photon emission [J]. Optics express, 2012, 20(18): 19956-71.

[10] THIERING G, GALI A. Ab initio magneto-optical spectrum of group-IV vacancy color centers in diamond [J]. Physical Review X, 2018, 8(2): 021063.

[11] MU Z, ZHOU Y, CHEN D, et al. Observation of Binary Spectral Jumps in Color Centers in Diamond [J]. Advanced Optical Materials, 2020, 8(19): 2000495.

[12] ZARGALEH S A, VON BARDELEBEN H J, CANTIN J L, et al. Electron paramagnetic resonance tagged high-resolution excitation spectroscopy of NV-centers in 4H-SiC [J]. Physical Review B, 2018, 98(21).

[13] MU Z, ZARGALEH S A, VON BARDELEBEN H J, et al. Coherent Manipulation with Resonant Excitation and Single Emitter Creation of Nitrogen Vacancy Centers in 4H Silicon Carbide [J]. Nano Lett, 2020.